UNIVERSITÉ DE SHERBROOKE
Faculté de génie
Département de génie électrique et de génie informatique

Paramètres de conception optimaux pour maximiser le rapport contraste à bruit pour scanners TEP avec temps de vol

Optimal Design Considerations to Maximize the Contrast to Noise Ratio for Time of Flight PET Scanners

Thèse de doctorat
Specialité: génie électrique

Nikta ZARIF YUSSEFIAN

Sherbrooke (Québec) Canada

Septembre 2021

JURY MEMBERS

Prof. Réjean FONTAINE
Supervisor

Prof. Roger LECOMTE
Co-supervisor

Prof. Vesna SOSSI
Examiner

Prof. Martin LEPAGE
Examiner

Prof. Yves BÉRUBÉ-LAUZIÈRE
Examiner

RÉSUMÉ

Les scanners de tomographie d'émission par positrons (TEP) par temps de vol (TdV) augmentent le rapport contraste à bruit (RCB) en réduisant le bruit de fond. Ceci se traduit par un temps d'acquisition plus court ou une dose réduite. Au cours des années, la TEP-TdV a évolué vers des résolutions temporelles de l'ordre de 200 ps, ce qui correspond à une incertitude spatiale de 30 mm. Bien que cela soit suffisant pour améliorer la sensibilité effective des scanners cliniques, résoudre des petites structures comme les ganglions lymphatiques, ou des organes de petits animaux nécessite des résolutions temporelles inférieures à 50 ps pour résoudre un objet inférieur à $\sim$ 10 mm. Une résolution temporelle de 10 mm permettrait même d'éviter la reconstruction tomographique des images TEP. L'obtention d'une bonne performance d'image en TEP nécessite d'aborder simultanément tous les paramètres de qualité d'image, y compris la résolution spatiale, la sensibilité et le RCB. Cependant, il est peu probable que cela se produise, car des études ont démontré que les choix de conception du détecteur peuvent favoriser certains paramètres de qualité d'image, mais en dégrader d'autres. On doit donc cibler les facteurs contribuant au RCB, l'un des paramètres importants de la qualité d'image. Un de ces facteurs est le choix de l'épaisseur du cristal qui affecte la résolution temporelle et donc, le RCB. Bien qu'une résolution temporelle améliorée augmente la détectabilité des petites lésions, on doit étudier les compromis afin de trouver un point d'équilibre offrant à la meilleure performance d'image possible.

La motivation de cette recherche est de déterminer la limite à partir de laquelle le TdV améliore la qualité de l'imagerie des petits animaux et également, d'étudier les compromis nécessaires entre la longueur des cristaux, la résolution temporelle et la sensibilité pour atteindre la qualité d'image optimale. Ces compromis ciblent l'amélioration de la résolution temporelle pour améliorer les performances du RCB sans compromettre les autres paramètres de qualité d'image. Ces travaux démontrent qu'une résolution temporelle de 100 ps est le seuil à partir duquel le TdV améliore le performance RBC de l'imagerie des petits animaux. De plus, ils montrent que le volume du cristal peut être réduit de 19 % sans détériorer l'image. Un modèle est également proposé pour prédire le RCB avec un niveau de confiance relativement élevé et il peut être utilisé comme guide pour concevoir la prochaine génération de scanners. L'introduction d'une nouvelle mire élaborée pour étudier les avantages et les impacts du TdV sur la détectabilité des lésions pour les scanners TdV est par la suite présentée.

Mots-clés : Tomographie d'émission par positrons, Temps de vol, Résolution temporelle, Rapport contraste sur bruit, Imagerie des petits animaux, Qualité d'image, Modèle quantitatif.

ABSTRACT

Time-of-flight (TOF) positron emission tomography (PET) scanners improve contrast-to-noise ratio (CNR) that translates into reducing the scan time or the required injected dose. During the past years, TOF PET has evolved towards temporal resolutions of the order of 200 ps, corresponding to a spatial uncertainty of 30 mm along the line of response (LOR) defined by the two annihilation photons. Although this location uncertainty is sufficient to improve the effective sensitivity of clinical scanners, resolving small size tissues such as a lymph node, or small animal organs would require the timing performance to be less than 50 ps to resolve objects smaller than $\sim$ 10 mm. A coincidence time resolution around 10 ps would even allow to avoid tomographic reconstruction of PET images.

Obtaining good image performance in PET demands tackling simultaneously all image quality parameters, including spatial resolution, sensitivity, and CNR. However, this involves difficult trade-offs as studies have demonstrated that choices made at the design level for the detector configuration may enhance some image quality parameters but are then detrimental to others. It is therefore mandatory to identify and carefully investigate the factors contributing to the CNR, one of the most important parameter for image quality. One such factor is the choice of crystal thickness that affects coincidence time resolution and thus CNR. Although improved coincidence time resolution increases the chance of small lesion detectability, trade-offs should be studied to find an optimum compromise maximizing the image performance.

The motivation underlying this research is to determine the limit where TOF adds gain in small animal PET imaging and also investigate trade-offs between crystal length, timing resolution, and sensitivity to find the optimum image quality. These trade-offs target the coincidence time resolution improvement to enhance CNR performance without compromising the other parameters of image quality. It is demonstrated that a coincidence time resolution of 100 ps is the threshold where TOF starts to improve the image performance of a small animal scanner. In addition, it is shown that the crystal thickness can be reduced by 19 % without loss on the imaging performance. A model is also proposed that describes the CNR performance with a relatively high level of confidence at early stages of the design, and can be used as a guide to design the future generation of scanners. This is followed by introducing a new phantom purposely designed to study TOF benefits and impacts on lesion detectability for PET scanners.

Keywords: Positron Emission Tomography, Time of Flight, Coincidence Time Resolution, Contrast to Noise Ratio, Small Animal and Clinical Imaging, Image Quality, Quantitative Model.

To my beloved parents, Hoori and Hossein, for their unconditional love and everlasting support

ACKNOWLEDGEMENTS

First and foremost, I would like to express my sincere gratitude to my supervisor, Prof. Réjean Fontaine, for all the useful discussions, thoughtful comments, and also his remarkable guidance, continuous support and assistance that played a key role in the accomplishment of this research. His good sense of humour and consistent positiveness made the learning process and progress easier and more joyful. I am also very grateful to my co-supervisor, Prof. Roger Lecomte, for how dynamic and supportive he was in taking me to his group, for all the useful discussions and inputs. His insightfulness and willingness to help gave me the inspiration to succeed.

I would like to thank my jury members, Prof. Vesna Sossi, Prof. Martin Lepage, and Prof. Yves Bérubé-Lauzière for taking the time to review this work. Your comments without a doubt helped a lot in improving the quality of this work.

Special thanks to my colleague, Ph.D. Émilie Gaudin who supported me in the experimental and simulation procedure of this work. I wish to express my sincere thanks to the CIMS group, in particular, Ph.D. Catherine Pepin for her kindness, influential support and caring and also for being a good friend. I would like to thank my colleague, Ph.D. Maxime Toussaint, who always offered his best suggestions and advice. Special thanks to the 3IT group, in particular, Caroline, for her willingness in providing technical help and all who supported me at every step of this work. I am grateful to Ph.D. Jean-Baptiste Michaud for making his technical resources available to conduct this research. I'd like to express my gratitude to Calcul Québec and Compute Canada support team, in particular, Mr. Huizhung Lu who provides support readily in employing the resources.

I also take this opportunity to express my thankfulness to all my friends, Mohammad, Mohsen, Nooshin, Hazhir, and Narges who in one way or another shared their support either morally, physically or technically. Special thanks to my cousins, Ghazal and Omid for spending cherished time and offering their best help and advice.

Last but not least, I would like to express my deepest appreciation and gratefulness to every member of my family. To my mom, Hoori Razavi, you are my first teacher and I have still a lot to learn from you, thanks for encouraging me to do a Ph.D. and thanks to stay by my side at each step of this work. To my dad, Hossein Zarif Yussefian, thanks for the unwavering support and belief in me that paved the way to accomplish this journey. Many thanks to my older brother, Nima, who is an inspiration to me since the day I was born and to my younger brother, Mani, who is the kindest friend ever, for your unconditional support and consistent encouragement that kept me going to accomplish this research.

TABLE OF CONTENTS

LIST OF FIGURES

LIST OF TABLES

LIST OF ACRONYMS

Acronym	Definition
APD	Avalanche Photodiode
ASIC	Application-specific Integrated Circuit
BGO	Bismuth Germanate
CASToR	Customizable Advanced Software for Tomographic Reconstruction
CNR	Contrast to Noise Ratio
CRC	Contrast Recovery Ratio
CT	Computed Tomography
CTR	Coincidence Time Resolution
FDG	Fluorodeoxyglucose
FOV	Field of View
FWHM	Full Width at Half Maximum
GATE	Geant4 Application for Tomographic Emission
LOR	Line of Response
LSO	Lutetium Orthosilicate
LYSO	Lutetium Yttrium Orthosilicate
MCP	Micro-channel Plate
MLEM	Maximum Likelihood Expectation Maximization
MRI	Magnetic Resonance Imaging
MSE	Mean Squared Error
NaI	Sodium Iodide
NEC	Noise Equivalent Count
NEMA	National Electrical Manufacturer Association
OSEM	Ordered Subset Expectation Maximization
PET	Positron Emission Tomography
PMT	Photomultiplier Tube
ROI	Region of Interest
SD	Standard Deviation
SiPM	Silicon Photomultiplier
SNR	Signal to Noise Ratio
SOR	Spill Over Ratio
SPAD	Single Photon Avalanche Photodiode
TDC	Time to Digital Convertor
TOF	Time of Flight
UHR	Ultra High Resolution
VOI	Volume of Interest

CHAPTER 1

INTRODUCTION

1.1 Problem Statement

Cancer is a main public health concern and the first leading cause of death in Canada during the past five years [3]. Early detection is crucial to beating cancer as early diagnosis directly affects the effectiveness of the treatment, reducing the mortality rates and lessening the economic burden on the health system. The importance of early cancer detection is highlighted by knowing that approximately one out of two Canadians will be diagnosed with a type of cancer in their lifetime and for some types, such as prostate cancer, roughly 24% to 49% can be treated if early detection is available [4]. While studies have shown that positron emission tomography (PET) scans can be useful in the early diagnosis of cancer, it is definitely considered to be one of the most powerful tools at staging cancer [5, 6].

PET is a molecular imaging modality used in clinical and *in vivo* small animal research [7]. It allows obtaining the information on molecular processes through metabolism where glucose is the most widely used radiolabeled compound for its ability to detect diseases such as cancer [8] and neurological disorders [9]. In conventional PET, the radiotracer labeled with a positron emitting atom is administered to the subject. Following the disintegration of a proton in the nucleus, a positron is emitted and annihilated with a surrounding electron resulting in the emission of two back-to-back 511 keV photons; these are subsequently detected by a ring of detectors placed around the subject. Information regarding the position of the interaction, energy deposited at the time of interaction and the detector id are registered and used to form the image.

In the mid 1970s, time-of-flight (TOF) technology was initially introduced in PET through a Ph.D. thesis entitled, "Time-of-flight localization of positron emitting isotopes" [10]. This work proposed using the arrival time difference of 511 keV photons to more accurately locate the source in the field of view (FOV). However, the achieved TOF resolutions at the time were about 400 - 700 ps, and were not sufficient exploit its benefits in imaging applications; hence making the TOF scanner unqualified [11–13]. The emergence of dense Lutetium-based scintillators along with the development of photosensor technology led to better time performance that triggered once again the development of TOF-PET scanners [14, 15]. The best currently achieved TOF resolution in clinical scanners is 215 ps,

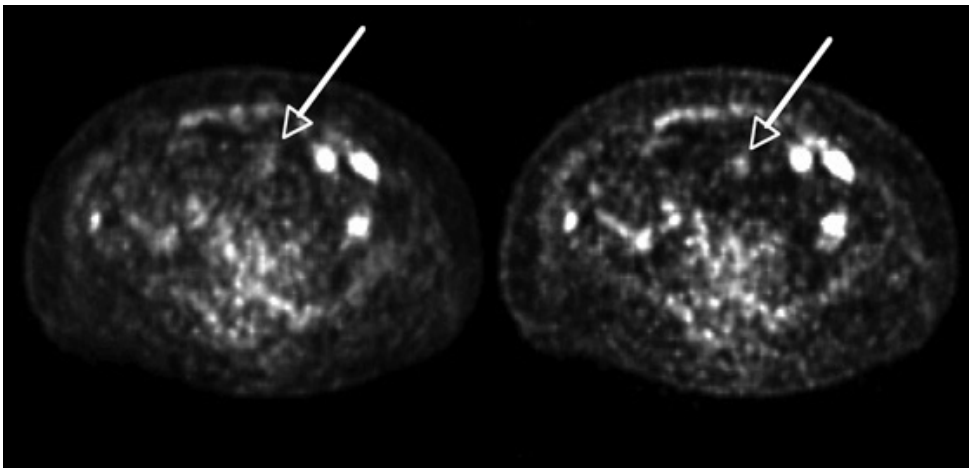

Figure 1.1 A patient with colon cancer, after injection of 555-MBq of FDG and scan for 3 min/bed position following a 60-min uptake period, Left: non-TOF image, Right: TOF image. In TOF image cancerous lesion can be clearly discerned. Image reprinted from Joel Karp, 2008 [1].

which is not yet a sufficient improvement to benefit from TOF in small animal imaging [16]. However, in laboratories TOF resolution is improved down to 30 ps [17]. The main advantage of employing TOF is shown to enhance small lesion detectability, which is desirable for increasing the chance of early detection of metastasis and cancerous cells (Figure 1.1) [14, 18–22]. The better the time performance of a TOF-PET scanner is, the better is its ability to discern small lesions; thus, it is more effective in diagnosing the diseases. Therefore, in the design of TOF-PET scanners, parameters contributing to TOF resolution should to be chosen carefully to optimize the time performance.

1.1.1 Physical Parameters of Image Quality in PET

To obtain a detailed image, three physical parameters should be optimized: spatial resolution, sensitivity, and contrast-to-noise ratio (CNR).

Spatial resolution: The spatial resolution is a key factor in evaluating the performance of PET scanners. It is defined as the minimum distance required to discriminate between two adjacent objects in an image. Spatial resolution is specified, and can be estimated, as the full-width half-maximum (FWHM) of uncertainties that contribute to the resolution degradation at the design level [23]. Spatial resolution in the submillimeter range allows for the detection of receptors and proteins associated with the early development of diseases. Hence, a system with high spatial resolution performance increases the chance of small tumors being detected and also allows for monitoring their response to a treatment. While TOF information does not generally seem to affect the spatial resolution performance, in

a recent study it was shown that if ultra-fast TOF (below 30 ps) could be achieved, spatial resolution performance could be improved [24].

Sensitivity: Scanner sensitivity can be reasonably estimated at the initial stages of a design based on the detector geometry and its arrangement [25]. A highly sensitive scanner requires lower administered dose to the patient and provides high counting statistics for the image. TOF technology does not directly contribute to the sensitivity performance. However, studies have shown that TOF can compensate for sensitivity loss and lead to better image performance when low counting statistics are present [26, 27].

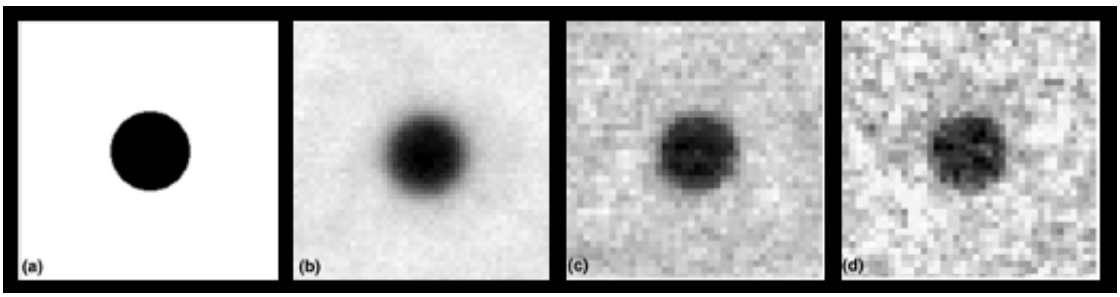

Figure 1.2 a) Ideal image with enough statistics, perfect CNR, spatial resolution and sensitivity, b) Low spatial resolution, high CNR, high sensitivity c) High spatial resolution, low sensitivity (high noise), low CNR d) low spatial resolution, CNR and sensitivity. Image reprinted from Anders Brahme, 2014 [2].

CNR: CNR is the ability of the scanner to differentiate objects from the background noise and as the chance of neglecting a lesion in a noisy background increases if the lesion is small, this is sometimes referred to as small lesion detectability. The CNR is evaluated by drawing a region of interest (ROI) that encapsulates the desired lesion in the image and is calculated as follows:

$$CNR = \frac{C_{lesion} - C_{background}}{\sigma_{background}}, \tag{1.1}$$

where C_{lesion} and $C_{background}$ are the mean activities in the ROI of the lesion and its surrounding area, respectively, and $\sigma_{background}$ is the standard deviation of the background [28]. Both spatial resolution and sensitivity contribute to the CNR performance by revealing fine details and improving statistics, respectively. Therefore, the CNR performance is mainly dependent on the counting statistics, the spatial resolution, the size of the lesion, the reconstruction algorithm, and the reconstruction parameters. Although rarely addressed in the literature, CNR performance plays an essential role in the imaging performance of any scanner. TOF's principal impact is on improving the CNR performance by reducing the background noise in the image [29]. This happens because the location of the annihilation

is estimated based on TOF information, thus the noise propagation is reduced during the image formation process which leads to the reduction of background noise.

Designing a scanner that only provides an image with high spatial resolution does not guarantee obtaining a high quality image that is adequate for diagnostic purposes, particularly in the case of small lesion detection and small animal imaging. To have an efficient scanner that allows for obtaining detailed images, both high contrast and high spatial resolution, along with enough counting statistics have to be maintained (Figure 1.2). Nonetheless, improving all these parameters together is impossible, and trade-offs have to be made at each step of the design process. TOF adds another degree of freedom that will allow more flexibility in the choice of the other parameters, and so, fewer compromises in the trade-offs between all parameters.

1.1.2 Design of PET Scanner Detectors

A PET scanner detector is composed of three elements: scintillator or crystal, photodetector, and electronics (Figure 1.3). Such a detector works on the basis of the conversion of the 511 keV photon energy into a voltage pulse, that is subsequently processed by the scanner electronics. There are many alternatives in designing detectors for PET in terms of crystal material and dimensions, type of photodetector, and how quickly and efficiently the electronic block processes the signal. This makes the design process a challenge as the imaging performance of the scanner is highly affected by the choice of design parameters and those parameters have interdependent relationships with one another meaning that the improvement of one parameter may result in the degradation of another. For example choosing a large crystal surface favours sensitivity performance as it allows for more photons to impinge on the crystal surface; however, it degrades the spatial resolution performance [30, 31]. One important key factor that affects the performance of all three parameters of image quality is the crystal length, as choosing long crystals improves the sensitivity performance by increasing the chance of interactions, however; it degrades the spatial resolution performance in the periphery of the FOV. Moreover, a long crystal increases the travel pathlengths between the interaction position inside the scintillator and the photodetector, which results in degrading the timing performance; this reduces the image CNR for TOF-PET scanners [32, 33]. The improvement of the timing performance at photodetector level has advanced in the recent years [34, 35]; this also makes optimizing the crystal length a prime factor for further improvement of TOF performance in future.

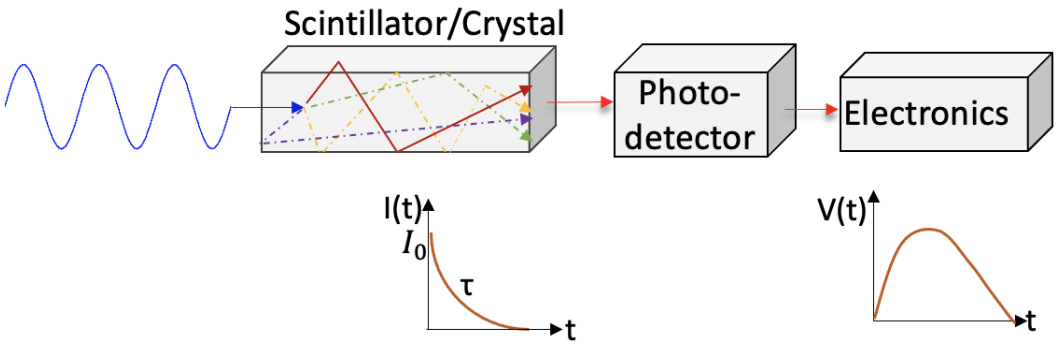

Figure 1.3 A typical PET detector block.

1.1.3 Dedicated PET Systems

The first commercial PET system was developed in 1976, making the PET scanners a focus of the diagnostic imaging industry ever since [36]. PET scanners have evolved throughout the years with advances in their detector material, photodetector technology, spatial and coincidence time resolutions (CTRs), and geometrical capacity in body coverage and sensitivity [16,37–42]. However, academia never ceased to explore even more innovative avenues by introducing TOF information leading to the development of first TOF capable system in 1982 [12], and hybrid systems such as PET combined with computed tomography (CT) and PET combined with magnetic resonance imaging (MRI) [43, 44].

1.1.4 Dedicated Small Animal Systems

The extensive use of clinical PET scanners has provided an incentive to develop small diameter PET systems that allow to conduct experimental studies in animal models. Thus, small animal PET scanners have emerged in the 1990s [45–47] to assess new radiotracers in non-human subjects. Another important aspects of small animal imaging is to reduce the risk on human subjects, develop novel radiotracers, and study how body organs would respond to a treatment. There are also some limitations in small animal imaging imposed by the type of the animal model that is used in the research. Some small animals such as rodents are warm-blooded species with small size, thus they require more metabolic energy to keep their body temperature steady in particular when they are under anesthesia on the scanner bed. This may unfavourably affect the results of some studies specially when the targeted organ is the heart. Due to this, large species such as dogs or pigs have been preferred over rodents as their organ size and their physiological characteristics are better matched with humans. This also makes the transfer of the findings from animals to humans easier. However, their breeding and housing conditions are challenging that make

them less desirable as the animal model in the preclinical imaging.

Among preclinical PET scanners, LabPET scanners were developed in different sizes and dimensions allowing for the study of small to mid-sized animals as well as human brains, with the first prototype introduced in 2005 [48, 49]. One unique feature of these scanners is the one-to-one coupling of scintillator to photodetector. This pixelated configuration, as implemented in the LabPET II platform, leads to superior spatial resolution performance, roughly equal to physical limits. Hence, TOF technology can be added to these scanners to enhance their CNR image performance.

1.2 Objectives of the Research

Considering the impact of TOF technology in enhancing image quality, along with the fact that the LabPET II platform of scanners has already been optimized for spatial resolution performance, the main goal of this research is to investigate the possible benefits of TOF technology for future generations of LabPET II scanners. Specifically, this project aims to study the effect of crystal length reduction as one potential improvement made possible by TOF information in enhancing the imaging performance of LabPET II scanners. This will be achieved by finding a figure of merit that can express the performance of the scanner in terms of image CNR. Furthermore, to obtain a CNR model for LabPET II brain scanner, a phantom will be designed for the purpose of assessing CNR performance for TOF-PET clinical scanners. Thus, the following objectives are pursued:

1. Investigating the benefits of exploiting TOF information for small animal imaging.
2. Identifying the key parameters affecting CNR performance and their trade-offs for a highly pixelated scanner.
3. Developing a figure of merit for evaluating CNR performance to help in the design of the future generations of scanners.
4. Designing a phantom to add flexibility in CNR performance evaluation for clinical TOF PET scanners.

The figure of merit will also set the roadmap for future designs of LabPET II scanners. The method proposed in this work for deriving the model can be employed by other scanner developers to implement optimal CNR performance. The phantom was designed to become standard to assess the impact of TOF resolution on CNR performance for clinical scanners. Ultimately, the outcome of the proposed research is to improve CNR performance that will lead to better diagnostic imaging and reduce the health care burden.

1.3 Structure of the Thesis

The present document consists of seven chapters. Chapter 2 presents a literature review and discusses background pertaining to the nature of the current research including: principles of PET, time-of-flight PET, the unavoidable trade-offs that must be made while designing any scanner, performance parameters to consider while designing a scanner along with their dependencies, and finally, how the data are analyzed and processed. Chapter 3 presents the results of a study on TOF benefits and trade-offs between scan time, crystal length, and TOF resolution using the LabPET II scanner for mouse imaging as a model. The outcome is published in *IEEE Transaction on Radiation and Plasma Medical Sciences (IEEE TRPMS)* [50]. A detailed methodology to derive a CNR model using regression analysis is presented in Chapter 4, which has also been published in *IEEE TRPMS* [51]. In addition, to be able to study TOF resolution effect on the LabPET II brain scanner, a phantom is designed which is presented in Chapter 5. Here the phantom is validated using the Siemens Biograph Vision TOF PET/CT scanner in a simulation and experimental study. The result of this research has been submitted to the journal *Physics in Medicine and Biology* . The main contributions as well as the limitations of the current work are discussed in Chapter 6. Finally, this dissertation ends with Chapter 7 where the main achievements and future perspectives are presented.

Published articles: There are two published articles for this work [50, 51].

Submitted articles: There is one submitted article [52].

CHAPTER 2

STATE of the ART and LITERATURE REVIEW

This chapter starts with discussing the principles of PET. Then the main challenges of designing a scanner are presented. This part will be followed by defining the most important parameters affecting the imaging performance of scanners and their associated parameters. The chapter ends with a description of the image quality assessment protocol and the method used for data post-processing.

2.1 Principles of PET

The principal objective of medical imaging is to observe and diagnose pathologies in tissues and organs. In the case of PET, the objective is to delineate the radiotracer uptake in a tissue or an organ following the injection of a radiolabeled pharmaceutical agent.

2.1.1 Radioactive Tracer

The radioactive tracer or radiotracer, or radiolabeled agent is a chemical combination of a radionuclide attached to a molecule such as anti-body, protein, peptide, or glucose. The most common radiotracer used in PET from the mid-1970s to the present is fluorodeoxyglucose (^{18}F-FDG) that is used intensively in oncology to identify and localize cancerous tissues [53]. PET radionuclides must be β^+ emitters and are characterized by their half life and their integration type with the targeted molecules. The half life, defined as the time required for the substance to lose half of its initial activity, should be high enough to accommodate the transportation and preparation time and short enough so to avoid unnecessarily exposure to radiation for the patients.

Radiotracers are used in the detection of a variety of tumors and their metastasis, and for studying the functionality of different organs, including among others, liver and pancreas function, brain metabolism, lung ventilation, perfusion and cancer detection, kidney and adrenal glands, heart blood flow and metabolism [54–59]. Table 2.1 shows a list of radionuclides widely used in PET for generating diagnostic and therapeutic radiotracers.

The radionuclides presented in Table 2.1 are mostly used to generate diagnostic radiotracers that are useful to detect or monitor of a disease or the response to therapies, however,

Table 2.1 Commonly used radionuclides in PET.

Radionuclide	Half life	Decay type	Diagnostic or therapeutic
Carbon 11	20.4 min	β^+ (100%)	Diagnostic
Fluorine 18	109.8 min	β^+ (97%) EC (3%)	Diagnostic
Gallium 68	68 min	β^+ (89%) EC (11%)	Diagnostic
Copper-64	12.7 h	β^+ (18%)	Diagnostic
Iodine-124	100.2 h	β^+ (26%) EC (74%)	Therapeutic & Diagnostic
Zirconium-89	78.4 h	β^+ (23%) EC (77%)	Diagnostic

in recent years, extensive studies on generating the therapeutic radiotracers have been conducted in particular, to treat prostate cancer [60].

Whenever a radiotracer is administered, it is distributed within the body and will eventually interact with the targeted tissues. Upon disintegration, the emitted positron interacts with nearby electrons producing two simultaneous annihilation 511 keV rays as

$$p \longrightarrow n + \beta^+ + \nu \xrightarrow{\beta^+ \ slowing \ down} \beta^+ + e^- \rightarrow 2\gamma, \tag{2.1}$$

where p is a proton, n is a neutron, β^+ is a positron produced by disintegration of the radiotracer, ν is a neutrino, e^- stands for an electron and γ is an annihilation photon that has a 511 keV energy. The goal of PET is to track the fate of the radiotracer *in vivo* in order to investigate biochemical processes using very low concentrations of the radiotracer, typically in the range of 10^{-9} to 10^{-12} mol/L [55], revealing metabolic activities at this level is a characteristic that makes PET unique in comparison to other imaging modalities.

2.1.2 Types of Interactions

The photons emitted following the annihilation can undergo three major types of interactions which are photoelectric absorption, Compton scattering, and Rayleigh or coherent scattering. However, only Compton scattering and photoelectric interactions are of importance in the case of diagnostic imaging. Rayleigh scattering has a negligible effect due to the low energy nature of these interactions for 511 keV incident photons. The two common interactions in diagnostic imaging are further described below.

Photoelectric Absorption

Photoelectric absorption is a physical process in which a photon transfers all of its energy (E_g) to an orbital electron, called the photoelectron, which emerges with an energy (E_e) where $E_e = E_g - E_b$, whereby E_b is electron binding energy, in the form of kinetic energy. A vacancy that is created by the ejected photoelectron can be filled by the process that

leads to the emission of either an Auger electron or characteristic X-rays. Characteristic X-rays are generated when an electron from the outer shell fills the vacancy in the inner shell. This electron transition can be followed by the ejection of another electron from one of the outer shells which is called the Auger electron.

Compton Scattering

Compton scattering is an inelastic scattering of photons in which a photon with E_0 energy hits an electron, the photon is deviated by an angle θ from its original direction, and transfers part of its energy to the recoil electron. The energy of the scattered photon

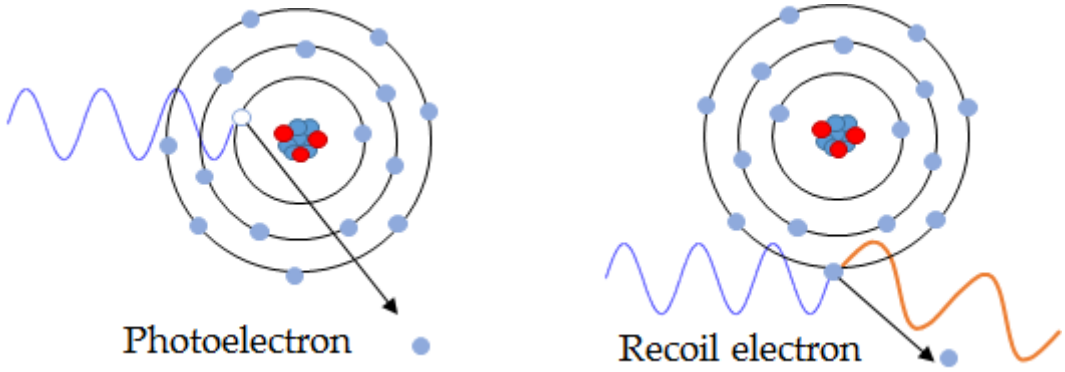

(a) Photoelectric interaction.

(b) Compton scattering interaction.

Figure 2.1 Two most important interactions in PET.

(E_{sc}) and the energy of the recoil electron can be calculated using the Compton scattering formula given by

$$E_{sc} = \frac{E_0}{1 + \frac{E_0}{m_0 c^2}(1 - \cos(\theta))}, \tag{2.2}$$

This equation shows that the maximum transferred energy to the recoil electron, $E_0 - E_{sc}$, occurs at the backscatter angle ($\theta = 180°$) and equals $E_0/3$ or 170 keV for a 511 keV incident photon.

2.1.3 Coincidence Detection

Whenever two photons reach the opposing detectors within a preselected time window, they are considered to originate from the same annihilation event and thus said to be in coincidence. The line along which the coincidence event occurs and relates detectors provides positional information and is called line of response (LOR) [61]. The coincidence events are categorized into three groups: random, scatter, and true coincidences. Random coincidences refer to the detection of two 511 keV photons falling into the time window although they do not originate from the same annihilation event. This happens when two

radioisotopes decay quasi-simultaneously creating two pairs of annihilation photons but only one of the photons of each pair reaches surrounding detectors defining a wrong LOR. Scatter coincidences are generated when two photons originating from the same events fall within the coincidence window but, due to the scattering of one of the photons, the LOR is incorrectly associated to them. Thus, they are registered as a valid coincidence as demonstrated in Figure 2.2. Only true coincidences form LORs that represent the actual point of emission; the other false coincidence events add background noise and blurring to the image.

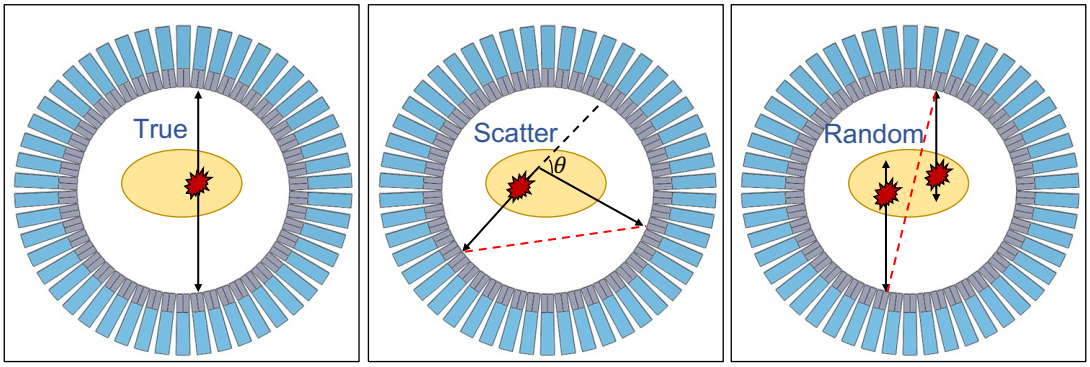

Figure 2.2 Types of coincidences.

2.1.4 Data Acquisition Chain

A typical PET acquisition chain is based on scintillation detectors consisting of a scintillator, photodetector, and block of electronics where the analog signal from the photodetector is converted into a timestamp and energy. Figure 2.3 depicts a typical acquisition chain.

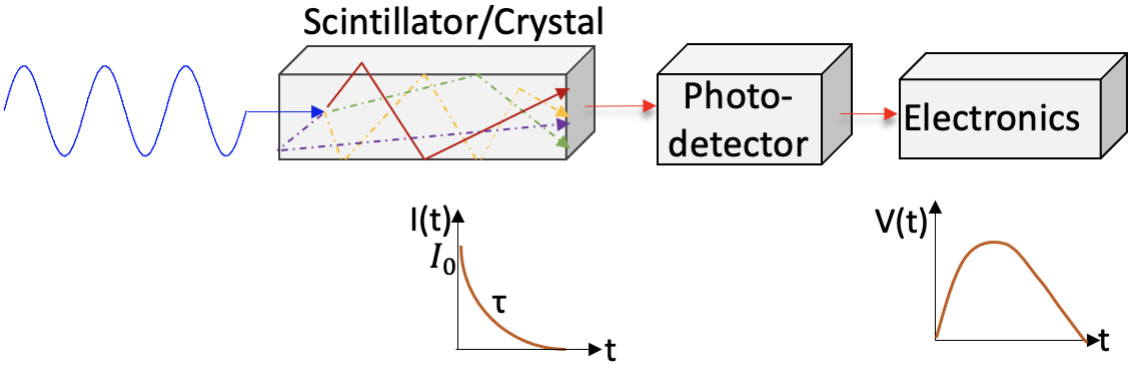

Figure 2.3 Typical data acquisition chain in PET.

Scintillator

Radiation detectors differ in their detection method. In the case of PET, the ionizing radiations produce visible light while interacting with crystals, so-called scintillators. Upon

interaction, the photon is absorbed and its energy converted to visible light. The shape of emitted light by the crystal follows an exponential decay given by

$$I = I_0 e^{\frac{-t}{\tau}}, \tag{2.3}$$

where I_0 and τ are two physical properties of the scintillator, the initial intensity of the light pulse and decay time, respectively. As scintillators are the first block of the acquisition chain, they play a crucial role in the design of PET scanners and should have the following properties [62]:

- The material should be dense with high atomic number leading to a high stopping power to improve the system detection efficiency, and thus the sensitivity.
- The dimension should be optimized for high detection efficiency to provide enough statistics as well as allowing for high spatial resolution.
- Short decay time to limit detector deadtime and allow high counting rate and, in the case of time of flight, to enable high CTR.
- High light yield to provide for high scintillation photon statistics and high energy resolution for better event discrimination.
- The refraction index should match the optical coupling of the photodetector to enhance light transmission efficiency.
- The wavelength of the converted light should be in visible range ($\sim$ 420 nm) to match the photodetector spectral response.
- Be non-hygroscopic and chemically stable.

These desirable characteristics for scintillators make it difficult to find the material satisfying all these properties. Initially, sodium iodide (NaI) was used in the design of PET scanners [63]. However, NaI is highly hygroscopic and it has a slow decay time, that have stimulated the search for a new scintillator material. This led to the introduction of Bismuth germinate (BGO) crystals [64, 65]. The main advantage of BGO was its high density warranting high sensitivity. However, it also suffers from a low light yield and slow decay time component that contribute to poor timing performance. A new generation of cerium doped lutetium orthosilicate (LSO) crystals and its derivates emerged in the 1990's. These scintillators provide faster decay times in comparison to BGO and relatively high light yield [66]. These scintillators gradually replaced BGO crystals in the majority of modern PET scanners [16, 42].

Photodetector

The scintillator is coupled to a photodetector as a second component of the acquisition chain, which converts the visible light to an electrical signal. Traditionally, photomultiplier tubes (PMTs) are incorporated as a photodetector in PET [30]. However, by technology improvement over time and considering the drawbacks of PMTs such as bulkiness and magnetic field susceptibility, avalanche photodiodes (APDs) was considered as an alternative to the PMTs [67, 68]. APDs are semiconductor photodetectors whose output signal comes from the avalanche multiplication process created by electron-hole pairs in their depletion region [69, 70]. Despite significant progress, APDs are not a perfect match as an alternative for PMTs due to their limited gain and challenging operating conditions due to the presence of electronic noise. Hence, silicon photomultipliers (SiPMs), which are composed of a 2D array of single avalanche diodes (SPADs) overcome most of the limitations of APDs. Each diode is tied in parallel through a quenching resistor to a common node of small microcells operated in Geiger mode [67]. The desired photodetector properties are listed below:

- Fast response for high CTR and efficient discrimination of random coincidences.
- High conversion efficiency of visible photons to charge.
- Insensitive to magnetic field for PET-MRI applications.
- Low noise performance to provide high SNR.

The compact geometry, high gain, and photo detection efficiency, along with the fact that they are insensitive to magnetic fields, make SiPMs a prominent choice as a photosensor in modern scanners [16, 67, 71]. Recent studies show that SiPM technology has evolved towards superior performance in terms of timing efficiency that can possibly revolutionize PET imaging [34, 35].

Electronics

The electrical signal produced by the photodetector must be processed by an appropriate low noise electronics block [72]. The electronic circuit should perform two tasks: first, converting the charges to a voltage signal; second, measuring the time and the energy of the events, registering the crystal identification (ID) and rejecting the events outside a prespecified energy window, sorting events chronologically for coincidence selection, and random estimation. Therefore, the generated exponential signal with decay time τ from the photodetector is subsequently transferred to a charge sensitive pre-amplifier that converts the charge pulse to a voltage pulse. This signal is then sampled and shaped as needed, and both the time and energy are measured. The event data consisting of the timestamp,

the energy and pixel ID are sent to a coincidence processing unit where the difference between the arrival time of the pulses is calculated and used to discriminate between coincidences by comparing with a reference coincidence time window. Figure 2.4 depicts how a coincidence sorter unit works. The coincidence time window is chosen based on the timing performance of the scanner that depends on the decay time of the scintillator, noise in the photodetector and the signal processing unit.

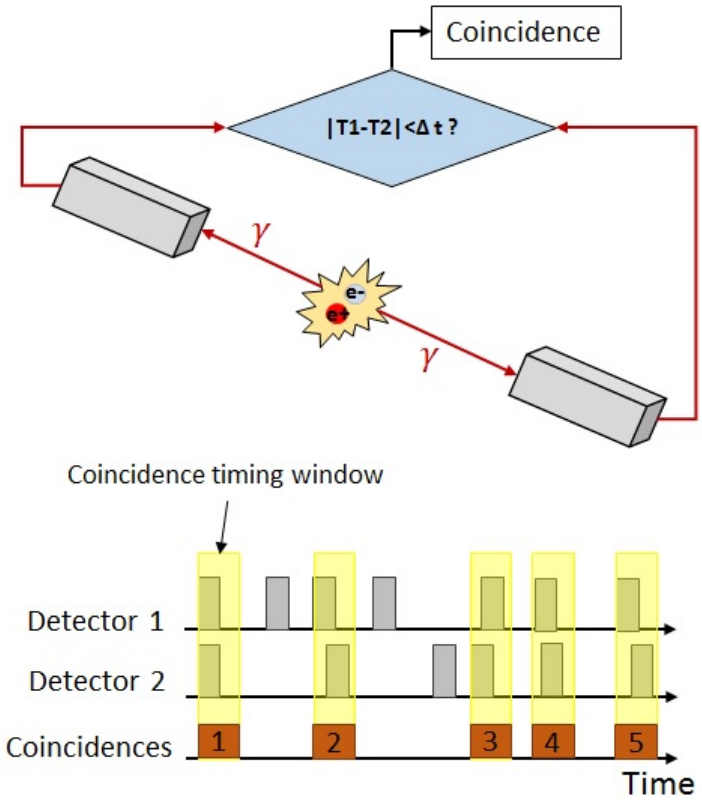

Figure 2.4 Coincidence timing unit functionality.

This unit may classify the events as trues and randoms in a delayed time window (section 2.1.3).

2.1.5 Image Formation and Corrections

Once the coincidence criterion is applied to the signal, the data are stored and either binned in a sinogram or registered event by event in a file for further processing. As these data are distorted by physical phenomena such as variations in efficiency of detector pairs, random coincidences, scattered coincidences, and photon attenuation, some corrections are required before or while performing image reconstruction. These phenomena are presented in the following sections.

Attenuation Correction

When a 511 keV photon impinges on the crystal, it may either undergo one or a mixture of interaction types (*e.g.* photoelectric absorption and Compton scattering), or may escape even without any interactions or mixture of the interactions. However, before reaching the crystal the annihilation photons pass through the subject that is being imaged, which attenuates the photons. Hence, a linear attenuation coefficient that is dependent on the energy of the incident photon and also the atomic number and density of the absorber material is used to measure the transmitted photon by

$$I = I_0 e^{-\mu_l L}, \tag{2.4}$$

where μ_l is the attenuation coefficient, I_0 is the incident intensity and L is the thickness of the material. For a photon in coincidence, both traversing different thicknesses of tissue to reach the detector pair, such as L_1 and L_2, the probability of coincidence detection is given by

$$P = e^{-\mu L_1} \times e^{-\mu L_2}, \tag{2.5}$$

where μ is the attenuation coefficient of the tissue and L_1 and L_2 are pathlengths travelled by each of the photons. The attenuation factor in PET for a given LOR is independent of the emission point and relies only on the distance traveled by the photon within the medium. Hence, a common approach to perform the attenuation correction is to find the attenuation map from the emission image and apply the correction as a multiplicative factor in the reconstruction process [73]. This correction has to be carried out to have a quantitative image and is less important in case of small animal imaging. It is, however, a must do as the subject size increases specially for clinical whole body imaging [74].

Scatter Correction

After annihilation, some photons may undergo scattering in the subject before reaching the detectors and partially lose their energy depending on their scattering angle. However, since most photons are forward scattered, they will mostly fall within the energy window. Thus they will be registered causing scattered coincidence events that increase scattering noise in the image. Scattering can also happen in-between detectors which is called inter-crystal scattering. Such scattering may lead to the selection of the wrong LOR, thus mispositioning the associated event. Contrary to scatter in the patient, these inter-crystal scatter events tend to affect the image sharpness [75]. Choosing the lower energy threshold high enough will mitigate this effect by rejecting most scattered photons to produce a sharper image [76, 77], at the cost of losing counting statistics. Many approaches have

been developed to correct for scattering effects. However each has shortcomings making scatter correction a challenge [78, 79].

The most commonly used scatter correction technique is the single scatter simulation (SSS) method [80] which estimates the single scanner events using the emission distribution and the attenuation image. This technique applies the scatter estimate during the reconstruction as an additive factor. In general, scatter correction can be conducted before proceeding to the image reconstruction or during reconstruction when iterative image reconstruction techniques are used.

Random Coincidences Correction

Random coincidences are the source of background counts in an image resulting in a lower contrast. The rate of random coincidences on a given LOR connecting detectors i and j is given by

$$R_{ij} = 2\Delta t S_i S_j \tag{2.6}$$

where $2\Delta t$ is the coincidence time window and S_i and S_j are single photon rates in detectors i and j, respectively. Hence, by choosing a coincidence time window as narrow as possible and lowering the single photon rates, the effect of random coincidences can be diminished. This highlights the importance of using fast crystals and electronics in PET. The correction for random coincidences can be done either by using a delayed coincidence window or the single event rate estimation and prior to or during the image reconstruction [81].

Image Formation

The ultimate goal of PET is to make an accurate image of the distribution of the radiotracer in the subject. After all corrections are applied, the data is fed to an algorithm to reconstruct the image. Image reconstruction techniques in PET divided into three classes: analytic, iterative and matrix-based. Matrix-based methods are computationally heavy and rarely used in PET scanners [82, 83]. In analytic methods, LORs are equally back-projected on all image voxels along the LOR for each projection angle. The data are also filtered before back-projection and then the contribution of all angles around the subject are summed up to form the image. Analytic methods are traditionally used in obtaining PET images as they are fast and linear, but are not the best-suited for highly pixelated scanners because sampling nonuniformities and missing pixels create imaging artifacts. Iterative methods have thus become more and more popular as they handle better the low statistics conditions and missing pixels. The iterative algorithms are divided into two groups: first, maximum likelihood expectation maximization (MLEM), second, ordered subset expectation maximization (OSEM). In the latter, the data is divided into subsets

and the image is updated after a specific number of subsets; this process accelerates the reconstruction process.

2.1.6 Conclusion

PET relies on injecting a positron emitting radionuclide compound into the subject. This leads to the production of pairs of back-to-back 511 keV creating photons simultaneously by annihilation of positrons with electrons in the medium. Subsequently, each 511 keV photon in such a pair is detected by the acquisition chain including the scintillator, photodetector, and electronics which were discussed individually in this chapter. The physical principles of PET, including radionuclide decay, radiation interactions, and radiation detection along with different types of coincidences must be taken into account. Moreover, as the ultimate goal of every scanner is to record meaningful data for diagnostic purposes, the formation of quantitative images is required. Therefore, detection efficiency variations between detector elements, random and scatter coincidences that are recorded besides true coincidence events, and photon attenuation can induce some deterioration on the data set and impair the image quality. These effects need to be corrected before or during image reconstruction.

In conventional PET, due to the uniform location probability along the LOR, it is not possible to find where an annihilation occurs. This brings up the emergence of a new generation of PET scanners, called time-of-flight (TOF) PET, which is presented in the following section.

2.2 Time-of-Flight PET

TOF-PET scanners have been introduced in the 1980s whereby the location of annihilation along the LOR is determined by the difference of the arrival times of the two photons [85], as measured by

$$\Delta x = \frac{\Delta t \times c}{2}, \tag{2.7}$$

where c is the speed of light ($3 \times 10^{11}\ \frac{mm}{s}$), Δt is the difference of the arrival time, also known as coincidence time resolution (CTR), and Δx is the position error along the LOR (Figure 2.5b). This information is employed in the reconstruction process by applying a gaussian kernel with the width of $2\Delta x$ on a given LOR. Without timing information, all the pixels along the LOR must be given the same probability of being the actual emission point as shown in Figure 2.5a; this is the case in conventional PET scanners. Contrary to conventional PET, TOF PET reduces the noise in the reconstructed image [85, 86], since the statistical fluctuations along the LOR is limited to the number of pixels under the TOF response (Figure 2.5a) [29, 87, 88].

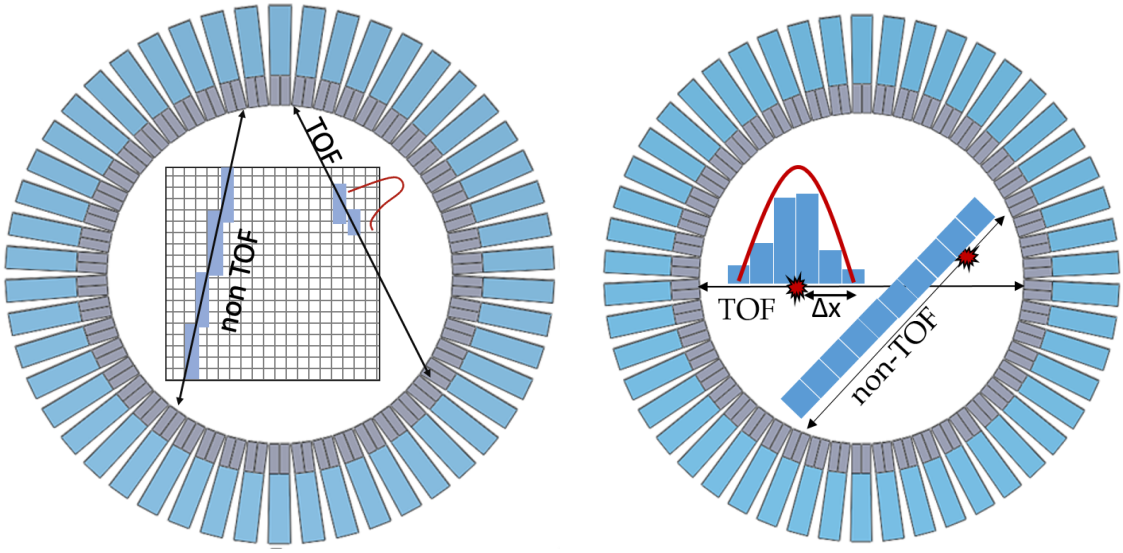

(a) (b)

Figure 2.5 Benefits of TOF over non-TOF PET. a) Highlighted pixels are contributing to image for either TOF and non-TOF PET, b) Probability distribution for TOF and non-TOF PET.

This benefit of TOF scanner translates into decreased patient radiation dose, shorter scan time, and increased small lesion detectability [18, 29, 33, 89]. The induced gain by employing TOF was proved [12, 85] by defining the ratio of the signal-to-noise (SNR) for PET scanners as

$$SNR = k(n_c)^{-1/4}(n_t)^{1/2} \tag{2.8}$$

where k is the reconstruction factor, n_c is the number of resolution cells, and n_t is the number of detected events. For same counts, a TOF capable system reduces the number of effective resolution element based on the location uncertainty calculated by knowing timing performance given by

$$n_{TOF} = \pi(\frac{\Delta x}{2})^2 \div d^2 \xrightarrow{Substituting\ in\ equation\ 2.8} SNR_{TOF} = k(\pi(\frac{\Delta x}{2d})^2)^{-1/4}(n_t)^{1/2} \tag{2.9}$$

where d is the scanner resolution and Δx is a location uncertainty calculated from equation 2.7. For non-TOF scanner, this is given by

$$n_{non-TOF} = \pi(\frac{D}{2})^2 \div d^2 \xrightarrow{Substituting\ in\ equation\ 2.8} SNR_{non-TOF} = k(\pi(\frac{D}{2d})^2)^{-1/4}(n_t)^{1/2} \tag{2.10}$$

where D is the diameter of the object in the FOV. This translates into a gain as

$$TOF_{\text{gain}} = \frac{SNR_{\text{TOF}}}{SNR_{\text{non-TOF}}} = (\frac{\Delta x^2}{D^2})^{-1/4} = \sqrt{\frac{D}{\Delta x}}, \tag{2.11}$$

The advantage of TOF PET over conventional PET can also be expressed as multiplicative reduction noise factor [85] given by

$$G = \frac{2 \times D}{c \times \Delta t}, \tag{2.12}$$

with G also being called the sensitivity gain. The sensitivity gain shows that the TOF benefits will improve for larger object size (D) and better arrival time difference (Δt).

Based on equation 2.7, detecting a 1.5 mm diameter object requires a 10 ps CTR. If the CTR of 10 ps can be achieved the image reconstruction could be avoided as claimed by the 10 ps worldwide challenge [90, 91], since the actual point of emission is estimated within 1.5 mm along the LOR. Moreover, the improvement in CTR mitigates the impact of data inconsistencies on image quality [14, 18–22, 85].

2.2.1 Coincidence Time Resolution and its Dependencies

The coincidence time resolution (CTR) is a key parameter for TOF PET scanners as it contributes to CNR performance by limiting the noise contamination in the reconstructed image. Therefore, TOF PET scanners require precise CTR to increase the ability to tag the location of the annihilation along the LOR, thus increasing the CNR compared to conventional PET. CTR is determined as the quadratic sum of the uncertainties contributing to the time performance in the acquisition chain in terms of how fast the data can be read, processed and registered [33, 62, 92–94]. Figure 2.6 shows how the different components involved in the detection process across the acquisition chain contribute to the CTR.

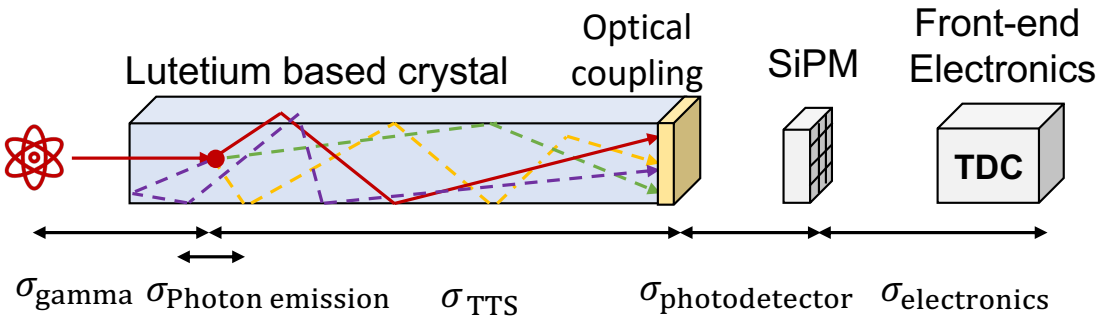

Figure 2.6 A typical time chain.

Timing uncertainties in scintillators

The choice of scintillator dominates the time performance of a scanner as it affects the time chain with three components as shown in Figure 2.6. These components are listed as follows.

- σ_{Gamma}: Variations of the location of the interaction within the scintillator induces a jitter that resulting from the bias introduced by the propagation time of the gamma in the crystal relative to the propagation time of scintillation photons towards the photodetector [21, 95]. This effect becomes significant for CTRs below $\sim$ 50 - 75 ps depending on the crystal length.
- $\sigma_{\text{Photon emission}}$: The inefficiencies in emission time of optical photons is the time it takes by the scintillation process to emit the visible light. It is dependent on the light yield, rise time, and decay time of the scintillator. Hence, the faster and brighter crystals shall be selected to reduce photostatistical timing jitter. This process normally takes a few nano seconds and can be accelerated by employing Cherenkov photons down to a few picoseconds [17].
- σ_{TTS}: The photon transit time spread (TTS) from the emission point to the photodetector is a function of crystal length as it affects the propagation time of the photons and thus the timing precision. It is also dependent on the inconsistencies of refraction index from scintillator to the light guide (optical coupling) and also the photodetector [96]. The crystals used in PET are normally long and thin and attached to a photodetector on one end. This configuration increases the travel path and exacerbates the number of photon reflections before reaching the photodetector surface, resulting in degraded light collection efficiency [93, 97, 98] and poorer CTR [32, 33, 86, 99, 100].

Timing uncertainty in photodetector

How fast and how efficiently can photodetectors convert the scintillation light into an electrical signal affects the timing performance. The photodetector contributes to the time chain as explained below.

- $\sigma_{\text{Photodetector}}$: The time it takes when a scintillation photon reaches the photodetector until the production of photoelectrons that eventually leads to an electrical signal is referred to as the light transfer efficiency of the photodetector. This process affects the time chain by the amount of detected photons that is a function of the photodetector active surface, variation of the photostatistics and how fast the de-

tected photon generates a signal. Recently, SiPMs have become the photodetector of choice due to their short timing performance and relatively good quantum efficiency. A recent study shows promising results on reducing $\sigma_{\text{Photodetector}}$ down to 7.8 ps [34].

Timing uncertainty in electronics

The approach that is employed to convert the analog electrical signal coming from the photodetector into the time signal plays a role in the timing performance in terms of how efficient the electronic works as regards a fast time response, low noise, and high gain. Traditionally, a time to digital convertor (TDC) is used with SiPMs or SPADs to measure the arrival time of the photons. However, other methods such as constant fraction discrimination, and advanced signal processing tools can be alternatively used [35].

- $\sigma_{\text{Electronic}}$: The timing jitter that is induced to the signal by the electronic block [101].

The overall CTR of a detector can be determined by the full-width half-maximum (FWHM) or σ_{t} in the time stamp distribution [93, 102]. Timing measurements are done by evaluating the point where the signal intercepts with a voltage threshold [103, 104] (Figure 2.7). At this point, the noise existing on the signal has an impact on the CTR through the signal slope that is given by

$$\sigma_{\text{t}} = \frac{\sqrt{{\sigma_{\text{Gamma}}}^2 + {\sigma_{\text{Photon emission}}}^2 + {\sigma_{\text{TTS}}}^2 + {\sigma_{\text{Photodetector}}}^2 + {\sigma_{\text{Electronics}}}^2}}{\frac{dv}{dt}\,|_{\text{threshold crossing}}}, \tag{2.13}$$

where σ_{Gamma}, $\sigma_{\text{Photon emission}}$ and σ_{TTS} are the uncertainties induced by the scintillator, $\sigma_{\text{Photodetector}}$ is the error due to the photodetector response and $\sigma_{\text{Electronics}}$ is the error resulting from electronic measurements. The steeper the rising edge of the signal in Figure 2.7, the better the timing resolution. Hence, the smaller the value of the CTR, the better the ability of the system to discern between the arrival times of the photons.

A high timing performance leads to better localization of the annihilation point along the LOR and allows to reduce the random rate; thus results in reducing background noise in the image and finally enhancing the CNR performance. This benefit makes TOF technology to be the center of the scanner development research and highly desirable for current and also future manufacturing of PET scanners.

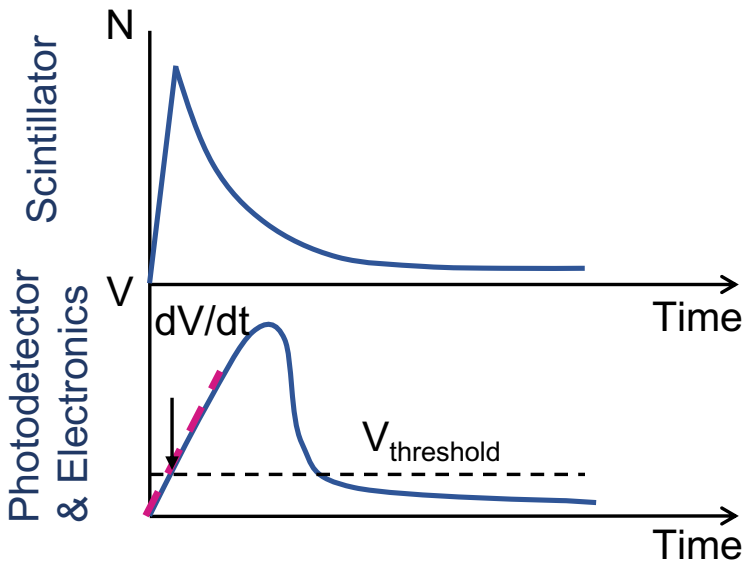

Figure 2.7 Time signal from scintillator, photodetector and electronic that is used to measure the CTR.

2.2.2 TOF Benefits

TOF PET has been thoroughly investigated at the clinical level [41, 105–107] and its main benefits include the reduction of scan time or injected dose, and enhanced small lesion detectability by reducing background noise [14, 18, 20]. However, researchers have shown that employing TOF capability improves image quality in multi-modality such as PET/MRI where TOF information facilitates the attenuation correction and reduces the impact of metal induced artifacts [108–110]. In addition, TOF reconstruction is less prone to errors and more robust to inconsistent data [86, 111, 112].

At the preclinical level, however, TOF was not investigated as the CTRs obtained are not good enough to have an impact. This is because the FOV for these scanners are small in comparison to clinical scanners, resulting in the currently achieved TOF resolution insufficient to procure any gain according to equation 2.12. Nevertheless, TOF technology is progressing steadily, approaching 100 ps timing resolutions, which is sufficient to provide a location accuracy of 1.5 cm in the FOV, (equation 2.7) [113, 114]. Moreover, state-of-the-art timing performance reported in laboratory measurements reach between 30 to 100 ps with crystal lengths of 3 to 20 mm [17, 91, 113–117]. The potential advantages of such improved timing performance would deserve further investigation for the implementation of TOF in preclinical PET.

2.2.3 Conclusion

This section emphasized that fast timing information can be used to calculate the emission distance along the LOR. This gave rise to the new generation of TOF-PET scanners, encoding the arrival time difference of coincident photons in the image reconstruction algorithm. This information is used to localize the emission point, thus leading to improved CNR in reconstructed images by reducing statistical noise. Including TOF information leads to increased small lesion detectability and reduced scan time or injected dose. Having TOF-PET capability also appears of high interest for small animal imaging to discriminate between tiny organs of animal models. This along with the recent progress in TOF resolution provide an incentive to study the benefits of TOF for small animal scanners. Therefore, the choice of design parameters that affect the small animal PET scanner performance and image quality should be studied in the context of ultrafast TOF timing. This is the subject that will be discussed in the next section.

2.3 Image Quality Parameters

The most important factors affecting image quality in PET scanners are sensitivity, spatial resolution and contrast-to-noise ratio (CNR). To have a reliable image, all of the mentioned parameters should be optimized. However, these parameters are interconnected and several design factors, such as detection efficiency, energy resolution, noise equivalent count, *etc.* have influenced the image quality in regard with these parameters. Therefore, the physical parameters of image quality along with their dependencies are discussed in this section.

2.3.1 Sensitivity

System sensitivity plays an important role in CNR performance due to the fact that it is directly contributing to the counting statistics. The number of counts per time unit (in cps) per unit of activity (in Bq) is defined as the absolute sensitivity of a scanner and is expressed theoretically to detect the annihilation photons emitted followed by a disintegration [25] as

$$S = \varepsilon^2 \times \Omega, \tag{2.14}$$

where ε is the detector intrinsic efficiency, and Ω is the geometric detection efficiency. High sensitivity is highly desirable as it increases the statistical quality of the data that is required for quantitative imaging. A scanner with high sensitivity allows to visualize organs with small uptakes or small animals with a very low amount of radiopharmaceutical. The coincidence efficiency is discussed in the following section.

Coincidence Efficiency As equation 2.14 shows, the absolute sensitivity or coincidence detection efficiency of a scanner is dependent on the intrinsic detection efficiency of the coincident detectors and the geometric detection efficiency. The intrinsic detection efficiency can be defined as the ability to effectively stop the incident photons and is given by

$$\varepsilon = 1 - e^{-\mu_l \times L}, \tag{2.15}$$

where μ_l is the energy-dependent linear attenuation coefficient of crystal, and L is the detector thickness. The intrinsic efficiency expresses the fraction of number of detected photons over the number of photons impinging on the crystal. The high intrinsic efficiency leads to noise reduction from counting statistics and, hence, high image SNR. The geometric efficiency is the solid angle spanned by the source over the detector and is calculated as

$$\Omega = \frac{Area}{d^2}, \tag{2.16}$$

where d is the distance between the source and detectors, and A is the area of the detector exposed to the radiation as shown in Figure 2.8. This should be summed over all possible detector pairs.

The geometric detection efficiency can be enhanced by increasing the solid angle coverage of the scanner while the intrinsic detection efficiency can be improved by choosing scintillators with a high atomic number, made of a high density material, and/or increasing crystal length, and crystal packing fraction [118–120]. The geometric detector arrangement is a

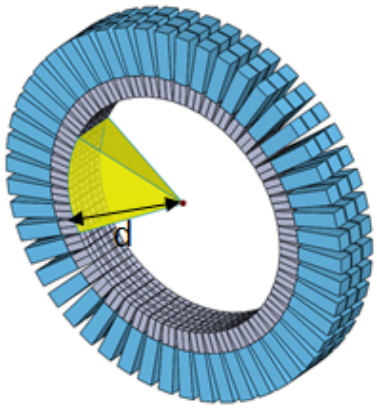

Figure 2.8 Solid angle coverage.

very important design consideration that affects significantly the detection efficiency, thus the sensitivity [121]. The fact that rectangular shape detectors are placed within a ring, makes gaps between detectors inevitable. Photons can fall into these gaps, escaping the detection process, leading to the degradation of detection efficiency, and thus sensitivity.

Two important factors that are also contributing to imaging performance are the noise equivalent count (NEC) and the energy resolution; these are discussed in the following sections.

Another important parameter affecting imaging performance is NEC which is a widely used metric representing the SNR performance of PET in terms of the three types of coincidences registered by the scanner. It provides information on the rate of true, random and scatter coincidences, and how they contribute to the image SNR [28]. The NEC provides insight into the quality of primary data and is given by

$$NEC = \frac{T^2}{T + S + R}, \tag{2.17}$$

where T, S, and R stand for true, scatter, and random coincidence count rates, respectively. The NEC does not guarantee obtaining good quality images [30], it measures the effect of random and scatter rates and the ability of the scanner to measure true coincidences [121] and is mainly dependent on the choice of the coincidence time window to reject random coincidences and the energy threshold to reject scattered photons. The activity concentration at which the NEC performance reaches the maximum value can be used to put a limit on the activity that should be injected to avoid over exposing the subject to radiations. As can be seen from the formula, to improve the NEC, the number of scatter and random coincidences should be minimized [122]. Moreover, the higher the NEC at a given injected dose, the higher the SNR obtainable by the PET scanner, which results in higher CNR performance. Knowing this optimum activity, the scan duration can be also calculated to have certain counting statististics for each bed position.The energy resolution will be discussed next.

Energy Resolution Whenever an interaction takes place (either Compton scattering or photoelectric absorption) some energy is deposited in the detector. Pulse amplitudes created by the photoelectric absorption are proportional to the energy of the incident photon (E_γ) since the whole photon energy is absorbed in such an interaction. However, photons that undergo Compton scattering deposit part of their energy in the material via Compton recoil electrons. This energy deposition is maximum when the scattering angle is equal to 180° (equation 2.2), and the energy deposited in the detector can be characterized by an energy spectrum as shown in Figure 2.9. Energies ranging from 0 to 340 keV (Compton edge) correspond to Compton scattering events. Events at 511 keV (photopeak) and in its vicinity correspond to the photoelectric interaction. In addition, some photons can undergo multiple scattering producing a distribution of pulses which are

placed in the valley between the Compton edge and the photopeak. The energy resolution

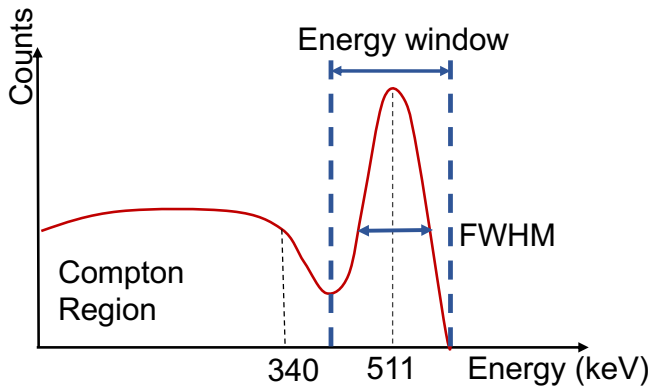

Figure 2.9 Typical energy spectrum of a 511 keV interaction in a scintillator.

is defined as the full-width at half-max (FWHM) or ΔE over the E_γ by fitting a Gaussian over the curve resulting from the contribution of five terms [123]; it is given by

$$\frac{\Delta E}{E_\gamma} = \sqrt{(\sigma_{\text{in}})^2 + (\sigma_{\text{st}})^2 + (\sigma_{\text{lt}})^2 + (\sigma_{\text{n}})^2 + (\sigma_{\text{el}})^2}, \tag{2.18}$$

where

– σ_{in} is the intrinsic energy resolution of the crystal;

– σ_{st} is the statistical term proportional to $\sigma_{\text{st}} = \frac{1}{\sqrt{\text{Number of detected photons}}}$;

– σ_{lt} is related to light transmission efficiency of both the crystal and the photodetector;

– σ_{n} is coming from the photodetector noise contribution;

– σ_{el} is electronic front-end noise.

Overall, the energy resolution represents the ability to separate true coincidences from scatter coincidences and is dependent on the choice of the scintillation material along with the light transmission efficiency and counting rate capability of the electronics [124]. In general, photons are undergoing two types of scattering either in the tissue or in-between crystals. The latter occurs when a photon escapes from a crystal and deposits its remaining energy in an adjacent crystal. The rate of inter crystal scattering is increasing if small detector elements are used since the scattered photons may escape to the adjacent crystal before releasing all of their residual energy. The probability of inter crystal scattering is increased by choosing a low density crystal [125]. In PET, scattered photons are normally rejected by choosing an energy window to allow only photoelectric events and events in their vicinity to reconstruct the image [126, 127] leading to the elimination of a large fraction of both scatter coincidences and inter crystal scattering events. However, some

researchers recently proposed methods to consider these scatter events and include them, as well as photopeak events, by lowering the energy threshold to enhance the sensitivity [128, 129] at the cost of the degradation of optimal NEC performance and CNR [70].

2.3.2 Spatial Resolution

The spatial resolution performance contributes significantly to the quality of image. The spatial resolution of the system at the center of the FOV is defined as the ability to discriminate between two adjacent objects after image formation; it is given by

$$S = k\sqrt{(\sigma_{\text{det}})^2 + (\sigma_{\text{positron range}})^2 + (\sigma_{\text{acolinearity}})^2 + (\sigma_{\text{decoding}})^2}, \tag{2.19}$$

where k is the reconstruction factor, $\sigma_{\text{positron range}}$ and $\sigma_{\text{acolinearity}}$ are the physical limitations originating from positron range and acolinearity as shown in Figure 2.10, σ_{det} is associated with impact of crystal dimensions on the resolution, and σ_{decoding} is associated to how the photodetector reads the crystal signal. Each of these uncertainties will now be discussed.

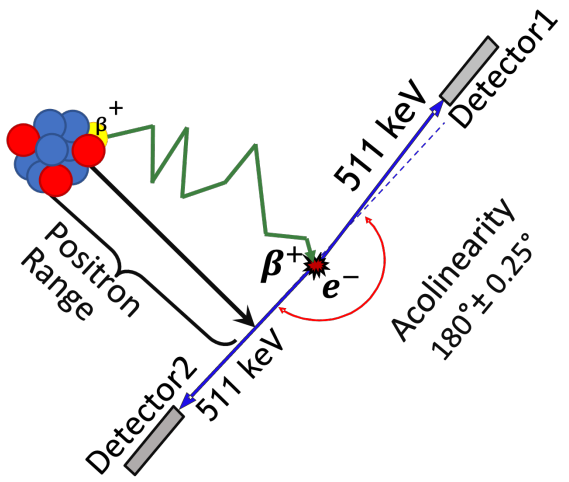

Figure 2.10 Physical phenomena contributing to spatial resolution performance: positron range and acolinearity.

– **Crystal Resolution:** This factor is presented as σ_{det} in equation 2.19 and is calculated by

$$\sigma_{\text{det}} = \frac{d}{2} \times (\cos\theta + \frac{L}{d}\sin\theta), \tag{2.20}$$

where d is the crystal cross section, L is the crystal length and θ is the incident photon angle for the sources in the periphery. If the source is centered in the FOV, θ is zero and the spatial resolution is calculated by the point spread function of the two detectors which

is equal to the width of the crystal divided by two [130]. For sources in the periphery, the resolution is degraded also by the crystal length and the incident angle that together affect the spatial resolution radially. This refers to the depth at which the photon travels into the crystal before depositing its energy. So, when the source is off-centered, photons enter crystals with oblique angles resulting in the degradation of the spatial resolution in the periphery and the creation of a parallax error, Figure 2.11 [31, 131]. Some approaches have been proposed to overcome the parallax error by designing scanners that are equipped with depth-of-interaction (DOI) capability such as double-sided readout, using phoswich detectors, *etc.*. However, the proposed methods are either costly or hard to implement [97, 118, 132–136]. Another way to mitigate the effect of parallax error is by choosing crystals with a short length.

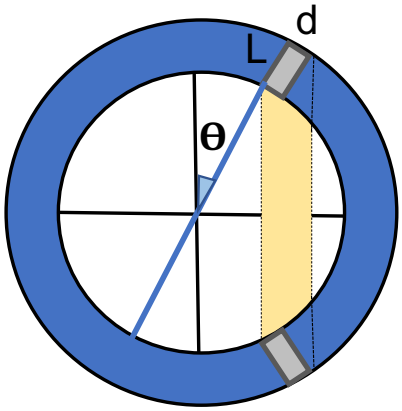

Figure 2.11 Parallax effect.

Positron Range: The $\sigma_{\text{positron range}}$ is the error coming from the distance that the positron travels before annihilating with a surrounding electron and is shown in Figure 2.10. This distance depends on the emission energy of the positron and varies for different radionuclides.

Acolinearity: The $\sigma_{\text{acolinearity}}$ is the uncertainty affecting the spatial resolution performance through the misalignment of the annihilation photons of $\pm$ 0.25° (Figure 2.10). The misalignment comes from the residual momentum of the positron at the annihilation, and affects spatial resolution by

$$\sigma_{\text{acolinearity}} = 0.5 \times D \times \tan(0.25^\circ) \sim 0.0022 \times D, \tag{2.21}$$

where D is the scanner diameter. The uncertainties from the positron range and acolinearity are physical limitations [137] and exist for any scanner regardless of the detector arrangement.

Decoding Factor: The decoding factor (σ_{decoding}) is determined by the type of photodetector and its connection to the crystal array. Whenever a crystal is read by an individual photodetector, the coding error is equal to zero. However if a group of crystals are connected to a photodetector, an uncertainty is induced by the multiplexing factor in the crystal identification, resulting in some resolution degradation.

Recontruction Factor: k is related to the choice of image reconstruction algorithm imposing resolution degradation on the image and can have a value between $1.1 < k < 1.3$ [23]. However, when estimating the intrinsic (non-reconstructed) spatial resolution, this factor is set equal to one ($k = 1$).

2.3.3 Contrast-to-Noise Ratio

High noise reduces lesion detectability as shown in Figure 2.12 a) as well as low contrast as shown in Figure 2.12 b). For this reason the ratio of contrast to noise provides for a more meaningful evaluation rather than the absolute value of each of them. So the contrast of the images acquired in PET is assessed with respect to the noise level and is expressed as the contrast-to-noise ratio (CNR). Thus, the CNR is a metric that represents signal

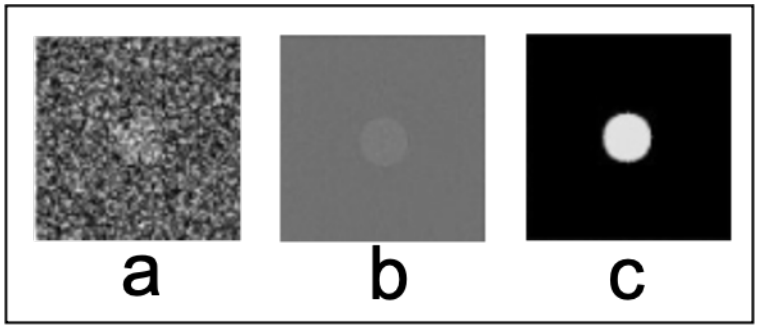

Figure 2.12 Image contrast-to-noise ratio, a) Image with high noise and low contrast, b) Image with low noise and low contrast, and c) Image with high contrast and low noise.

levels in the presence of noise in the image. As illustrated in Figure 2.12 c), the CNR is maximum as the contrast is high and the noise is low in the image and can be measured using equation 1.1.

The CNR is a key parameter for the image as it demonstrates the amplitude of the signal with respect to its surrounding medium and is highly dependent on the presence of noise in the image that was registered as a background signal. Even if the noise is low, the lack of counts can result in low contrast thus missing a lesion. Hence, a high CNR is crucial

to enhance small lesion detectability in the image. Therefore, to obtain a clear image, the CNR should be high enough along with spatial resolution and sensitivity.

The Rose model developed by Albert Rose for visual perception is the most widespread model that relates the resolution, noise and contrast based on Poisson statistics [138]. Rose defined a quantitative limit of 5 on CNR. This means that if the CNR of an object is found to be 5 or above, then the object is detectable.

Some other definitions have been proposed for the CNR evaluation [22, 86, 139, 140], and also some researchers employ the CNR definition but refer to it as SNR [107, 141]. This being said, equation 1.1 is the only one that is compatible with the Rose model and is used commonly for CNR evaluation [142, 143].

In general, parameters affecting the CNR performance of a scanner can be divided into two subsets: intrinsic and extrinsic parameters. Intrinsic parameters result from the choice of radiotracer as well as the physiology and biology and the size of the target tissue that affects the count density. Extrinsic parameters affecting the CNR are photon scatter, random coincidences, sensitivity, and TOF capability [85]. These dependencies make the CNR a parameter difficult to estimate at design stage.

2.3.4 Trade-Offs in Designing a Scanner

While designing a scanner, many trade-offs should be considered coming from limitations imposed by the physical phenomena, available scintillators, photodetectors, electronics, and cost. A detailed image can be obtained by high spatial resolution, high CNR and adequate counting statistics. Hence, scanner developers tend to ideally preserve the parameters contributing to high performance of each of the image quality parameters. Nevertheless, this task is impossible in practice as these parameters have interdependencies and designers have to prioritize one or two image quality parameters and sacrifice the other/others. Therefore, to come up with the best possible outcome, it is vitally important to find a balance point that leads to the best performance of the scanner to obtain a detailed image.

Having a highly sensitive scanner is desirable to allow for measuring low activity concentration, in particular, in small animal imaging. So, it would be ideal to have a large monolithic crystal or some slabs of crystals connected to the detector matrices to avoid the slipping of photons through gaps between crystals and crystal blocks to enhance the sensitivity by increasing the intrinsic detection efficiency [134, 144, 145]. Although in this configuration the total photon energy is detected, a high spatial resolution is hardly achievable because the annihilation cannot be localized precisely. So, long pixelated crystals are incorporated

in the scanner making it possible to track the location where the annihilation took place leading to an improvement of the spatial resolution at the cost of degrading sensitivity. On the other hand, sensitivity can be enhanced by expanding the solid angle coverage either by decreasing the system diameter or increasing the axial FOV at the expense of higher cost [119, 121].

To provide quantitative images of a radiotracer distribution, the spatial resolution must be weighted against the CNR. Studies have shown that the smaller the crystal size, the better the spatial resolution but thin crystals are expensive to make [23, 130, 146]. Based on Equation 2.19, if pixelated photodetectors (APDs, SiPMs) are used, the coding factor is reduced to zero at the cost of incorporating high density electronics to improve the spatial resolution. When using PMTs or large area photodetectors, this factor is significantly high due to the decoding methods used to determine the location of interactions, in particular, with the increasing rate of inter crystal scatter events. The more Compton scatter occurs within the crystal arrays, the more the uncertainty of the localization is with PMTs; the coding factor is increased which results in degrading the spatial resolution. In addition, the positron range and collinearity factors are physical phenomena and cannot be neglected [137].

As mentioned earlier, another important factor affecting imaging performance is the sensitivity resulting from the application of an energy window. Besides physical constraints of the type of materials, the crystal cross section and length also affect the energy resolution. The longer the crystal, the higher its ability to stop 511 keV. However, this may also degrade the light collection efficiency and affect the energy resolution unfavourably. A good energy resolution allows for choosing a narrow energy window to reject scattered photons that are produced mainly by fabricating a thin and long crystal [147, 148]. However, if pixelated photodetectors are used, the Compton scattered photons interacting in adjacent crystals can be eliminated if their energy is lower than the applied energy threshold, and this can lead to reduced sensitivity [149]. To overcome this issue, some researchers have proposed to reduce the energy threshold allowing for more Compton scattered photons to contribute in the image along with true coincidences to compensate for sensitivity losses [128,129]. This approach degrades the NEC performance and adds background noise to the image which deteriorates the CNR performance [70].

Improving CTR will lead to a reduction of the background noise in the image originating from scatter coincidences, applied corrections, thus increasing the CNR. CTR can be improved by choosing a crystal with a short length owing to a reduced travel path that photons travel to reach the photodetector [131,150,151]. As a benefit, the effect of parallax

error is reduced as well by choosing short length crystals when ultra fast timing is available. This also improves the radial spatial resolution, though at the cost of compromising the sensitivity of the scanner [111].

Crystal light output is another important parameter that affects the CTR and energy resolution statistically [33, 152, 153]. If the light output is high, the SNR is high enough allowing for discrimination of the desired signal. The amount of light output is dependent on the choice of scintillator geometry and physical parameters along with crystal wrapping considerations [131, 154].

From the above discussion, trade-offs in the performance characteristics must be undertaken and are inevitable based on targeted applications of the system, availability of the required material, ease of implementation, and cost of the technology. As the CNR performance is dependent on design parameters, finding a balance point between these metrics, such as sensitivity, timing resolution, *etc.*, where CNR performance improves, is highly compelling.

2.3.5 Conclusion

While designing a scanner, many trade-offs should be made depending on the type of system and its applications in terms of electronics, physics, cost, *etc.* It has been discussed that there are several challenges in designing a scanner and the ultimate performance of the scanner is highly dependent on the choices that are made at the early stages of the design. Hence, decisions relating to detector parameters, electronic front end, and features of the scanner highly influence the complexity of the design and should be considered beforehand.

As mentioned, CTR is the primary factor that affects the TOF imaging performance by reducing the noise propagation that leads to an enhancement of the CNR performance. Hence, this metric should be optimized and parameters affecting it should be chosen judiciously. Whereas the first and most limiting factor in ultrafast CTR is the crystal, in particular the crystal length, one approach to improve the CTR is reducing the length of the crystal; thus improving the image quality, if sensitivity loss can be tolerated.

2.4 LabPET II Platform

The LabPET II detector was designed for the purpose of high resolution PET imaging based on an array of 4×8 $Lu_{1.9}Y_{0.1}SiO_5$:Ce (LYSO) scintillators. The first version was manufactured five years ago to image small size animals such as mice. Since the technology is fully modular, other models dedicated to rat and mid-sized animal imaging were since introduced (Figures 2.13 and 2.14). The next step is to implement the same technology

in a brain-dedicated scanner. In this platform, each scintillator is individually coupled to one of the pixels of a monolithic 4×8 APD array. Each APD has a sensitive area of 1.1×1.1 mm^2 that is spaced at a 1.2 mm pitch.

(a) Small size animal scanner (b) Mid-size animal scanner

Figure 2.13 LabPET II preclinical scanners.

The unique configuration of one-to-one coupling implemented for the LabPET II detector technology allows for optimum spatial resolution and its short crystal length allows for reduced parallax effect that altogether lead to outstanding imaging performance. Table 2.2 lists the specifications for the scanner models of LabPET II platform.

2.5 Image Performance Evaluation of Small Animal Scanners

The imaging performance of the small animal scanners was evaluated based on NEMA standard instructions for assessing image quality [155]. The phantom proposed by NEMA NU4 2008 for evaluation of the imaging performance of small animal scanners is a cylinder of 30 mm in diameter consisting of three compartments (Figure 2.15). The standard requires three sets of values to be reported:

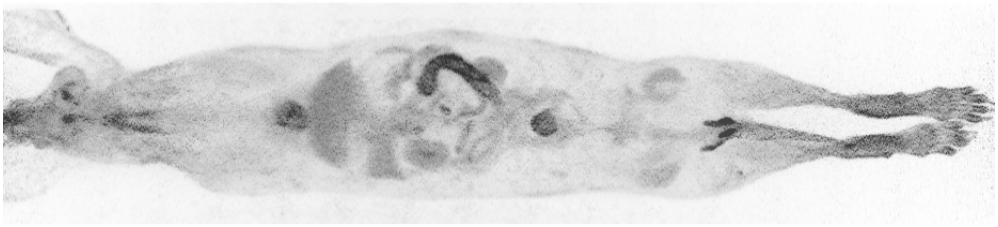

(a) After injection of FDG.

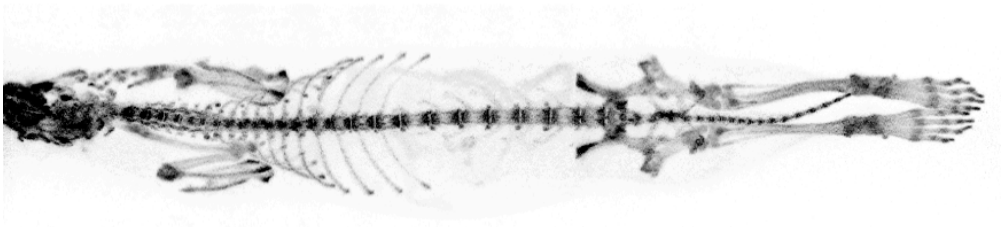

(b) After injection of NaF.

Figure 2.14 Images of a 4.1 kg New-Zealand white rabbit obtained with LabPET II mid-sized scanner.

1. The first compartment is a Plexiglass cylinder of 30 mm diameter by 20 mm length that contains 5 fillable rods with diameters of 1, 2, 3, 4 and 5 mm. This part of the phantom is employed to calculate the partial volume effect by measuring contrast recovery coefficients (CRC). The CRC associated to each rod is calculated by drawing the volume of interest (VOI) to cover the middle 10 mm long of each rod.

2. The second compartment of the phantom occupies length of 15 mm and is employed for evaluating the image uniformity. The latter is measured by drawing the VOI over 75% of the cylinder diameter and a 10 mm length to estimate the standard deviation and mean value of activity.

3. The third compartment contains two cylinders each with a diameter of 4 mm; one is vacant and the other is filled with water. This compartment is used to measure spill over ratios that show the accuracy of the applied corrections by calculating the mean of the VOI for the two cylinders divided by the mean of the uniform compartment.

NEMA has also developed phantoms for evaluating the performance of clinical scanners, however, those phantoms were not designed to thoroughly study the benefits of using TOF in PET scanners.

Table 2.2 Specifications of the scanners models based on the LabPET II platform.

	Preclinical scanners		**Clinical scanner**
	Small size (mouse/rat)	**Mid-size (rabbit, monkey)**	**Brain**
Crystal size (mm^3)	1.12 × 1.12 × 10.6/12	1.12 × 1.12 × 12	1.12 × 1.12 × 12
Scintillator number	6,144/18,432	36,864	129,024
Transaxial FOV (mm)	60/80	180	271
Axial length (mm)	50.4/103	103	235
Ring diameter (mm)	78/120	254	398

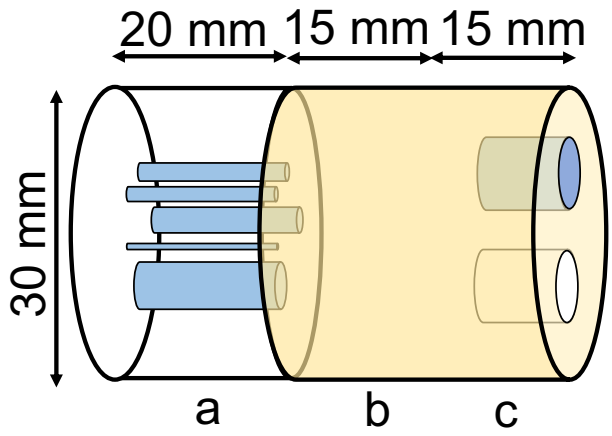

Figure 2.15 NEMA NU4 2008 image quality phantom.

2.6 Data Acquisition Method and Post-processing

2.6.1 Factorial Design

Factorial design is an approach to deal with several factors in conducting an experiment. It allows for an experimental strategy to be considered in order to vary factors together instead of one at a time. This is done by m^n experiments where n stands for the number of factors and m stands for the number of level of variations considered for each factor. Figure 2.16 shows a factorial design analysis for 3 factors, each with 2 levels of variations making a total of 2^3 analyses. By performing the full factorial design, an enormous data set will be available that can be used to extract the limitations and boundaries of the variations of the factors and also to find the trade-offs between them as suggested in the research project definition. However, when the factors have more than two levels; a

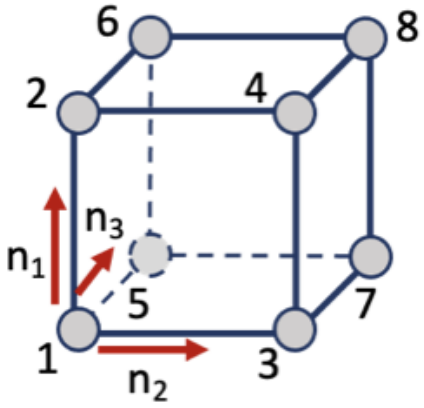

Figure 2.16 Factorial design analysis example for 3 factors, each factor having two levels of variations.

statistical model should be used to represent the experiment. Hence, a regression model can be alternatively incorporated.

2.6.2 Linear Regression Analysis

A linear regression analysis is a commonly used type of predictive analysis that attempts to model the relationship between two or more variables by a linear equation. The linear regression is expressed as,

$$Y = a + bX \tag{2.22}$$

where X is an independent variable or predictor, Y is the dependent variable to be predicted, a is the intercept and b is the slope of a line or coefficients that shows the correlation between X and Y. Correlation of each predictor should be investigated to study the association of each predictor with the dependent variable. To do that, the change of response for each variable should be investigated while keeping the other variables constant. This allows to determine the correlation significance. In the cases where the correlation is a polynomial function, a more advanced regression analysis (polynomial regression analysis) is required. By defining a proper regression model for a 3-factor factorial design, the effect of these parameters can be assessed and this leads to finding the combination that results in the optimum performance point.

The error of the estimation for the regression is measured by the mean squared error (MSE) that calculates the square of the difference between the measured and predicted values by

$$MSE(b_0, b_1, b_2, ..., b_n) = \frac{1}{m}\sum_{i=1}^{m}(y_i - Y_i)^2, \tag{2.23}$$

where m is the total number of observations, Y_i is the matrix of predicted values obtained from the regression model and y_i is the matrix of measured data from the experiment.

2.7 Conclusion

In the last decade, through the emergence of fast scintillators and detectors [71, 131], TOF-PET scanners were introduced where the location of annihilation is determined by the difference of the arrival times of the two photons. Including this information in image reconstruction significantly enhances the SNR and, hence, results in the improvement of small lesion detectability. In addition, by localizing the positron source along the LOR, TOF scanners provide benefits such as decreased patient radiation dose and a shorter scan time. Although TOF PET provides for better image quality in clinics, the CTR still needs to be improved especially to be effective for small animal imaging. While previous studies have reported the effect of almost every performance parameter separately on the image quality of TOF PET scanners, the lack of research studying the effect of the most important parameters altogether and their connection to obtain a clear image is obvious. Hence, inquiring about the optimal design considerations to maximize CNR and sensitivity could be greatly useful, particularly in the design of future generations of TOF PET scanners. This can also pave the way to develop a model that can best express how design parameters contribute to acquire high quality images in a TOF PET scanner.

CHAPTER 3

RESULTS: TOF Benefits and Trade-Offs on Image Contrast-to-Noise Ratio Performance for a Small Animal PET Scanner

Authors and affiliations:

- Nikta Zarif Yussefian : PhD student, Department of Electrical and Computer Engineering, Engineering Faculty, Université de Sherbrooke
- Maxime Toussaint : PhD student, Computer Science Department, Sciences Faculty, Université de Sherbrooke
- Émilie Gaudin : Post doctoral fellow, Department of Nuclear Medicine and Radiobiology, Faculty of Medicine and Health Sciences, Université de Sherbrooke
- Roger Lecomte : Professor, Department of Nuclear Medicine and Radiobiology, Faculty of Medicine and Health Sciences, Université de Sherbrooke
- Réjean Fontaine : Professor, Department of Electrical and Computer Engineering, Engineering Faculty, Université de Sherbrooke

Submission date: April 30, 2020

Publication date: August 21, 2020

Journal: IEEE Transactions on Radiation and Plasma Medical Sciences.

Reference: [50]

Contribution of the article: This article is the first of a series of three. The overall goal of the thesis is to maximize the CNR for small animal PET scanners. The current article contributes to the goal by studying the mandatory trade-offs and their impact on the CNR performance with focus on TOF benefits and the crystal length reduction. The

article serves as a basis for the second paper that covers the CNR derived model and is presented in the next chapter .

Small animal PET performance is critically dependent on scanner spatial resolution and the quality of the counting statistics available. The imaging performance of a PET scanner can be reduced to the concept of lesion detectability, which is the ability to distinguish an object from a noisy background. Hence at the design stage, the goal is to maximize the chance of obtaining an accurate signal and minimizing the noise to ensure high image quality. However, this is an ill-posed problem as many design parameters have multiple effects on scanner performance and thus its outcome as an image. One of these is the choice of long crystals, which promotes better statistics but degrades radial spatial resolution, and may affect TOF performance. This makes the trade-offs inevitable in the design of PET scanners.

The LabPET II technology is already optimized for spatial resolution owing to its compact design, choice of small crystal size and one-to-one crystal to APD coupling. Therefore, to optimize the CNR performance as well as the spatial resolution performance, one possible approach is to add TOF capability to the scanner. As the main goal of this thesis is to obtain a model for CNR, the first step is to study the impact of parameters affecting CNR performance. Thus, this research is conducted with two objectives. First, as the crystal length reduction improves TOF resolution as well as radial spatial resolution, this article investigates the trade-offs between crystal length, currently achieved TOF resolution and the scan time, and also how these choices have an impact on scanner imaging performance. Second, as the TOF resolution that is currently achieved is not good enough to be suitable for small animal scanners, this research studies the possible gain of implementing TOF in the LabPET II small animal scanner (mouse-version) for the first time.

French title: Avantages et compromis du TdV sur les performances du rapport contraste sur bruit de l'image pour un scanner TEP pour petits animaux

Résumé: Récemment, les scanners à temps de vol (TdV) sont devenus un courant dominant dans la recherche sur la TEP, notamment en raison de leur capacité à améliorer le rapport contraste sur bruit (RCB) de l'image. Comme le transport des photons de scintillation affecte directement la résolution temporelle de coïncidence, la diminution de la longueur des cristaux peut être envisagée pour améliorer les performances temporelles,

même au prix d'une perte de sensibilité. Cela améliorerait également la résolution spatiale radiale et réduirait le coût du matériau scintillateur en particulier dans les scanners cliniques. Cet article étudie les compromis entre le TdV, la longueur du cristal et le temps d'acquisition avec le but d'utiliser le TdV pour compenser la dégradation du RCB causée par la diminution du volume du scintillateur dans un scanner hautement pixelisé. Pour ce faire, un modèle TdV du scanner LabPET II pour petits animaux a été développé. Les coefficients de recouvrement (CR) et les performances en terme du RCB ont été étudiés à l'aide d'une analyse factorielle. Cela a permis de déterminer la limite à partir de laquelle le TdV peut être avantageux pour l'imagerie des petits animaux. Les résultats montrent que la diminution de la longueur du cristal de 2 mm améliore les performances du CR pour un tel scanner, tandis que le RCB peut être entièrement récupéré en augmentant le temps d'acquisition. Il a également été observé que le même RCB peut être atteint pour un temps d'acquisition plus court si une résolution TdV plus rapide est obtenue. L'article se termine par un résumé des compromis pour optimiser le RCB.

Abstract: Recently, time-of-flight (TOF) scanners have become a mainstream in PET research particularly owing to their ability to improve the image contrast-to-noise ratio (CNR). As the scintillation photon transport directly affects the coincidence time resolution, decreasing crystal length can be considered to improve timing performance even at the cost of sensitivity loss. This would also improve the radial spatial resolution and reduce the cost of the scintillator material particularly in clinical scanners. Hence, this paper investigates the trade-offs between TOF, crystal length, and scan time with the goal of using TOF to compensate for CNR degradation caused by decreasing the scintillator volume in a highly pixelated scanner. To do this, a TOF model of the LabPET II small animal scanner was developed. The contrast recovery coefficient (CRC) and CNR performance were investigated through a factorial design. This was followed by assessing when TOF gain may be advantageous in small animal imaging. Results show that decreasing crystal length by 2 mm improves CRC performance for such a scanner while CNR can be fully recovered by increasing scan time. It was also observed that the same CNR can be reached for a shorter acquisition time if faster TOF resolution is achieved. The paper concludes with a summary of the trade-offs to optimize the CNR.

3.1 Introduction

The time-of-flight (TOF) was introduced in positron emission tomography (PET) in the early 1980s with the goal of using timing information to localize the annihilation along the line of response (LOR) and improve the sensitivity [85]. TOF-PET has been investigated extensively in clinical studies [41, 105–107] and its identified benefits comprise the reduction of the scan time or the injected dose, as well as the suppression of random noise that affects the lesion detectability [14, 18, 20]. Furthermore, TOF reconstruction has proved to be more efficient and less sensitive to inconsistent data and artifacts [86, 111, 112]. TOF benefit is also extended to multimodality such as PET/MR where incorporating TOF information can provide an alternative for attenuation correction and lead to the reduction of metal-induced artifact [108–110]. Considering the vast benefits of TOF, researchers are now focusing on improving the coincidence time resolution (CTR) and were currently able to reduce it down to the 200-300 ps range in commercial devices [16, 156]. Nonetheless, the current state-of-the-art timing performance in the laboratories is between 30 to 100 ps and is achieved with a crystal length of 3 to 20 mm [17, 91, 113–117]. Recent studies indicate that TOF information of less than 100 ps will soon be within reach to localize lesions with 1.5 cm accuracy [113, 114].

Preclinical scanners have not yet been endowed with TOF capability as the current CTR is

not low enough to localize small animal tiny organs. Nevertheless, the currently achieved and expected time resolutions could still be advantageous to improve the image quality, in particular the contrast-to-noise ratio (CNR) since incorporating TOF information in the reconstruction allows for noise reduction.

Amongst design parameters of PET scanners, the choice of crystal material and dimensions directly impacts the scanner sensitivity and CTR [62, 157]. Several studies focused on investigating the effect of crystal cross section on scanner imaging performance [31, 33, 86, 158], while the effect of crystal length variations was rarely addressed in the literature [30, 32, 158]. The current practice is generally to use long crystals to ensure high sensitivity [31, 119], even though long crystals degrade timing performance due to increased scintillation transit time, as well as radial spatial resolution towards the periphery of the field of view (FOV) [32]. To resolve this problem, work is ongoing for designing detectors with depth-of-interaction (DOI) capability and high timing performance [159, 160], however such detectors are currently costly to design and would add complexity to the system. In recent studies it was shown that DOI correction is required for long crystals to achieve usable TOF (<50 ps) in small animal PET [95, 161], however shorter crystals alleviate the timing degradation and also provide enhanced light collection efficiency. Hence, crystal length and detection efficiency may have to be traded off with CTR, radial spatial resolution, and cost of ultrafast scintillating materials in future small animal TOF PET scanners.

The LabPET II detector technology was designed with a crystal cross section optimized to achieve sub-millimeter spatial resolution in small animal imaging. In order to further enhance the imaging performance of LabPET scanners, in particular CNR, we aim to endow the next generation with TOF capabilities. Recently, a single photon avalanche diode (SPAD) was developed in our group that achieved 7.8 ps single photon time resolution [34], which provides a strong incentive for studying TOF benefits. As the timing performance can be improved by shorter crystals, selecting the best crystal length that does not compromise the imaging performance could become a challenge. Using shorter crystals could also lead to reduced design complexity and material cost.

Thus, the motivation of this study is to investigate the trade-offs between TOF resolution, crystal length, and scan time with the goal of using TOF with the highly pixelated scanner to compensate for possible imaging performance degradation caused by reducing the crystal length and scan time. To conduct this research, we used a method called factorial design to investigate the effect of relevant factors such as crystal length, scan time, and

TOF resolution over the CNR, contrast recovery coefficients (CRC), and TOF gain. For each factor, a minimum of three levels of variations were considered and the combinations of two or multiple factors were used to study the trade-offs.

3.2 Materials and Methods

3.2.1 System Description

The mouse-version of the LabPET II scanner configuration was used as a model to investigate the trade-offs that could be considered by the implementation of fast TOF capabilities. The scanner relies on $1.12 \times 1.12 \times 10.6$ mm^3 $Lu_{1.9}Y_{0.1}SiO_5$: Ce (LYSO) scintillators [49, 162, 163] that are arranged in 4×8 arrays with one-to-one coupling to a pixelated monolithic APD array at a 1.2 mm pitch. Four of these arrays are then mounted on an interposer board to be interfaced to two 64-channel application-specific integrated circuits (ASIC). Forty eight of these modules are distributed on 4 rings of 76 mm diameter for a total of 6144 crystals (Fig. 3.1).

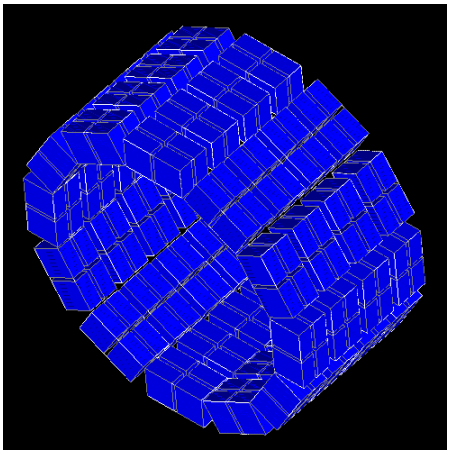

Figure 3.1 The model of the mouse-version of LabPET II.

3.2.2 Simulation Configuration

The simulations were performed with the open-source Geant4 Application for Tomographic Emission (GATE) [164] package v.8.0. The energy window and energy resolution were set to [250-650] keV and 21 %, respectively. The coincidence time window was set to 10 ns. The time resolution was set by the temporal resolution module from GATE that applies a Gaussian blurring in time domain. The LYSO intrinsic radioactivity was modelled by the noise module from GATE.

The image quality was assessed with the NEMA NU4 phantom based on a 50 mm long, 30

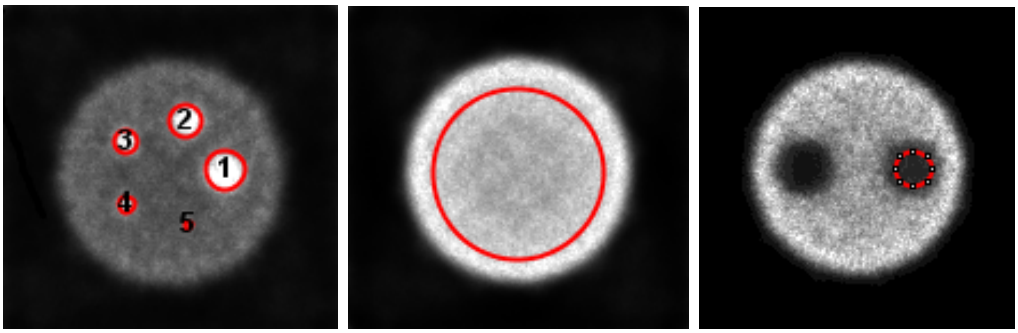

Figure 3.2 Left: ROIs for CRC analysis on 5 rods (Phantom first compartment), Middle: ROI for background measurement (Phantom central compartment), Right: ROI for spill over ratios analysis (Phantom third compartment).

mm diameter cylinder made of polymethylmethacrylate which consists of three compartments (Fig. 3.2) [155]. The first compartment includes five fillable rods that have a diameter of 1 to 5 mm (Fig. 3.2-left). The central part of the phantom is a uniform region used to quantify the uniformity by the percentage standard deviation (SD) (Fig. 3.2-middle). The rods in the first compartment and also the uniform region of the second compartment are used to determine the CRC. The third compartment consists of two vacant cylinders; one filled with air and the other filled with non-radioactive water (Fig. 3.2-right). These cylinders are used to calculate the spill over ratio (SOR).

The phantom was simulated using a uniform concentration of 0.18 MBq/cc of ^{18}F for a total activity of 3.7 MBq. To calculate the CNR, a homogenous background activity of 635 kBq is also added to the first compartment of the phantom to provide a concentration ratio of 4:1 between the rods and background.

To conduct the study, the factorial design method was used which allows for planning a simulation strategy to explore the effect of multiple independent factors on dependent performance parameters. Several levels can be also considered for each independent factor to investigate the possible change of response due to variations. Hence, the simulations were organized to investigate the impact of four main factors including crystal length, scan time, TOF (each with 3 levels), and also rod diameter (5 levels); giving the $3^3 \times 5$ possible combinations for a total of 135 configurations. Table 4.1 reports the description of the factors along with their associated levels.

The choice of the longest crystal length of 10.6 mm was made to comply with the current configuration of the LabPET II mouse scanner. The shorter crystal lengths (*e.g.* 9.6, 8.6 mm) were selected to investigate whether the improved TOF could compensate for the

Table 3.1 Trade-off factors and their levels in the factorial design

Factor	Crystal length (mm)	Scan time (minutes)	TOF (ps)	Rod diameter (mm)
				1
	8.6	6	50	2
Level	9.6	12	100	3
	10.6	20	200	4
				5

loss of detection efficiency. The choice of the 20 minutes scan time was made according to NEMA NU4 2008 instructions and the reduced values of 12 and 6 minutes were selected for the purpose of investigating the scan time reduction. The TOF resolution value of 200 ps was set in accordance with the currently achieved TOF in the state-of-the-art clinical scanners. The 100 ps value is a TOF resolution that may be reached in the foreseeable future, while 50 ps is in the range already reported for the best coincidence time resolution in the laboratories and which would be required for true small animal TOF-PET. The studies were categorized as follows:

– **Non-TOF Study:** The impact of crystal length, scan time, and rod diameter were studied for the purpose of, first investigating the CRC, uniformity, and SOR and second, investigating the trade-offs between the scan time and crystal length reduction on CNR.

– **TOF Study:** To investigate the trade-offs between TOF and scan time on CNR, the impact of time resolution and scan time at all levels were investigated for small size objects (*e.g.*, rod diameters of 2, 3, and 4 mm) with a crystal length of 8.6 mm. The trade-offs between TOF, scan time, and crystal lengths on CNR were also explored for rod diameters of 2 and 3 mm with crystal lengths of 8.6 and 10.6 mm. In addition, the gain induced by TOF resolution was assessed for a crystal length of 8.6 mm for all other configurations to study the possible advantage of currently achieved time resolution in small animal imaging.

3.2.3 Reconstruction Parameters

Images were reconstructed using ROOT output data from GATE with a voxel size of $0.3 \times 0.3 \times 1\,\mathrm{mm}^3$ with voxelization of $160 \times 160 \times 60$. The 3D MLEM algorithm Customizable and Advanced Software for Tomographic Reconstruction (CASToR) [165] was used

without post reconstruction filtering. Although no attenuation correction was performed during the reconstruction, it is not expected to affect the conclusions of the factorial analysis as all parameters have been compared on the same basis.

– **Non-TOF Reconstruction:** Images were reconstructed using multiple ray-tracing with the Siddon projector [166] so that the solid angle contribution of each event is considered in the system matrix.

– **TOF Reconstruction:** TOF reconstructions were done using the incremental Siddon line projector [167] with continuous TOF information [168].

3.2.4 Image Analysis

The CRC assessment is performed using

$$\mathrm{CRC_L} = \frac{\mathrm{Mean_L}}{\mathrm{Mean_{Unif}}}, \tag{3.1}$$

where $\mathrm{Mean_L}$ is calculated by averaging the image slices covering the central 10 mm length of the rods and placing regions of interest (ROIs) as large as the rod diameter over each source (Fig. 3.2-left). $\mathrm{Mean_{Unif}}$ is calculated by averaging over a volume of interest (VOI) encompassing 75% of active diameter transaxially by 10 mm axially in the center of the uniform region of the image quality phantom (Fig. 3.2-middle). The spill over ratio (SOR) measurement is done by averaging the central 7 mm image slices of the phantom third compartment as

$$\mathrm{SOR} = \frac{\mathrm{Mean_{Cylinder}}}{\mathrm{Mean_{Unif}}}, \tag{3.2}$$

where $\mathrm{Mean_{Cylinder}}$ is the mean of 4 mm diameter ROIs over both vacant cylinders (Fig. 3.2-right). For all CRC analysis, 30 iterations were used.

The CNR was assessed using an in-house Matlab code developed to place ROIs over the rods with the same diameters and 6 ROIs on the background as shown in Fig. 3.3. CNR evaluation was calculated by

$$\mathrm{CNR_L} = \frac{\mathrm{Mean_L} - \mathrm{Mean_{Bg}}}{\sigma_{\mathrm{Bg}}}, \tag{3.3}$$

where $\mathrm{Mean_L}$ represents the mean of each rod, while $\mathrm{Mean_{Bg}}$ and σ_{Bg} represent the overall mean and standard deviation of the six background regions in the first compartment of

the phantom, respectively. To compare the images for CNR performance in the absence

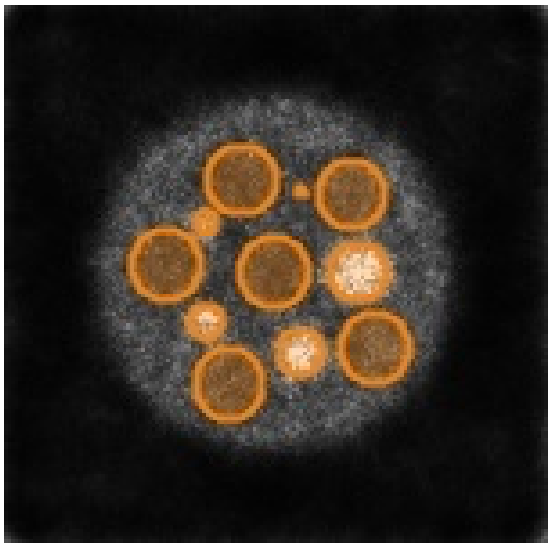

Figure 3.3 Example of reconstructed phantom transverse slice with ROIs for CNR analysis.

of TOF information, the number of iterations was adapted for each simulation until the same noise level was obtained for all images. For CNR analysis in the presence of TOF information the images were analyzed at 5 iterations.

The TOF gain was investigated by evaluating the ratio of $\frac{\mathrm{CNR_{TOF}}}{\mathrm{CNR_{non\text{-}TOF}}}$. For TOF gain evaluation the iteration that led to best CNR performance was determined and found to be between 3 to 8 iterations. The obtained ratio is compared with the theoretical TOF gain which is approximated by

$$TOF_{gain} = \sqrt{\frac{D}{\Delta x}}, \tag{3.4}$$

where D is the phantom diameter and Δx is the position uncertainty calculated from the coincidence time information by

$$\Delta x = \frac{c \times \Delta \mathrm{t}}{2}, \tag{3.5}$$

where Δt is the time resolution and c is the speed of light [85]. In another study, however, this gain is estimated by the ratio of D over 1.6 $\times \Delta x$ [169].

To speed up the simulation process, the bash scripting was used to perform the simulation with GATE and also for image reconstruction with CASToR. This was followed by performing image analysis for each image with a Matlab script.

3.3 Results

The results are listed in accordance with simulation configuration as non-TOF and TOF studies.

3.3.1 Non-TOF Study

Table 3.2 reports the NEMA image quality parameters including CRC, uniformity, and SOR for crystal lengths of 8.6, 9.6, and 10.6 mm for a scan time of 20 minutes. It is observed that there is a consistent trend towards higher CRC values as the crystal length is reduced and the improvement is slightly increasing for the smaller rod sizes (rod diameters of 1 and 2 mm in Table 3.2). This can be explained by the reduced parallax error away from the center of the FOV with shorter crystals. The CRC performance is found to be similar for scan times of 6 and 12 minutes.

Table 3.2 NEMA image quality parameters reported for crystal length of 8.6, 9.6, and 10.6 mm

Crystal length (mm)			**8.6**	**9.6**	**10.6**
Uniformity (STD,%)			8.14	8.31	8.26
Recovery coefficients	**Object (mm)**	**1**	0.42	0.40	0.38
	STD (%)		4.6%	5.0%	6.2%
		2	0.62	0.59	0.55
			5.6%	6.9%	6.7%
		3	0.73	0.70	0.69
			8.9%	10.5%	11.1%
		4	0.77	0.76	0.75
			10.1%	12.0%	14.0%
		5	0.82	0.81	0.80
			10.2%	11.7%	13.1%
Spill-over ratio		**Water**	0.13	0.14	0.14
		Air	0.25	0.25	0.26

Fig. 3.4 shows that the CNR performance improves as the crystal length is increased from 8.6 mm to 10.6 mm, especially for the larger rod diameters (solid lines). However, by reducing the scan duration from 20 minutes to 16 and 14 minutes for the 9.6 mm and

10.6 mm crystals, respectively, to match the count statistics of the 8.6 mm crystal, it is demonstrated that similar CNR values can be reached (dashed lines). Conversely, it also shows that the CNR loss due to shorter crystals can be fully compensated by increasing the scan duration.

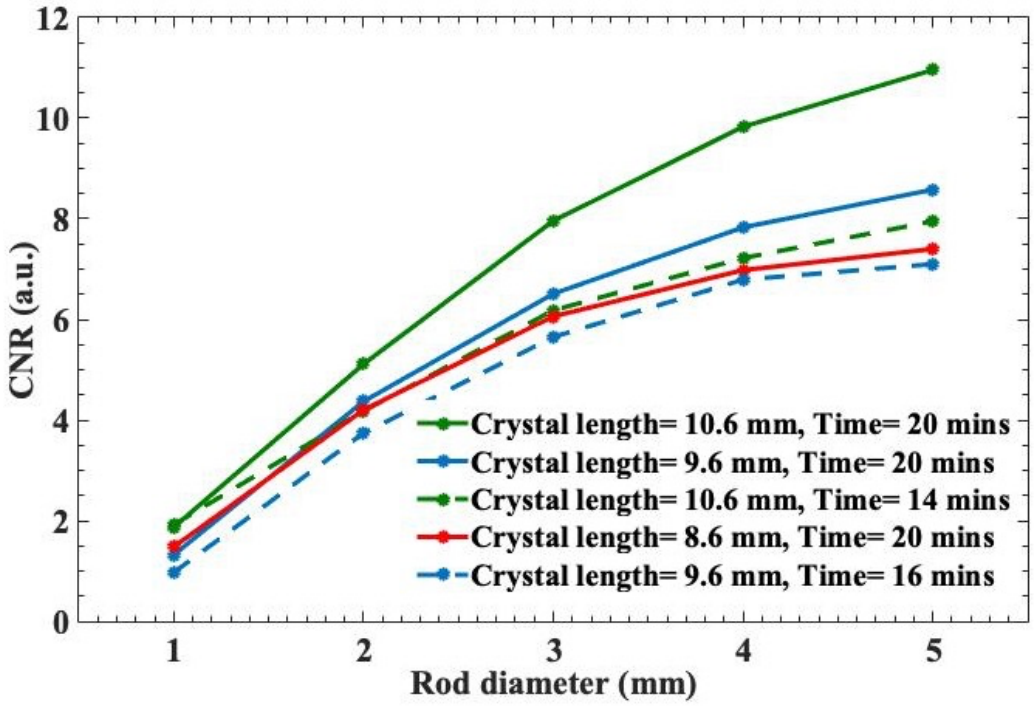

Figure 3.4 CNR as a function of rod diameters for the three crystal lengths and investigation of the trade-offs between crystal length and scan time.

3.3.2 TOF Study

Fig. 3.5 shows the trade-offs between TOF and scan time on CNR for the crystal length of 8.6 mm and for the 2, 3, and 4 mm diameter rods. As expected from theory and literature, the results show that CNR increases as the TOF resolution is improved. As an example, Fig. 3.5 shows a CNR of 4.2 obtained for both TOF resolution of 100 ps with a 12 minutes scan time as well as TOF resolution of 200 ps with a 20 minutes scan time for the 3 mm diameter rod. In addition, a similar CNR of 2.3 is achieved for the 2 mm diameter rod with TOF resolution of 50, 100, and 200 ps for the scan times of 6, 12, and 20 minutes, respectively. These results indicate that the lower statistics resulting from shorter scan times can be compensated for by including TOF information.

Fig. 3.6 depicts the trade-offs for crystal lengths of 8.6 and 10.6 mm for rod diameters of 2 and 3 mm with 6, 12, and 20 minutes scan time and TOF resolution of 50, 100, and 200 ps. The CNR with a TOF resolution of 200 ps is shown for any combinations while the bar

corresponding to the TOF resolution of 100 and 50 ps depicts the augmentation of CNR when the associated TOF resolution is used. As an example, the CNR values measured with a crystal length of 10.6 mm for a scan time of 6 minutes and rod diameter of 3 mm in Fig. 3.6 are 2.8, 3.1, and 3.4 for TOF resolution of 200, 100, and 50 ps, respectively.

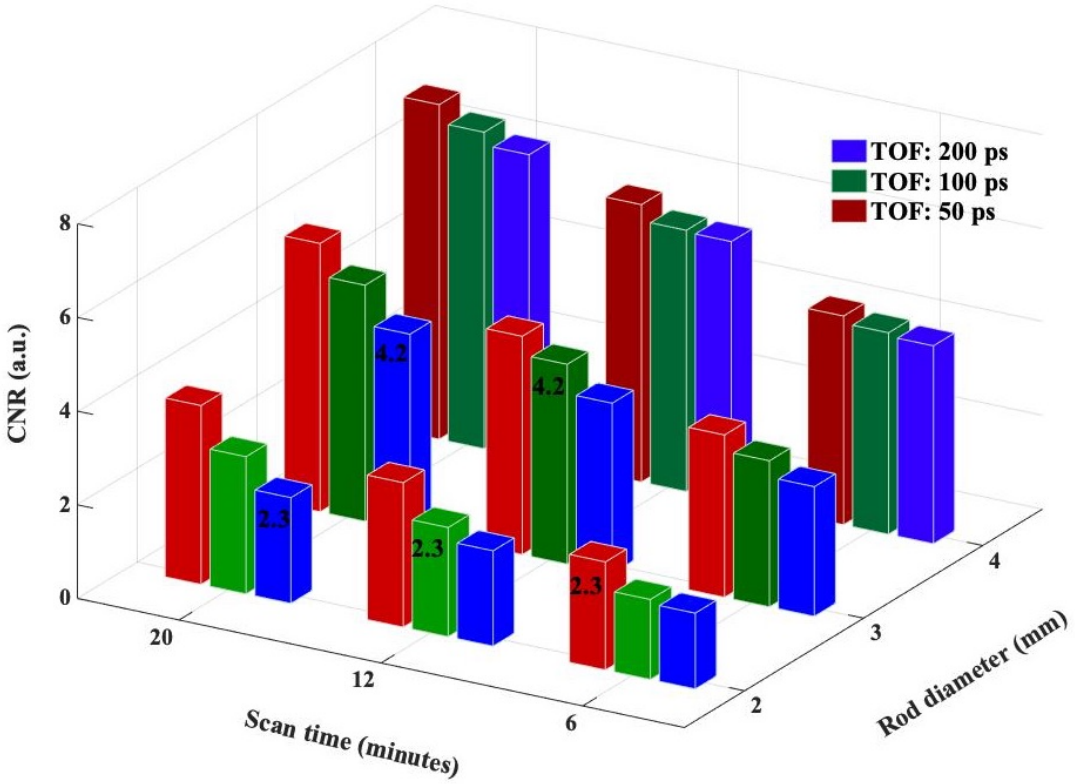

Figure 3.5 Trade-offs between scan time and TOF resolution for the 2, 3, and 4 mm objects. The number of counts are 16 M, 31 M, and 51 M for the scan time of 6, 12, and 20 minutes.

It is observed that when a TOF resolution of 200 ps is used, similar CNR values are obtained as a function of scan time and rod diameter for both crystal lengths. Hence, the observed improvement of CNR as a function of scan time is only due to higher statistics. However, when TOF improves (*i.e.* 50 ps) the CNR as a function of rod diameter and scan time is more enhanced for a crystal length of 8.6 mm rather than 10.6 mm. This enhancement of CNR occurs at a sharper rate as a function of scan time. This shows that increasing crystal length does not lead to an improvement of CNR performance in the presence of adequate statistics. Moreover, it is demonstrated that the same CNR performance can be achieved with improved TOF information and shorter crystal length. As an example, for both rods in Fig. 3.6, when the scan time of 20 minutes is incorporated, the CNR values for a crystal length of 8.6 mm with a TOF of 100 ps are equal with the values obtained with a crystal length of 10.6 mm and a TOF of 50 ps for both rod diameters.

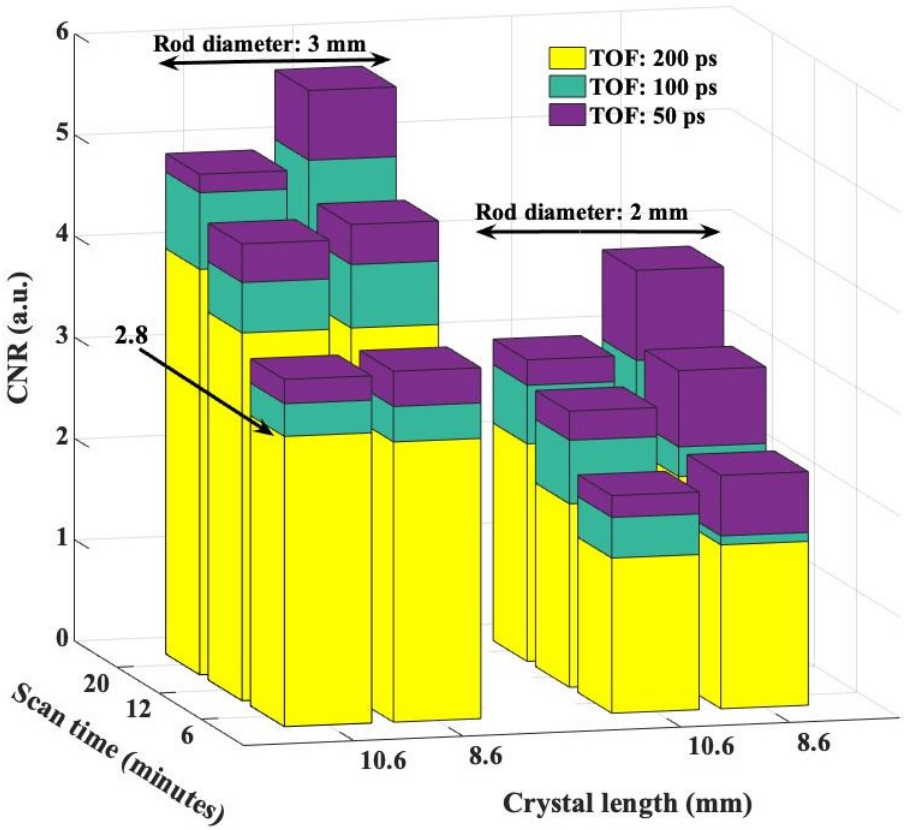

Figure 3.6 Trade-offs between crystal length, scan time, and TOF resolution for the 2 and 3 mm objects. The number of counts for crystal length of 8.6 mm and 10.6 mm are 16 M, 31 M, and 51 M, and 23 M, 46 M, and 68 M for scan times of 6, 12, and 20 minutes, respectively. The arrow shows the CNR value of 2.8 for a rod diameter of 3 mm and a crystal length of 10.6 mm.

Table 3.3 TOF gain analysis for scan time of 20 minutes

	Rod diameter (mm)	**Time resolution (ps)**		
		50	**100**	**200**
$\sqrt{\frac{D}{\Delta x}}$		2	1.4	1
$\sqrt{\frac{D}{1.6\times\Delta x}}$		1.58	1.1	0.79
$\frac{CNR_{TOF}}{CNR_{nonTOF}}$	**1**	2.62	2.46	0.91
	2	1.64	1.29	1.03
	3	1.35	1.18	1.00
	4	1.24	1.08	1.03
	5	1.18	1.10	1.04

The comparison of TOF gain with the theoretical TOF gains [85, 169] is presented in Table 3.3 for all rods at the scan time of 20 minutes and crystal length of 8.6 mm. As expected, consistent improvement is achieved with improved time resolution for each rod. However, apart from the 1 mm rod diameter, the experimental TOF gain values are more in accordance with the second derivation of the theoretical TOF gain, in particular, with time resolutions of 50 and 100 ps. This is concluded by calculating the average relative error between the experimental gain values and each of the theoretical derivations.
Fig. 3.7 shows the TOF gain for a scan time of 6, 12, and 20 minutes and a time resolution of 50, 100, and 200 ps for all rods. It can be observed that incorporating time resolution of 50 and 100 leads to gain in CNR although those TOF values are not enough to perfectly localize those objects. Moreover, Fig. 3.7 depicts that the statistics still need to be adequate to reach the expected TOF gain values. However, the gain with a time resolution of 50 ps is well above of the one obtained with a time resolution of 100 ps for any combination of rod diameter and scan time. As expected, there is no gain in incorporating time resolution of 200 ps for any configuration, as the corresponding time bin in that case is almost as large as the phantom diameter. Moreover, the effect of TOF is more significant for the low contrast lesion being 1 mm source diameter in our case.

3.4 Discussion

In this work, we investigated the trade-offs affecting image parameters, including CRC and CNR, for a mouse-version of the LabPET II scanner through a factorial design method

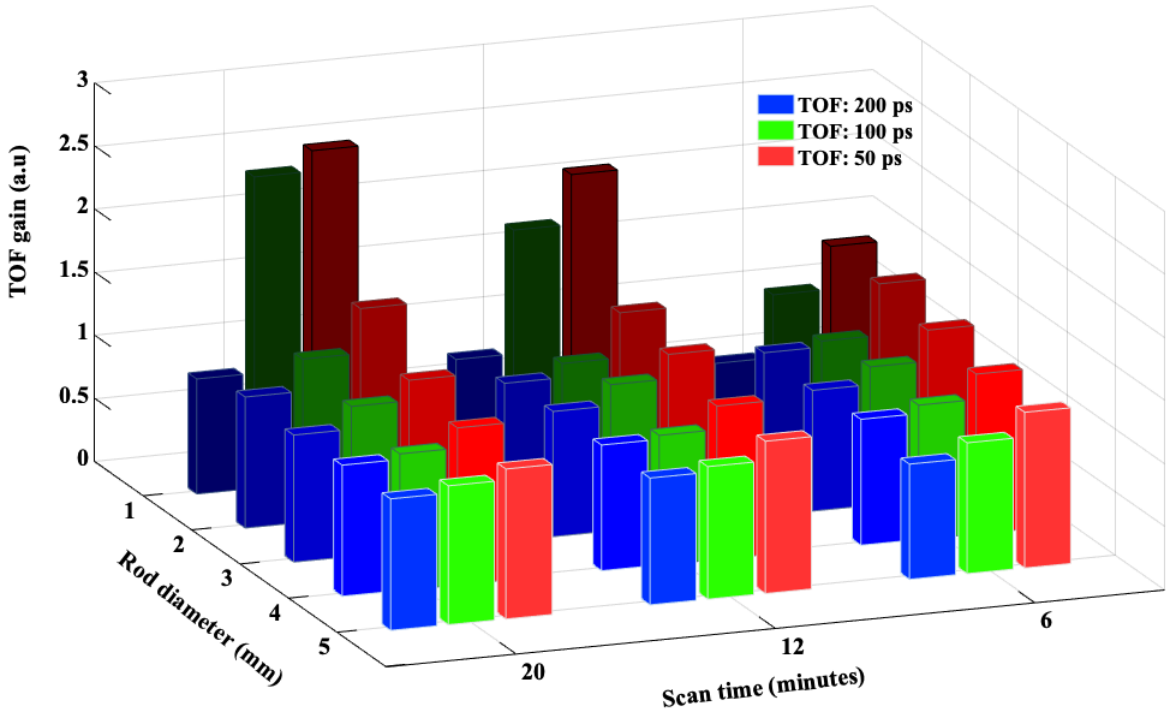

Figure 3.7 TOF gain for crystal length of 8.6 mm at timing resolution of 50, 100, and 200 ps.

by exploring the effect of four factors *e.g.* crystal length, scan time, TOF resolution, and rod diameter. Results indicate that shortening crystal length improves CRC performance, likely due to the reduction of the parallax error in the periphery [23]. However, the CRC is not a sensitive parameter to assess the image quality as a significant change was not observed in CRC performance with respect to scan time variations.

CNR performance was evaluated by changing crystal length from 8.6 mm to 10.6 mm and scan time from 14 minutes up to 20 minutes. It was observed that although CNR degrades with decreasing crystal length, consistent CNR performance is recovered if the same count statistics are incorporated in the image by increasing the scan time.

The impact of TOF and scan time were also studied on CNR. It was demonstrated that similar CNR performance can be obtained for a small animal scanner with reduced scan time if TOF resolution is improved. This is in accordance with the benefits of incorporating TOF resolution for clinical studies reported in [14, 18, 20].

Moreover, CNR performance was assessed as a function of TOF information, crystal length, and the scan time for two rod sizes. It was shown that reducing crystal length does not

necessarily degrade CNR performance when TOF information is used. This could happen due to the pixelated configuration of the scanner that provides enhanced imaging performance in comparison to other scanners. However, these results may be different if larger rod sizes are investigated as the used iteration number could affect their CNR performance adversely. Hence, this cannot lead to any conclusion on the lower limit of crystal length. Although encouraging results obtained with crystal length of 8.6 mm, it's a challenge in practice to achieve time resolution of 50 ps with LYSO crystal with the length of 8.6 mm. Hence, future research will address these issues by investigating the impact of crystal length using a wider range of variations.

Finally, the measured TOF gain was compared with theoretical derivations of TOF gain. The achieved TOF gain was in better agreement with the TOF gain derivation involving the 1.6 factor. The results are consistent with literature [170]. The TOF gain was also investigated for a small animal PET scanner and showed that incorporating TOF information leads to improved image CNR performance even at low statistics. Although CTR of 50 ps, which corresponds to a spatial uncertainty of 7.5 mm, is not enough to accurately assign the event location along the LOR, it is still better than assigning a uniform probability as in conventional PET, hence, is advantageous in the detection of small size lesions. Thus it was shown that the currently achieved TOF accuracy (15 mm corresponding to CTR of 100 ps), which in our case is similar to the half size of the phantom ($\Delta x \sim \frac{D}{2}$), already leads to a gain in imaging performance of small animal scanners. This is a promising result providing incentive to design the future generations of LabPET scanners with TOF capabilities. Altogether with the ultrafast SPADs under development [34] and optimized crystal length, significantly improved CNR performance can be expected for the future generation of LabPET scanners. Furthermore, it was observed that TOF gain is higher for the lesion with lowest contrast. Although this result is in agreement with other investigations [106, 170], the gain observed for the 1 mm rod diameter in our case may be due to the noise amplification artifact of the MLEM algorithm.

3.5 Conclusion

The trade-offs between coincidence timing resolution, crystal length, and scan time clearly showed that including TOF information in the image reconstruction can compensate for possible imaging performance degradation to obtain similar CNR values. It was also demonstrated that including TOF information allows for improved CNR performance with shorter crystal length when adequate statistics are available. These trade-offs are favorable to design the future generation of small animal TOF PET scanners with shorter

crystals. In our particular case, it would allow reducing the crystal volume by 19% without degrading CNR and CRC. Furthermore, it was shown that the TOF gain obtained with even modest coincidence time resolution can be beneficial in improving CNR performance in small animal imaging when using highly pixelated scanners. This is highly relevant for the design of future small animal PET scanners with TOF capability in order to improve their imaging performance.

CHAPTER 4

RESULTS: Predicting Small Lesion Detectability for a Small Animal PET Scanner

Authors and affiliations:

- Nikta Zarif Yussefian : PhD student, Department of Electrical and Computer Engineering, Engineering Faculty, Université de Sherbrooke
- Émilie Gaudin : Post doctoral fellow, Department of Nuclear Medicine and Radiobiology, Faculty of Medicine and Health Sciences, Université de Sherbrooke
- Roger Lecomte : Professor, Department of Nuclear Medicine and Radiobiology, Faculty of Medicine and Health Sciences, Université de Sherbrooke
- Réjean Fontaine : Professor, Department of Electrical and Computer Engineering, Engineering Faculty, Université de Sherbrooke

Submission date: May 04, 2021

Publication date: August 24, 2021

Journal: IEEE Transactions on Radiation and Plasma Medical Sciences.

Reference: [51]

Contribution of the article: This is the second article in a series of three papers. The first paper covered the trade-offs and defined the range over which TOF is effective in imaging small animals. This work focuses on the most important factors identified in the first paper and employs them to derive a CNR model for the LabPET II mouse scanner, thus contributing to the objectives of this thesis.

In the design of PET scanners, both the spatial resolution and CNR performances should be optimized to obtain meaningful, quantitative images. As the spatial resolution performance is optimized for the LabPET II technology, for designing the next generation of the scanner the focus is on improving the CNR performance. Thus, a model that would allow to estimate CNR performance at early stages of the design is desirable. In this research, a novel approach is undertaken to parameterize and derive a model to predict the CNR performance for a small animal PET scanner. To the authors' knowledge, prior to this work, no model was ever derived for the CNR performance based on design parameters.

French title: Prédiction de la détectabilité des petites lésions pour un scanner TEP pour petits animaux

Résumé: Une façon d'améliorer la détectabilité des lésions en tomographie d'émission par positrons (TEP) chez les petits animaux consisterait à améliorer la résolution temporelle de coïncidence (RTC) par rapport à l'état de l'art actuel. Cela pourrait bientôt devenir une réelle possibilité avec le lancement récent du défi mondial 10 ps. Des cristaux plus courts pourraient être favorables pour améliorer les performances temporelles en réduisant le temps de transit de la scintillation. Bien que cela se fasse au prix d'une perte de sensibilité, le gain de temps de vol (TdV) peut permettre de compenser cette perte sensibilité sans dégrader les performances d'imagerie. Comme le principal avantage du TdV est d'améliorer le rapport contraste sur bruit (RCB), il y a une motivation à évaluer les compromis entre la longueur du cristal et la résolution du TdV sur la détectabilité de lésions à l'aide d'un modèle quantitatif. Pour élaborer un tel modèle, un ensemble des simulations a été effectué sur le scanner LabPET II version souris avec GATE en suivant les normes NEMA NU4. Les images ont été obtenues à l'aide du logiciel CASToR pour la reconstruction tomographique. Le RCB a été évalué en employant une analyse factorielle et les résultats ont été utilisés pour élaborer un modèle empirique permettant d'évaluer les performances du RCB en fonction de la longueur des cristaux, de la résolution TdV et de la taille de la lésion à l'aide d'une régression polynomiale à plusieurs variables. Comme prévu, les résultats ont montré que la performance RCB a des corrélations positives avec la taille de la lésion et la RTC, et une corrélation négative avec la longueur des cristaux. Cela conduit à un modèle prédictif qui estime la performance RCB avec une erreur quadratique moyenne de 0,69.

Abstract: One way to enhance lesion detectability in small animal positron emission tomography (PET) would be to improve the coincidence time resolution (CTR) significantly relative to the current state-of-the-art. This may soon become a real opportunity with the recent launch of the worldwide 10 ps challenge. Shorter crystals may be needed to improve timing performance by reducing the scintillation transit time spread. Although, this comes at the cost of sensitivity loss, the time-of-flight (TOF) gain may allow to compromise on sensitivity without degrading imaging performance. As the main advantage of TOF is to enhance contrast-to-noise ratio (CNR), there is a motivation to assess the trade-offs between crystal length and TOF resolution on the lesion detectability through a quantitative model. To derive such a model, a set of simulations was performed using the LabPET II mouse-version scanner with GATE and NEMA NU4 standards. The images were reconstructed using the CASToR software for tomographic reconstruction. The CNR was evaluated through a factorial design and its outcomes used to derive a model to assess the CNR performance as a function of crystal length, TOF resolution and lesion size using a polynomial regression with multiple variables. As expected, results showed that CNR performance has positive correlations with lesion size and gain in TOF resolution and a negative correlation with crystal length. This leads to a predictive model that estimates the CNR performance with a mean squared error of 0.69.

4.1 Introduction

Time of flight (TOF) positron emission tomography (PET) scanners are employing the difference between the arrival time of two opposite photons of the same annihilation to approximately locate the emission source in the system's field-of-view (FOV) [85]. Using time information allows for higher image contrast-to-noise ratio (CNR) and better lesion detectability by reducing the background noise, which in turn may alleviate the amount of radioactive tracer or scan time. [14, 18–22]. Availability of new scintillator materials along with advancements in photodetector technology gradually led to better timing performance, hence making TOF-PET scanners more in demand in recent years [171]. Currently commercial TOF-PET scanners reach coincidence time resolutions (CTRs) of 200-300 ps and report spatial resolution performance in the range of 3-4 mm [16, 156]. However, the achieved CTRs do not yet significantly enhance small lesion detectability, which is important in early cancer detection or small animal imaging. In our recent study, it was demonstrated that CTR in the 100 ps range could be effective for small lesion detection [50]. CTR values below 100 ps are currently achievable in the laboratory [113, 172] while a CTR down to ∼30 ps was demonstrated using an internally integrated Cherenkov radiators with micro-channel plate photodetectors [17].

The TOF gain in PET scanners is dependent on the object size and the improvement of CTR [85]. The benefit of improved CTR is considered so significant that it has given rise to the 10 ps worldwide challenge [90, 91]. If the CTR can be reduced down to 10 ps, every event can be placed at its exact location along the lines-of-response (LORs), hence avoiding the image reconstruction process and making real-time PET imaging possible.

A rigorous optimization of the light production and transport processes inside the scintillators is required to improve CTR. In addition, the use of faster photodetectors such as silicon photomultipliers (SiPMs) or single photon avalanche photodiodes (SPADs) are mandatory. To push the CTR limits, several approaches are being explored by researchers, including investigation of new crystal materials, exploitation of Cherenkov photon emission, and introduction of ultra-fast SPADs and front-end electronics [35, 97, 114, 117, 173, 174]. Recently, promising results were reported on a SPAD with 7.8 ps single photon time resolution [34]. This is a motivation to study the pros and cons of a shorter crystal length to reduce the transit time spread (TTS) and depth-of-interaction (DOI) induced time bias [95] as a solution for further CTR improvements. In addition, crystal length reduction would mitigate the radial elongation error hence improving image performance in the periphery of FOV. Nevertheless, the crystal length is a subject of controversy as it affects the image quality through several physical parameters [30, 106].

The three main factors of image quality that should be preserved for producing reliable PET images are spatial resolution, sensitivity and CNR. The spatial resolution has been investigated in the literature [23] and can be estimated by knowing crystal dimensions, decoding factor, acollinearity and positron range. The sensitivity has also been studied and can be estimated fairly accurately at the design stage of a scanner and is dependent on the number of coincidence events detected per time frame [175]. The latter is determined by the injected activity and the detection efficiency which relies on crystal material, dimensions and arrangement [119]. This emphasizes the importance of choosing appropriate crystal length at the design level as the choice of long and thick crystals leads to better sensitivity but deteriorates the radial spatial resolution and CTR, and as a result degrades the CNR performance [30, 86]. Longer crystals may also have a non-negligible impact on the overall cost of the detectors, although manufacturing of the finely pixelated crystal arrays represents a substantial fraction of the cost for small animal scanners. Our previous study showed that improved CTR can compensate for sensitivity loss due to crystal length reduction [50]. Nonetheless, amongst the physical parameters of image quality, CNR has rarely been investigated in the literature and the lack of a figure of merit or a model that can assess the CNR performance based on design parameters is evident.

To further enhance the image quality for the future generation of scanners, we aim to improve the CNR performance by using ultra-fast TOF technology. Hence, the CNR was studied as a function of three prime parameters including: crystal length, lesion size and CTR. For each of these parameters, a range of variations was investigated through a factorial design, followed by extraction of the correlation of these parameters with CNR. A model was then derived by supervised learning and validated using data from experiments and also simulations. The model can be used as a design tool for future generation of the scanner.

4.2 Materials & Methods

4.2.1 System Description

The mouse-version of the LabPET II scanner configuration was used as a model (Figure 4.1) [162]. The scanner relies on $1.125 \times 1.125 \times 10.6$ mm^3 $Lu_{1.9}Y_{0.1}SiO_5$: Ce (LYSO) scintillators. The crystals are arranged in 4×8 arrays and coupled one-to-one using clear optical epoxy to a pixelated monolithic APD array at a 1.2 mm pitch. Four of these arrays are then mounted on an interposer board to be interfaced to two 64-channel application-specific integrated circuits (ASIC). Forty eight of these modules are distributed on 4 rings of 78 mm diameter for a total of 6144 crystals. These ASICs were designed based on a dual-threshold time-over-threshold method that process and record the signal from every individual pixel detectors independently [176,177]. The scanner achieves a sub-millimeter spatial resolution of 0.8 mm at 1 mm from the center of the FOV and the axial sensitivity profile reaches 3% [163]. While LabPET II modular technology platform allows scanners to be designed with various sizes from small to mid sized animals (mouse to monkey) and up to the human brain [162, 163], the smallest scanner model was selected for this study in order to limit the computation time. Indeed, the study of each configuration is comprised of four steps, including simulation, reconstruction, image analysis and data post processing.

4.2.2 Simulation Configuration

The simulations were performed with the open-source Geant4 Application for Tomographic Emission (GATE) [164,178] package v.8.2. The NEMA NU4 2008 phantom [155] was used to assess the image quality. The phantom is a 50 mm long, 30 mm diameter cylinder made of polymethylmethacrylate which consists of three compartments as shown in Figure 4.2. The first compartment includes five fillable rods that have diameters of 1 to 5 mm (Figure 4.2-a) which will be used to assess the lesion detection capability. The central

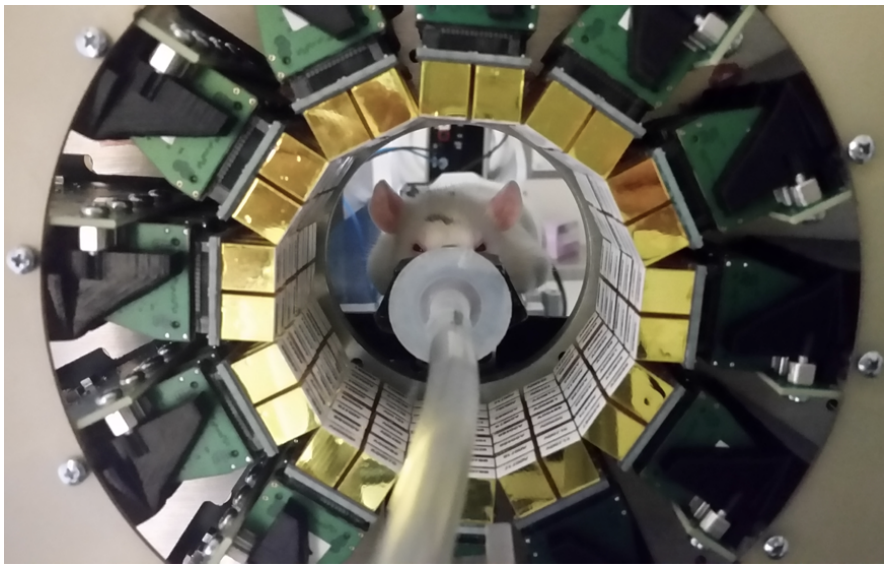

Figure 4.1 The mouse-version of the LabPET II scanner forming a 78 mm ring with an axial length of 50.4 mm.

part of the phantom is a uniform region used to quantify the uniformity by computing the percentage standard deviation (SD) on the mean (Figure 4.2-b). The third compartment consists of two vacant cylinders (Figure 4.2-c), one filled with air and the other filled with non-radioactive water, to calculate spill over ratios.

The phantom was simulated using a uniform concentration of 0.18 MBq/cc of ^{18}F for a total activity of 3.7 MBq and for a 20-minutes scan time. To calculate the CNR, a homogenous background activity was added to the first compartment of the phantom to provide a concentration ratio of 4:1 between the rods and background. The scanner parameters were set in accordance to manufacturer specifications, hence the energy window and the coincidence time window were set to [250-650] keV and 10 ns, respectively [162]. The energy resolution was set to 21% and the time resolution was set with the temporal resolution module from GATE which applies a Gaussian blurring in time domain.

To conduct the study, two sets of simulations were performed to investigate the impact of three parameters on CNR, namely CTR, crystal length and rod size. Table 4.1 summarizes the simulation parameters along with their associated levels. In the main set, for each parameter at least 5 levels of variations were considered for studying the CNR variation. In order to study the correlation of each variable and unveil the variation trends, a complementary set of simulations was performed to increase the statistical power with at least 10 samples. This gives a total of 480 trials for this factorial design study.

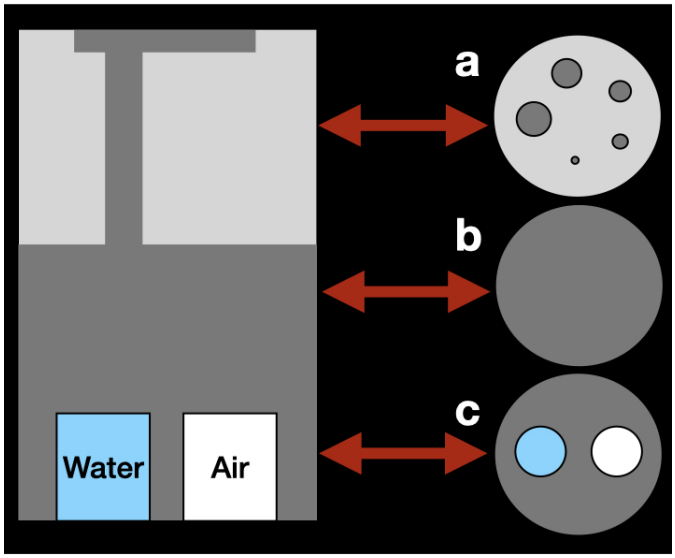

Figure 4.2 The modified NEMA NU4 2008 image quality phantom used in the simulations: a) The first compartment with five fillable rods in a uniform background with a 4:1 ratio; b) the second uniform compartment, and c) the third compartment with two cylindrical voids.

Table 4.1 Simulation parameters and their associated levels

Set	**Crystal length (mm)**	**CTR (ps)**	**Rod size (mm)**
Main set level of variations	6.6 7.1 7.6 8.1 8.6 9.1 9.6 10.1 10.6 11.6 20	10 20 30 40 50 100	1 2 3 4 5
Complementary set level of variations	6.6 8.6 10.6	14 28 42 56 70	1.2 2.4 3.2 3.8 4.6

For the main set, the 10.6 mm was made to comply with the current configuration of the LabPET II mouse scanner. The shortest crystal length (e.g., 6.6 mm) was selected as a limit where the inconsistencies in CNR performance was observed in the simulations. The other lengths were chosen at a 0.5 mm step, while the choice of the longest crystal length of 20 mm was chosen as the upper limit with which less than 100 ps CTR was achieved in the literature [117]. The 10 ps CTR value was selected to be consistent with the 10

ps worldwide challenge [91]. The higher values for CTR were chosen to be in accordance with the phantom rod sizes. The highest value of CTR (e.g., 100 ps) is chosen as a limit where the CTR leads to an insignificant gain in small animal imaging [50] and also the recently achieved reported CTR with long crystals.

For the complementary set, the choice of rod sizes was made so that the total activity in the phantom does not exceed the instructed activity by NEMA standard, which is 3.7 MBq. The choice of CTR was made to add 5 observations to the main set where each level of CTR in the complementary set is $\sqrt{2} \propto 1.4$ times CTRs of the main set.

4.2.3 Reconstruction Parameters

Images were reconstructed using ROOT output data from GATE with a voxel size of $0.3 \times 0.3 \times 1\,\mathrm{mm}^3$ with voxelization of $160 \times 160 \times 60$. The 3D MLEM algorithm Customizable and Advanced Software for Tomographic Reconstruction (CASToR) [165] was used with multiple ray-tracing of the Siddon projector [166] so that the solid angle contribution of each event is considered in the system matrix.

4.2.4 Image Analysis

The CNR was assessed using an in-house Matlab code developed to place ROIs over the rods with the same diameters and 6 ROIs on the background each with 6 mm diameter as shown in Figure 4.3. CNR evaluation was performed by

$$\mathrm{CNR_L} = \frac{\mathrm{Mean_L} - \mathrm{Mean_{Bg}}}{\sigma_{\mathrm{Bg}}}, \tag{4.1}$$

where $\mathrm{Mean_L}$ represents the mean of each rod, while $\mathrm{Mean_{Bg}}$ and σ_{Bg} represent the overall mean and standard deviation of the six background regions in the first compartment of the phantom, respectively. The images were analyzed at 5 iterations relying on fast convergence of TOF reconstructions.

4.2.5 Model Derivation

To obtain the CNR model, two steps were undertaken; first the correlation of each parameter was studied with the CNR, then the correlations and the main data set were used in a regression analysis to obtain a predictive model for CNR. All analyses for model derivation were conducted in Matlab.

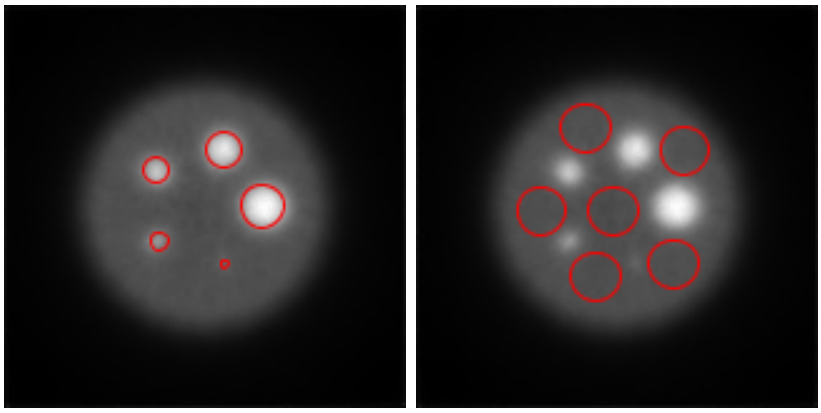

Figure 4.3 Example of a reconstructed image for CNR analysis obtained with crystal length of 10.6 mm and CTR of 30 ps, Left: ROI for obtaining mean values, Right: ROIs for measuring the background.

– **Study of Correlations:** To study the correlation of each parameter with respect to CNR, the datasets in Table 4.1 was used whenever required. The CNR variation was investigated for at least ten observations for each parameter while keeping the other two parameters constant.

A curve fitting tool was used to estimate the correlations. The curve leading to the highest coefficient of determination or R squared (R^2) and matching with the *a priori* knowledge of physics was selected. Hence, the degree of association of each parameter with CNR was chosen to satisfy both the physics and highest achievable R^2. In addition, as the number of observations for a given set of parameters may vary from one to another, the adjusted R^2 was calculated for each parameter that allows measuring the correlation, thus provides the information on the most significant parameter in the model.

– **Predictive Model:** Polynomial regression was used to extract the model that predicts the value of a variable based on one or multiple parameters (predictors) and is expressed by

$$Y = \theta_0 + \theta_1 X_1 + ... + \theta_2 X_1^2 + ... + \theta_d X_1^d + ...\theta_{d+n-1} X_n, \tag{4.2}$$

where Y is polynomially related to X_n's with the polynomial degree d. The matrix of coefficients Θ and the matrix of parameters X are expressed by

$$\Theta = \begin{bmatrix} \theta_0 \\ \theta_1 \\ \vdots \\ \theta_{d+n-1} \end{bmatrix}, X = \begin{bmatrix} X_1 ... X_n \\ \vdots \\ X_m ... X_{mn} \end{bmatrix}, \tag{4.3}$$

where in this study, the X matrix holds for parameters such as crystal length, CTR and lesion size for m observations, Y is the dependent variable, in our case the CNR, and Θ is the matrix of coefficients of the regression model that was calculated by

$$Y = X\Theta \rightarrow \Theta = (X^T X)^{-1} X^T y, \tag{4.4}$$

The error of the regression analysis was measured by the mean square error (MSE) calculated by

$$MSE(\theta_0, \theta_1, \theta_2, ..., \theta_n) = \frac{1}{m} \sum_{i=1}^{m} (y_i - Y_i)^2, \tag{4.5}$$

where m is the total number of observations, Y_i is the matrix of predicted values obtained from the regression model and y_i is the matrix of measured data obtained from GATE simulations. The MSE is considered to be significant when it affects the CNR detection limit, which is 5 according to Rose criterion [179]. This means that whenever the obtained MSE is larger than the difference of the obtained CNR and 5, it is considered to be significant as it affects the outcome of the lesion detectability by changing the status of the lesion from detectable to non-detectable and vice versa.
In order to smooth the drastic change of the level of variations for the parameters in the model, the location uncertainty (Δx) associated with each CTR was used to derive the CNR model and was calculated by

$$\Delta x = \frac{CTR \times c}{2}, \tag{4.6}$$

where c is the speed of light. This was followed by mapping the obtained correlation into the X matrix. Then, the data of the main set in Table 4.1 for crystal length of 6.6 to 10.6 mm was used as a training set to calculate the coefficients. However, the data set corresponding to the crystal length of 10.1 mm was excluded and reserved for the purpose of validation. Hence, the data of the complementary set in Table 4.1 along with the data set corresponding to crystal length of 10.1 mm were used as a test set. The MSE was also measured to assess the quality of the CNR predictive model for both training and test sets.

4.2.6 Model validation

The validation was done in two steps through simulations and experiments.

– **Simulation Validation:** The test set was used to validate the model. The predicted values were obtained by placing the test data into the model. The associated MSE was measured and reported thereafter.

– **Experimental Validation:** An experimental study was performed on NEMA NU4 2008 phantom using the LabPET II mouse scanner with an initial activity of 5.6 MBq for a 10-minutes scan. The in-house reconstruction code was used with 3D-MLEM algorithm relying on an analytical system matrix that models the photon interaction probabilities within the detector arrays with $0.3 \times 0.3 \times 0.3$ mm^3 voxelization. The images were corrected for only random contributions. The image analysis was performed on the 10 mm central region of the first compartment as instructed by NEMA NU4 2008 and the images were analyzed at 5 iterations. Figure 4.4 shows the image along with the ROIs. The choice of 5 iteration was made in accordance with the iteration used for performing image analysis for the simulations. For the purpose of comparison with the CNR values obtained from

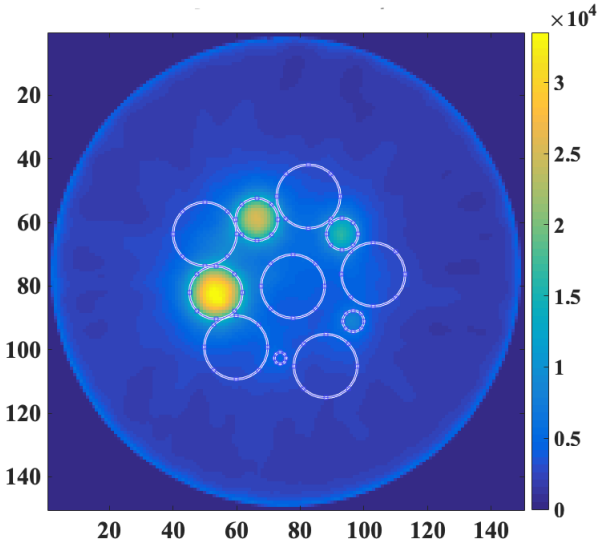

Figure 4.4 Image obtained by the LabPET II mouse scanner and the ROIs for CNR analysis at 5 iterations.

the experiment, the CNR model was used to estimate the CNR performance for crystal length of 10.6 mm, CTR of 100 ps and all rod sizes. The choice of 10.6 mm crystal length was made to comply with the current configuration of the LabPET II mouse scanner. The CTR of 100 ps is a suitable choice for a fair comparison as the scanner is not TOF capable and this CTR does not lead to a significant gain. The MSE was measured to investigate the accuracy of the predicted values by the CNR model.

4.3 Results

The results are presented in three parts: correlations, derived predictive CNR model and finally validation of the CNR model. For the analysis, the results corresponding to the 1 mm diameter rod were excluded as they mainly led to CNR values below 3.

4.3.1 Correlations

The correlation of crystal length, rod size and CTR along with their corresponding adjusted R^2 are reported as follows.

– **Correlation of CNR with Crystal Length:** The effect of crystal length on CNR is shown in Figure 4.5 for a CTR of 10 ps and rod sizes of 2, 3, 4 and 5 mm, obtained from 11 observations. The data of the 3 mm rod were fitted with a quadratic polynomial. It is observed that CNR has a negative correlation with crystal length, meaning that increasing crystal length leads to CNR degradation. This is because image reconstruction relies highly on counting statistics and is more efficient with ultra-fast TOF [180]. This implies that the reconstruction algorithm tends to converge faster to maximum CNR values when the counting statistics are adequate and as the CTR is improved. In addition, as the 3D reconstruction algorithm was used the radial elongation error is reduced by using shorter crystals. A discontinuity in CNR performance is observed between crystal lengths of 7.6 and 8.1 mm for all rods. This can be attributed to the alignment of the rods (all at the same distance from the centre) with the gaps between detector blocks at this crystal length. An adjusted R^2 of 0.97 is obtained by fitting the second degree polynomial curve. This result is in agreement with the literature [23, 119] and the same degree polynomial is assigned to this correlation.

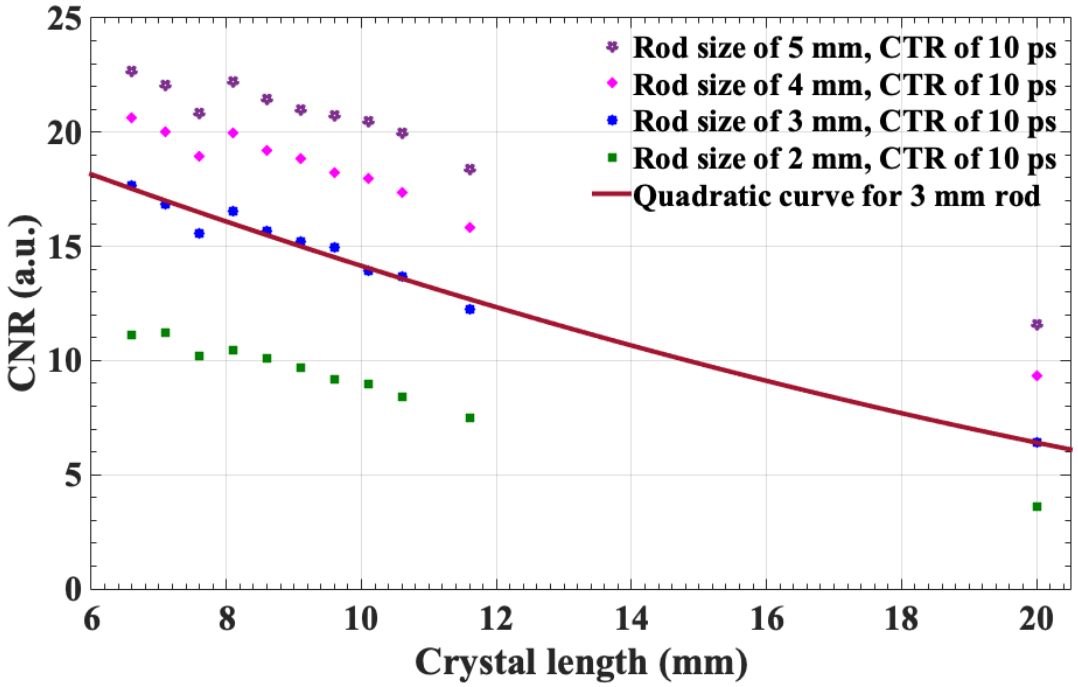

Figure 4.5 Correlation of CNR with crystal length for CTR of 10 ps obtained from 11 observations at 5 iterations.

– **Correlation of CNR with Rod Size:** The effect of rod size on CNR is shown in Figure 4.6 for CTR values of 10, 20, 30 and 40 ps and a crystal length of 10.6 mm. It is observed that rod size has a positive correlation with CNR. This is because the smaller lesions (rod sizes) are affected by partial volume effect, which dampens their intensity in the image. Thus the bigger the lesion size (rod size) the better the lesion detectability. The adjusted R^2 is equal to 0.99 for the second degree fitted curve, which is assigned to this parameter in the model.

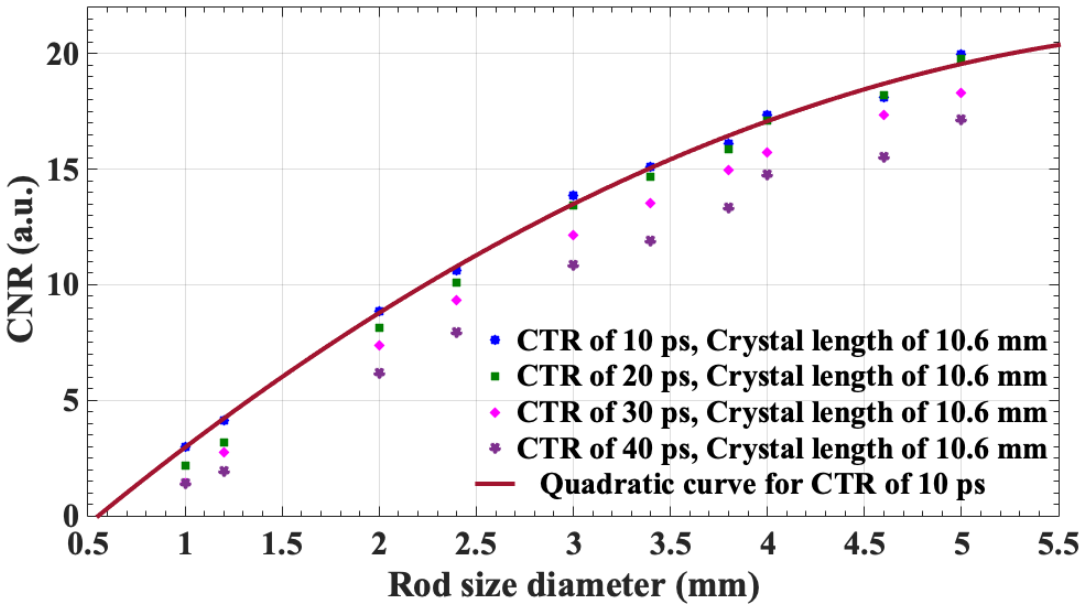

Figure 4.6 Correlation of CNR with rod size for a crystal length of 10.6 mm obtained from 10 observations.

– **Correlation of CNR with CTR:** Figure 4.7 shows the CNR performance with respect to CTR variations for a crystal length of 10.6 mm and rod sizes of 2, 3, 4 and 5 mm. As expected, improved CTR results in the reduction of background noise and thus an improvement of the CNR performance [171]. Hence, CNR has a negative correlation with the increasement of CTR values which translates into a positive correlation with improved CTRs. An adjusted R^2 of 0.97 was obtained for the fitted curve of the 3 mm rod data.

On the basis of *a priori* knowledge of physics and the observed correlation of the crystal length, rod size and CTR, a figure of merit can be derived for CNR performance as follows

$$CNR \propto \frac{\sqrt{Rod\ size}}{Crystal\ length \times \sqrt{CTR}}, \tag{4.7}$$

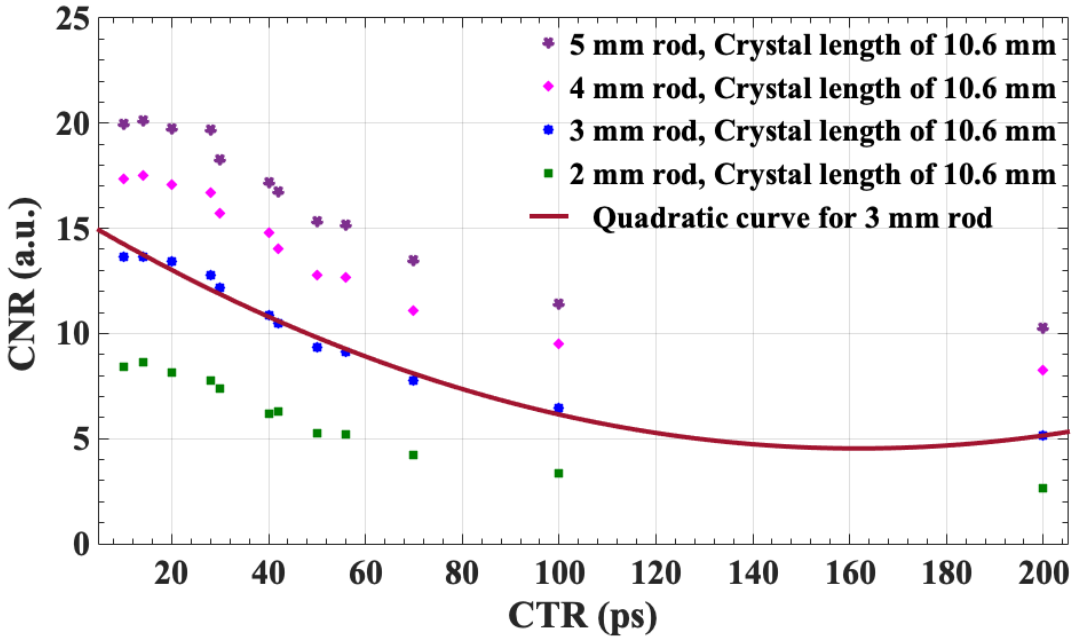

Figure 4.7 Correlation of CNR with CTR for a crystal length of 10.6 mm obtained from 12 observations.

Although the CNR correlation in Equation 4.7 is not unit less, it should be noted that the scan time contributes positively to CNR performance. However, as all the data sets were obtained with the same scan time, the effect of this parameter was not investigated in this work.

4.3.2 Derived Predictive CNR Model

On the basis of observed correlations (Equation 4.7), the X matrix is formed as

$$X = [1, Rod\ size, \sqrt{Rod\ size}, \Delta x, \frac{1}{\sqrt{\Delta x}}, Length, \frac{1}{Length}], \tag{4.8}$$

where Δx's are associated with CTRs by Equation 4.6. By introducing the CNR values obtained by simulations of the main dataset (Table 4.1) in the Y matrix and performing the regression analysis using Equation 4.4, the coefficients (Θ's) can be extracted. The predictive model is determined as

$$\begin{aligned} CNR = &-18.25 - 4.36 \times Rod\ size + 29.01 \times \sqrt{Rod\ size} \\ &- 0.51 \times \Delta x + 3.44 \times \frac{1}{\sqrt{\Delta x}} - 0.53 \times Length \\ &- 5.2 \times \frac{1}{Length}, \end{aligned} \tag{4.9}$$

The MSE for the regression model is 0.68 for a measured CNR variation range of 19.5 (from 4 to 23.5).

4.3.3 Validating the CNR Model

– **Simulation Validation:** The model was verified using the complementary dataset (Table 4.1) and also the data set corresponding to the 10.1 mm crystal length of the main set. The overall MSE for the test dataset is found to be 0.69.

Figure 4.8 shows the CNR's obtained using the CNR model as well as those measured from the simulations for crystal length of 10.1 mm, CTRs of 10, 20, 30, 40, 50 and 100 ps and rod sizes of 2, 3, 4 and 5 mm. The CNR values predicted by the CNR model are in reasonable agreement with the CNR measured values from the simulations. The MSE is notable for detecting the 2 mm rod with CTRs of 50 ps as the MSE of 0.69 is larger than the difference of the obtained CNR for this combination (e.g., 5.6) and Rose detection limit (e.g., 5).

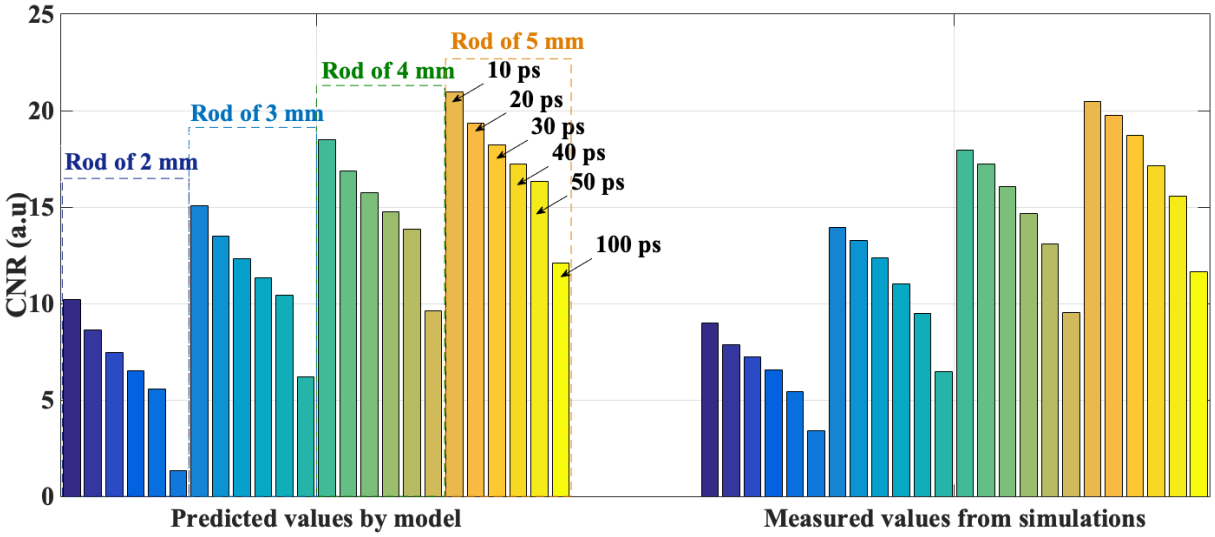

Figure 4.8 Validation of the CNR model with crystal length of 10.1 mm for rod sizes of 2, 3, 4, and 5 mm and CTR of 10 to 100 ps. The mean difference between the predicted values by the model and the measured values from the simulation is 4%.

Figure 4.9 depicts the comparison of CNR values obtained by the model and simulations for a crystal length of 6.6 mm and CTRs of 14, 28, 42, 56 and 70 ps. The reported error is of importance for detection of 2 mm rod with CTRs of 56 and 70 ps.

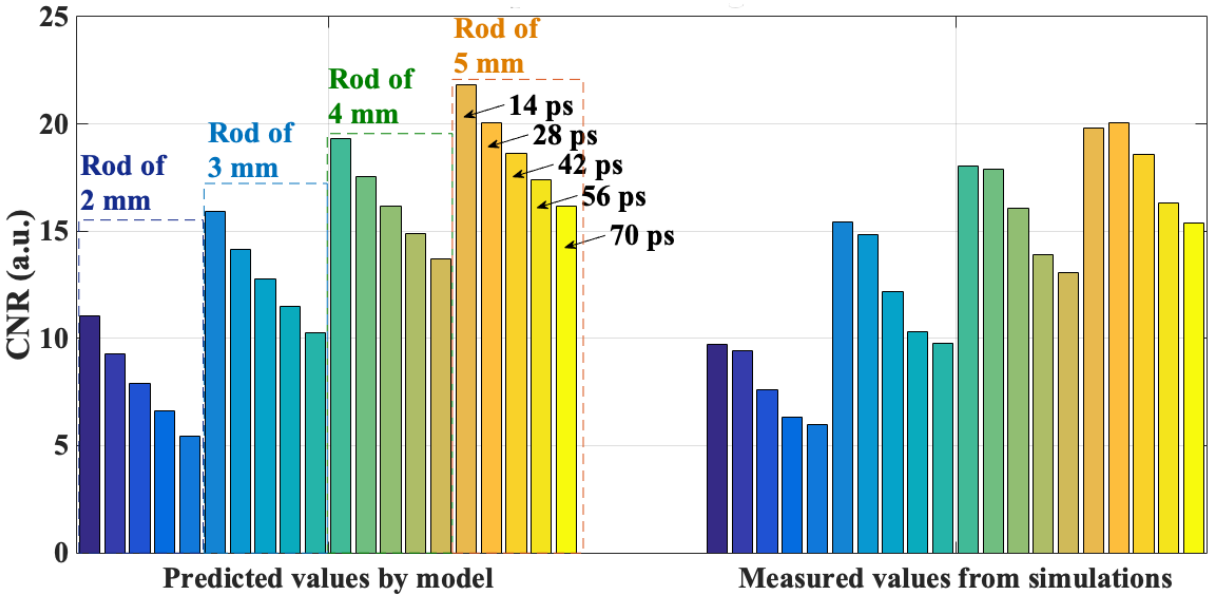

Figure 4.9 Validation of the CNR model with crystal length of 6.6 mm for rod sizes of 2, 3, 4 and 5 mm and CTRs of 14 to 70 ps. The mean difference between the predicted values by the model and the measured values from the simulation is 4.7%.

The results of the model validation for a crystal length of 10.1 mm is also reported in Figure 4.10. The MSE is remarkable for the CNR values obtained for rod size of 2 mm with CTRs of 56 and 70 ps.

– **Experimental Validation:** Figure 4.11 compares the predicted values by the CNR model and the experimental data. It is observed that at 5 iterations the predicted values are in a good agreement with the experimental data for all rods, with the MSE calculated to be 0.43 for this comparison.

4.4 Discussion

In this work, possible further improvement of image quality with fast TOF was investigated for a highly pixelated scanner that already achieved an optimum spatial resolution (0.8 mm at 1 mm from the center in the scanner's FOV). To fulfill this, a series of simulations was performed with GATE using the NEMA NU4 2008 phantom to quantify CNR performance based on the three most important parameters, which are crystal length, lesion (rod) size and CTR. This was followed by studying the correlation of these parameters with CNR to derive a predictive model of CNR by the regression analysis. The CNR model was validated using the data from simulations and experiments.

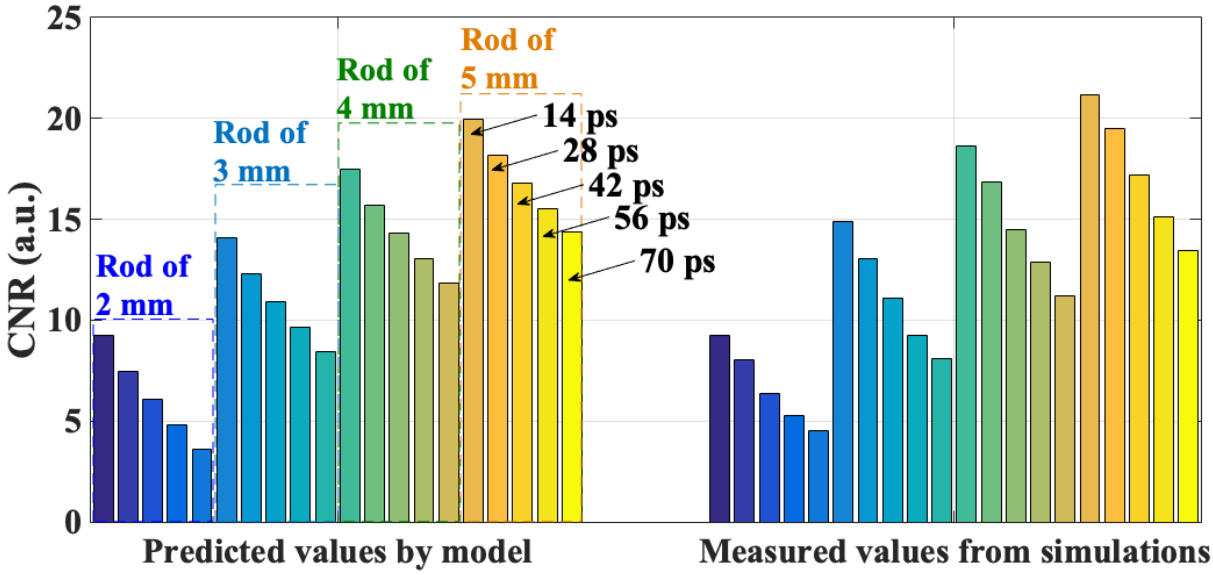

Figure 4.10 Validation of the CNR model with crystal length of 10.1 mm for rod sizes of 2, 3, 4, and 5 mm and CTR of 14 to 70 ps. The mean difference between the predicted values by the model and the measured values from the simulation is 3.1%.

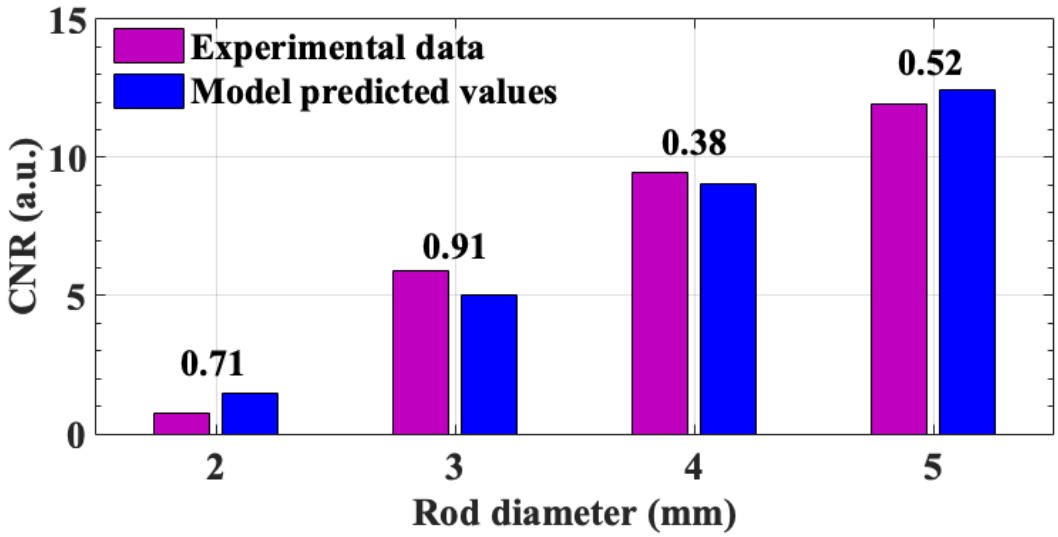

Figure 4.11 Comparison of the CNR predicted by the model and measured from the experiment at 5 iterations. This is for a crystal length of 10.6 mm and a simulated CTR of 100 ps and the number above each rod signifies the absolute value of the difference between the experimental data and the model predicted values.

As expected, results showed that the lesion size and improved CTR have positive correlations with CNR, while the crystal length has a negative correlations with the latter. These results are in general agreement with physics and the literature. Moreover, the most significant predictor in the model was found to be the rod size. However, the crystal length and CTR contribute rather equally as predictors in the CNR model. Hence, the crystal length can indeed be traded off with CTR without loss of CNR and this should facilitate the achievement of faster TOF and expedite the 10 ps TOF challenge.

It was also demonstrated that CNR performance can be estimated with a reasonable accuracy as an overall MSE of 0.68 and 0.69 was obtained for the training set and test set, respectively. The error is not significant for the rod size of 3 mm or larger, but can increase substantially for the 2 mm rod as the CNR values drop in the range between 3 to 12, close to the margin of 5 considered by the Rose criterion for lesion detection. It is worth noting that the CNR of the 2 mm lesion could be raised above the detection criterion with ultra-fast CTR under 50 ps. In addition, the validation of the CNR model against both simulation and experimental data confirms the robustness of the proposed approach to predict the CNR values for CTR of 10 to 100 ps.

Moreover, as different counting statistics were used in this study, the choice of the iteration number for image analysis was a challenge. Although for this research all the data were analyzed at the same iteration number, slightly different trends could be observed if other iteration numbers would have been investigated. Hence, the iteration number could be included as a parameter in the model to have a more accurate predictive model for CNR. However, this would require a more complex model that will be presented in future work.

Although the target is set to achieve the 100 ps time resolution in near future, studies have shown that there should be no physical or technological limits in achieving time resolutions below 100 ps, as illustrated by the 10 ps worldwide challenge [91]. Yet for the purpose of this study, we focused our effort on the development of the method to extract a model for CNR analysis. In order to reduce the computational cost, we used a small scanner geometry for studying ultra-fast TOF. Nonetheless, this was a time consuming process as for each trial in this study, a GATE simulation with a 20-minutes scan time, followed by the image reconstruction and then the image analysis and post processing was conducted. However, this approach can be extended to larger scanners for studying more realistic CTRs.

Finally, the CNR image performance is parametrized and presented in a form of a polynomial predictive model. The model was validated with both simulation and experimental

data, however the fact that small animal scanners manufactured so far are not TOF capable is a limitation for further experimental validation. Nonetheless, the approach developed in this work can be readily extended to larger systems such as the UHR brain scanner [163] or clinical TOF whole body 3D scanners [16, 156], allowing more extensive quantitative performance analysis to be carried out.

4.5 Conclusion

We have used a novel approach to derive a model allowing to assess the CNR performance for the LabPET II small animal scanner with ultra-fast TOF based on three parameters. The model was validated and a MSE of 0.69 was obtained, confirming the accuracy of the model. This model can be useful as a tool to evaluate the CNR performance prior to the design and manufacturing of the next generation of TOF capable scanners. The proposed model can be easily adapted to other scanner configurations and be extended to include the impact of other parameters on CNR performance, such as iteration number, phantom size and location of the lesion in the field of view.

Acknowledgment

The authors would like to thank the Natural Sciences and Engineering Research Council of Canada (NSERC) and Mitacs for their financial support and also Calcul Quebec and Compute Canada for their technical support and assistance with this research. In addition, we would like to thank Dr. Jean-Baptise Michaud for his help in offering resources on his Calcul Quebec and Compute Canada accounts.

CHAPTER 5

RESULTS: Novel Phantom for Practical Performance Evaluation of TOF-PET Scanners

Authors and affiliations:

- Nikta Zarif Yussefian : PhD student, Department of Electrical and Computer Engineering, Engineering Faculty, Université de Sherbrooke
- Émilie Gaudin : Post doctoral fellow, Department of Nuclear Medicine and Radiobiology, Faculty of Medicine and Health Sciences, Université de Sherbrooke
- Roger Lecomte : Professor, Department of Nuclear Medicine and Radiobiology, Faculty of Medicine and Health Sciences, Université de Sherbrooke
- Réjean Fontaine : Professor, Department of Electrical and Computer Engineering, Engineering Faculty, Université de Sherbrooke

Submission date: October 05, 2021

Journal: Physics in Medicine and Biology.

Reference: [52]

Contribution of the article: This is the last article of a series of three. The first article covered the trade-offs between the main parameters contributing to CNR performance. This was followed by the second article where a model was derived for predicting CNR performance of a scanner at the design stage. In order to extend the CNR model to the UHR brain scanner based on the LabPET II technology, this work is focused on developing a phantom allowing to conduct extensive TOF assessment on clinical scanners.

Although the TOF technology has made considerable progress in the recent years, there is no gold standard developed to study the impact of TOF resolution on scanner performance at the design stage. Hence, this article proposes a novel phantom that allows assessing the

influence of the TOF resolution on image performance all over the field-of-view. To the authors' knowledge, this design is novel and there has not been any published document dealing specifically with this subject.

French title: Une nouvelle mire pour l'évaluation pratique des performances des scanners TEP-TdV

Résumé: Les progrès récents dans le développement de photocapteurs et de matériaux de scintillation contribuent de manière significative à l'avancement de la technologie du temps de vol (TdV) pour la tomographie d'émission par positrons (TEP) et ont conduit à l'émergence de scanners TEP TdV atteignant une résolution de temps de coïncidence inférieure à 300 ps. Les scanners TEP TdV offrent des avantages en termes de réduction du temps d'acquisition ou de la dose injectée et une meilleure détectabilité des petites lésions. En règle générale, les mires NEMA sont des normes globale à utiliser pour l'évaluation des performances des scanners. Cependant, ces mires ne sont pas entièrement appropriées pour évaluer les performances TdV, en particulier au niveau de la conception des scanners, car la taille des structures est généralement plus grande que la résolution TdV actuellement atteinte. Compte tenu du développement rapide de la technologie TdV au cours des dernières années, nous proposons une nouvelle mire conçue pour évaluer la précision de la résolution TdV dans l'ensemble du champ de vue des scanners atteignant l'état de l'art actuel jusqu'à l'objectif ultime d'un TdV de 10 ps. Les caractéristiques de la mire pour évaluer les performances du TdV ont été étudiées en effectuant des simulations à l'aide des outils Geant4 Application for Tomographic Emission (GATE) et Customizable and Advanced Software for Tomographic Reconstruction (CASToR). Les simulations ont été validées en effectuant des mesures expérimentales avec un scanner TEP/TDM Siemens Biograph Vision.

Abstract: Recent progress in photosensors and scintillator materials has contributed significantly to the development of fast radiation detectors and has led to the emergence of time-of-flight positron emission tomography (TOF-PET) scanners. TOF-PET provides many benefits that can be summarized as the reduction of scan time or injected dose and enhanced small lesion detectability. Generally, NEMA phantoms are gold standards for the performance evaluation of PET scanners. However, these phantoms are not fully appropriate to assess TOF-PET performance, in particular at the design stage of the future generation of TOF-PET scanners that are expected to achieve much better TOF resolution. Considering the fast development of TOF technology in recent years, we propose a novel phantom designed for assessing TOF resolution accuracy across the entire field of view of scanners achieving state-of-the-art performance down to the ultimate goal of 10 ps TOF. The phantom characteristics for assessing the performance of TOF-PET were investigated by conducting simulations using Geant4 Application for Tomographic Emission (GATE) and the Customizable and Advanced Software for Tomographic Reconstruction (CASToR). The simulations were validated by conducting experiments with the Siemens Biograph Vision PET/CT scanner.

5.1 Introduction

Time-of-flight (TOF) positron emission tomography (PET) provides better localization of the annihilation process by measuring the arrival time difference of the two annihilation photons [85]. TOF PET was introduced a few decades ago using CsF- and BaF2-based scintillators along with photomultiplier tubes (PMTs) able to achieve a TOF resolution of 400 - 700 ps [181]. However, the rather poor detection efficiency, the poor spatial resolution resulting from the use of larger detectors and the modest TOF resolution achieved with those detectors were insufficient to gain any benefit in imaging applications, making TOF uncompetitive at the time. The emergence of dense and high-luminosity Lutetium-based scintillators providing high and fast light output along with the progress in photosensor technology has led to better time performance [14, 15, 119]. This triggered the development of TOF-PET scanners with much improved image contrast-to-noise ratios (CNRs) performance, thus allowing the reduction of scan time or of the administered dose [14, 18, 20]. As better TOF resolution also provides a better control of data inconsistencies [14, 18–22, 85, 182], there is a motivation to push the limits of TOF to even avoid tomographic image reconstruction, as claimed by the 10 ps challenge [90, 91]. While the best reported coincidence time resolution (CTR) acquired so far is 215 ps in commercial clinical scanners [16,156], researchers have shown that a 100 ps CTR is within reach in the near future [114,174]. Nonetheless, to better detect small lesions such as lymph nodes and

early breast and prostate cancers, CTR down to 100 ps would be highly desirable. Moreover, sub-100 ps CTR is required for TOF to be useful in preclinical studies [50]. Hence, several groups are engaged on pushing the limits of TOF by optimizing performance at each step of the data acquisition process [11, 17, 35, 114, 183, 184]. Currently, the world record for best CTR performance in the laboratory is 30 ps using microchannel plate photomultiplier tubes (MCP-PMTs) integrated with 3.2-mm thick Cherenkov radiators [17].

NEMA standards are generally employed to evaluate the performance of PET scanners [185]. However, the NEMA phantom geometry is not completely appropriate for current and future TOF-PET technology to be evaluated fully as it does not allow to probe the performance all across the FOV. Although a method is proposed to measure TOF-PET capabilities using the NEMA noise equivalent count (NEC) phantom [186], this method is experimental and can be used for only TOF capable scanners. With the rapid progression of TOF technology, there is a need for a model or a gold standard for rigorously and systematically evaluating CNR performance. Thus, we propose a novel phantom allowing the assessment of the performance of TOF-PET scanners at the design stage and all across the field of view (FOV). In order to confirm the robustness of the simulation process, first an experimental study was conducted with the Jaszczak phantom [187] and the Siemens Biograph Vision PET/CT scanner that reported TOF resolution of 215 ps [16] and the results of the experiment was compared to the simulation study conducted with same characteristics using the proposed phantom. Then, to investigated the TOF gain, the proposed phantom was used to assess CNR performance of UHR brain dedicated PET scanner based on the LabPET II detection platform that is presumably TOF capable [49, 162, 163]. This is followed by conducting a comparative simulation study on the imaging performance of the UHR and the Siemens Biograph Vision scanner [16] with and without TOF capabilities.

5.2 Materials & Methods

5.2.1 Phantom Design and Specifications

An in-house phantom (Figure 5.1) was designed for the purpose of assessing the benefit of TOF on the CNR for clinical TOF-PET scanners. The phantom is a 90 mm long, 240 mm diameter cylinder consisting of 20 rods spread spirally across the field of view (FOV). The spiral configuration is chosen to avoid the overlap of larger rods, in particular if the small version of the phantom needs to be adapted in future to fit within small animal scanners FOV. The rod sizes were chosen with diameters from 15 mm down to 1.5 mm to be in accordance to TOF resolution from 100 ps down to 10 ps [90, 91]. Table 5.1 lists the

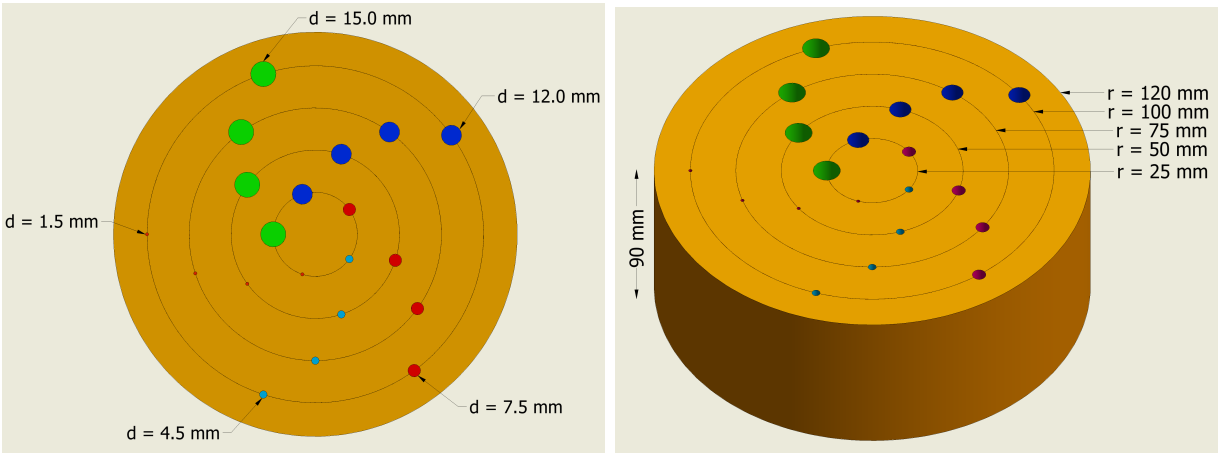

Figure 5.1 TOF Phantom model, a cylinder with a radius of 120 mm and length of 90 mm containing 20 rods that spread spirally all over FOV. Left: TOF phantom rod dimension, Right: TOF phantom rod arrangement.

rod arrangement and their specifications. In addition, Figure 5.1-Left and Right show the phantom rod dimensions and arrangements, respectively. The phantom can be employed either with hot rods and cold background or cold rods and hot background. Both features were employed in this study such that the hot rods feature is used more often, except for the purpose of experimental validation where the phantom is used with cold rods.

Table 5.1 Specifications of the TOF phantom. Each object (rod) is placed at distance r from the center in mm and an angle of θ in degree

	Object Diameter (mm)	Associated TOF Resolution (ps)	Object Position (r,θ)			
			First Replica	Second Replica	Third Replica	Fourth Replica
1	15.0	100	(25 mm, 0°)	(50 mm, 324°)	(75 mm, 306°)	(100 mm, 288°)
2	12.0	80	(25 mm, 288°)	(50 mm, 252°)	(75 mm, 234°)	(100 mm, 216°)
3	7.5	50	(25 mm, 216°)	(50 mm, 180°)	(75 mm, 162°)	(100 mm, 144°)
4	4.5	30	(25 mm, 144°)	(50 mm, 108°)	(75 mm, 90°)	(100 mm, 72°)
5	1.5	10	(25 mm, 72°)	(50 mm, 36°)	(75 mm, 18°)	(100 mm, 0°)

5.2.2 Systems Description

The GATE model of ultra high resolution (UHR) brain PET scanner was used in this study consisting of 4 × 8 array of 1.12 × 1.12 × 12 mm^3 $Lu_{1.9}Y_{0.1}SiO_5$: Ce (LYSO) scintillators. To optimize the spatial resolution, the scintillators are coupled one-to-one with a 1.2 mm pitch to a 4 × 8 monolithic APD arrays [163] for a total of 129,024 crystals spread over a cylinder with a diameter of 390 mm and an axial length of 235 mm. Figure 5.2-Left shows the simulation model of the UHR scanner.

The simulated performance of the UHR brain scanner was previously compared to the recent SiPM-based Biograph Vision TOF PET/CT scanner developed by Siemens Medical Solution Inc. according to NEMA standards [16,163]. The Siemens Biograph Vision relies on arrays of 3.2 × 3.2 × 20 mm^3 LSO scintillators optically coupled to 4 × 4 channel SiPM arrays. The overall 60,800 crystal elements form a cylinder with a diameter of 820 mm and an axial length of 263 mm (Figure 5.2-Right). The detailed specifications of the scanners are listed in Table 5.2.

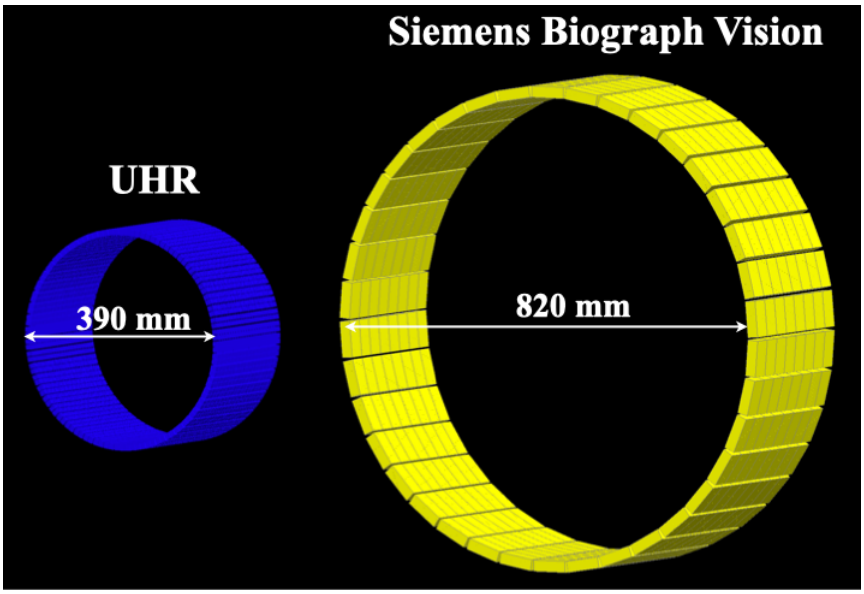

Figure 5.2 GATE models of the scanners used in this study. Left: UHR scanner from LabPET II series with ring diameter of 390 mm, Right: Siemens Biograph Vision scanner with the ring diameter of 820 mm.

Table 5.2 Simulation characteristics of the UHR and Siemens Biograph Vision scanners.

Characteristics	UHR	Siemens Biograph Vision
Energy resolution (FWHM)	21%	10.5%
Energy window (keV)	250 - 650	435 - 650
CTR (ps)	215	215
Coincidence time window (ns)	6	4.73
Scintillator material	LYSO	LSO
Scintillator dimension (mm^3)	1.12 × 1.12 × 12	3.2 × 3.2 × 20
Scintillator array dimension	4 × 8	10 × 20
Number of scintillators	129,024	60,800
Transaxial FOV (mm)	271	700
Axial length (mm)	235	263

5.2.3 Experimental Study

For the purpose of validating the simulation with the experiment the Flangeless Deluxe Jaszczak phantom was used [187]. The Jaszczak phantom is composed of three compartments. The first compartment contains 6 sections of cold rods with diameters of 4.8, 6.4, 7.9, 9.5 11.1, and 12.7 mm, the second compartment consists of 5 cold spheres with diameters of 9.5, 12.7 15.9, 19.1, 25.4 and 31.8 mm and finally the third compartment is a uniform distribution. The first and third compartments of the phantom were used for the purpose of validating simulations as the first part contains a section filled with rods of 7.9 mm diameter which is comparable to the rod of 7.5 mm diameter in that of the TOF phantom. The phantom was filled with the activity of 0.0212 MBq/cc of ^{18}F and placed in the center of the Siemens Biograph Vision scanner. Acquisition times of 3, 5, and 7 minutes were used.

To assess the validity of the simulation process and also conduct a fair comparison with the Jaszczak phantom, the TOF phantom was filled with the same activity concentration as the Jaszczak phantom and was employed with hot background and cold rods. The simulations were conducted with the Siemens Biograph Vision PET/CT scanner with the same acquisition time as the experiments.

– **Reconstruction Parameters:** Image reconstruction was performed with the Siemens 3D OSEM TOF software with 5 subsets and 0.825 × 0.825 × 3 mm^3 voxel size for 3, 5, and 7 minutes acquisition times. The images were corrected for attenuation using CT data and analyzed at 5 and 8 iterations. The number of iterations was selected according to the previously published study performed by the manufacturer [16]. For the purpose of validation, the simulation data were reconstructed using CASToR with the exact same parameters and iteration numbers as the experiment.

– **Image Analysis:** Image analysis was done according to the standard method developed for the phantom with hot background [188] as

$$CNR_L = \frac{Mean_{Bg} - Min_L}{\sigma_{Bg}},$$

where CNR_L is the CNR of each rod with the diameter of L, Min_L represents the minimum value of each rod with diameter L, while $Mean_{Bg}$ and σ_{Bg} represent the overall mean and standard deviation of the hot background region in the uniform region of the phantom, respectively. The ROI is placed over all three replicas of 7.9 mm rods on Jaszczak phantom

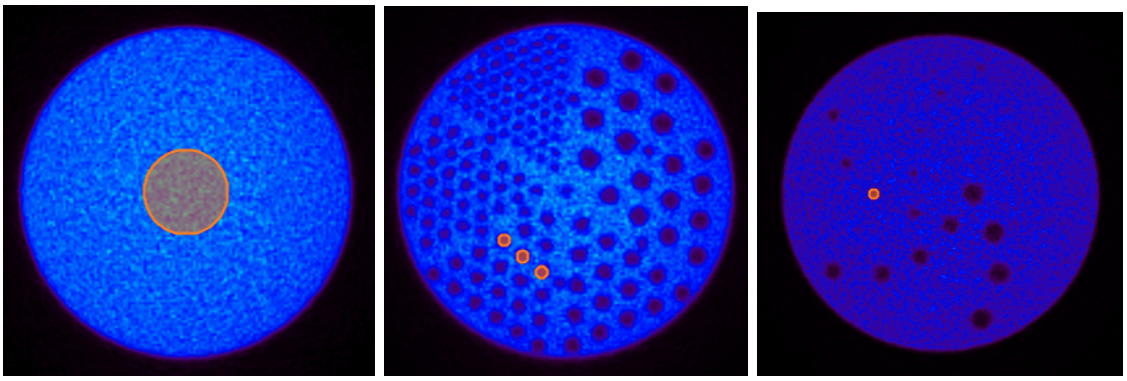

Figure 5.3 Images obtained with TOF information at 7 minutes scan and 8 iterations. Left: ROI for background in the uniform region of the Jaszczak phantom obtained from the experiment with the Siemens Biograph Vision scanner, Middle: ROI for the third replicate of 7.9 mm diameter rod (roughly at 52.5 mm from the center) in the rod part of the Jaszczak phantom obtained from the experiment with the Siemens Biograph Vision scanner, Right: ROI over the second 7.5 mm rod replica on the TOF phantom with cold rods (at 50 mm from the center) obtained from the simulation with Vision scanner.

as shown in Figure 5.3-Middle because these rods are located roughly at 52 mm from the center making them comparable with the 7.5 mm rod on TOF phantom at 50 mm from the center as shown in Figure 5.3-Right. Figure 5.3-Left shows the ROI for background over the uniform compartment of the Jaszczak phantom. The area of the background ROI was chosen to be equal to the overall area of the background ROIs considered for background on the TOF phantom. Image analysis was done by taking the average on the axial slices to cover overall 10 mm middle height of the phantom for both the experiment and simulation.

5.2.4 Simulation Study

Simulations were performed using the open-source Geant4 Application for Tomographic Emission (GATE) package v.8.2 [178]. The simulation parameters for the scanners were selected in accordance to manufacturer specifications [16, 163] and are summarized in Table 5.2. The CTR was set using the temporal resolution module of GATE. This module applies Gaussian blurring with the width specified by the coincidence time resolution in the time domain which is 215 ps to comply with the reported TOF resolution of Siemens scanner. Moreover, the UHR performance was also studied using narrower energy window to investigate how it affects the CNR performance of the scanner. The phantom was simulated using a uniform concentration of 0.0212 MBq/cc of ^{18}F in the rods and the acquisition time was fixed at 30 minutes. To calculate the CNR, a homogenous background activity was added to the phantom to provide a concentration ratio of 4:1 between the

rods and background (hot rods feature of the phantom). The activity concentration was chosen as instructed by NEMA NU2 2001 which suggests a background activity of 5.3 kBq/cc [185].

– **Reconstruction Parameters:** Images were reconstructed using the ROOT output of GATE along with the open-source Customizable and Advanced Software for Tomographic Reconstruction (CASToR) [165]. Reconstruction was performed using a 3D MLEM algorithm using multiple ray tracing with Siddon projector [166] for the UHR scanner and images were formed with a voxelization of $0.4 \times 0.4 \times 1$ mm^3. For Biograph Vision scanner, the 3D OSEM algorithm with 5 subsets was used relying on multiple ray tracing with Siddon projector; images were formed with $0.825 \times 0.825 \times 3.0$ mm^3 voxels. The voxelization and reconstruction algorithm were chosen according to the respective manufacturer softwares for each scanner. The minimum number of 5 subsets had to be chosen for the reconstruction with Siemens software. The analysis was performed on images reconstructed with 30 iterations and 8 iterations for non-TOF and TOF studies, respectively.

– **Image Analysis:** The CNR was assessed using an in-house Matlab code developed to place ROIs over each rod with the same diameter and also 16 background ROIs each with a radius of 12 mm spread over the background as shown in Figure 5.4. Images were analyzed on the 10 mm middle slices for both scanners. CNR evaluation was performed for each rod by

$$CNR_L = \frac{Mean_L - Mean_{Bg}}{\sigma_{Bg}},$$

where $Mean_L$ represents the mean of each rod, while $Mean_{Bg}$ and σ_{Bg} represent the overall mean and standard deviation of the sixteen background regions of the phantom, respectively. The results of CNR analysis was used to assess lesion detectability according to the Rose criterion that puts a quantitative limit on CNR (CNR > 5 is considered to be detectable) [179]. The radial variation of the CNR was measured for each rod diameter using

$$Parallax\ error_{(L)} = \frac{CNR_{(L,1)} - CNR_{(L,4)}}{CNR_{(L,1)}},$$

where $CNR_{(L,1)}$ stands for the CNR measured for the rod diameter of L first replica that is located at 25 mm away from the center according to Table 5.1 and $CNR_{(L,4)}$ represents the CNR obtained for rod diameter of L fourth replica, positioned at 100 mm from the center of the phantom.

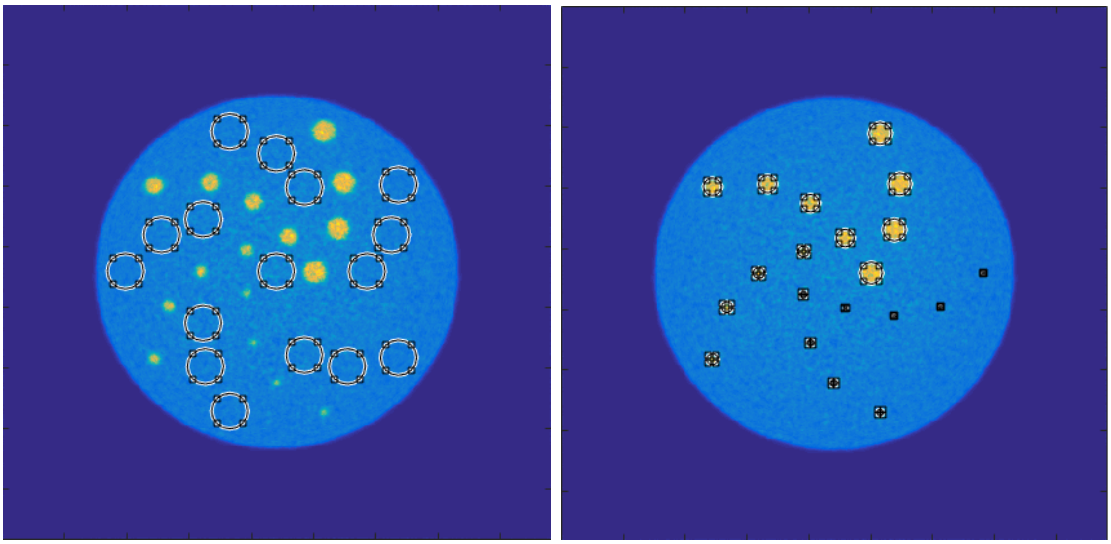

Figure 5.4 Designated ROIs for image analysis on TOF phantom. Left: ROIs for calculating overall the mean and STD of the background, Right: ROIs for calculating the mean of the rods.

5.3 Results

The results are presented in two sections. To begin with, the result of an experimental study conducted on the Siemens Biograph Vision scanner with the Jaszczak phantom is presented that is used to confirm the robustness of the simulation process. This is followed by presenting the result of a simulation study with TOF phantom using the UHR and Vision scanners.

5.3.1 Experimental Validation of the Simulations

Figure 5.5 shows the result of a comparison of CNR for the data obtained from the experiment and the simulation conducted on the Vision scanner for 3, 5, and 7 minutes acquisition times for two different number of iterations. The CNR for the experiment is measured by taking the mean of all three replicas of the rod as shown in Figure 5.3-Middle.

The difference between the results of the experiment and simulation are shown over the graph which demonstrate the CNR values from the simulation are in an excellent agreement with the CNR values from the experiment, in particular for the 7 minutes acquisition. The result of the simulation with 3 minutes scan time is slightly different from the experiment most likely due to the lack of enough counting statistics at this acquisition time.

5.3.2 Simulation Study on CNR Evaluation with the Phantom

The simulation results are presented in two steps, first the result of phantom performance is presented with UHR scanner with and without TOF resolution, second, a comparative simulation study with TOF phantom placed in the UHR and Vision scanners' FOV for

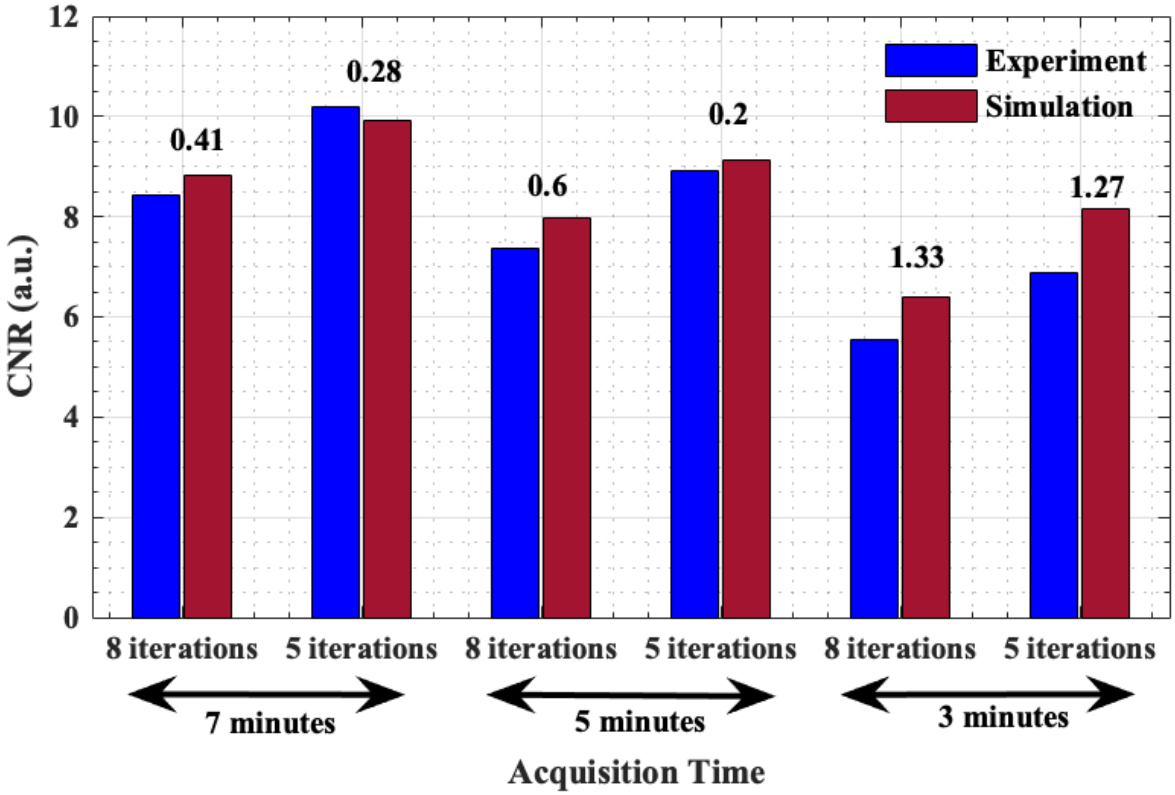

Figure 5.5 CNR comparison obtained from experiments and simulations at acquisition times of 3, 5, and 7 minutes, each at both 5 and 8 iterations. The discrepancies between the results obtained from the experiment and simulation is shown on the graph for both 5 and 8 iterations, at each scan time.

same counting statistics (20 and 30 minutes scan time for Vision and UHR scanners, respectively) and also for the same energy window with the same scan time (20 minutes).

– CNR Performance Evaluation of the UHR scanner with the Phantom

Figure 5.6 shows the CNR performance of the UHR scanner for rods with a 4.5, 7.5 and 12 mm diameter in a form of stacked bar graph with and without TOF resolution. The bars in red show the CNR without TOF resolution for each rod location while the bar corresponding to the TOF resolution in blue color depicts the increase of CNR when the TOF resolution of 215 ps is employed. As an example, the CNR value measured for the 7.5 mm diameter rod at 50 mm away from the center without TOF resolution is equal to 6.8 while with TOF resolution the measured CNR, for the same rod at the same position, is 10.6.

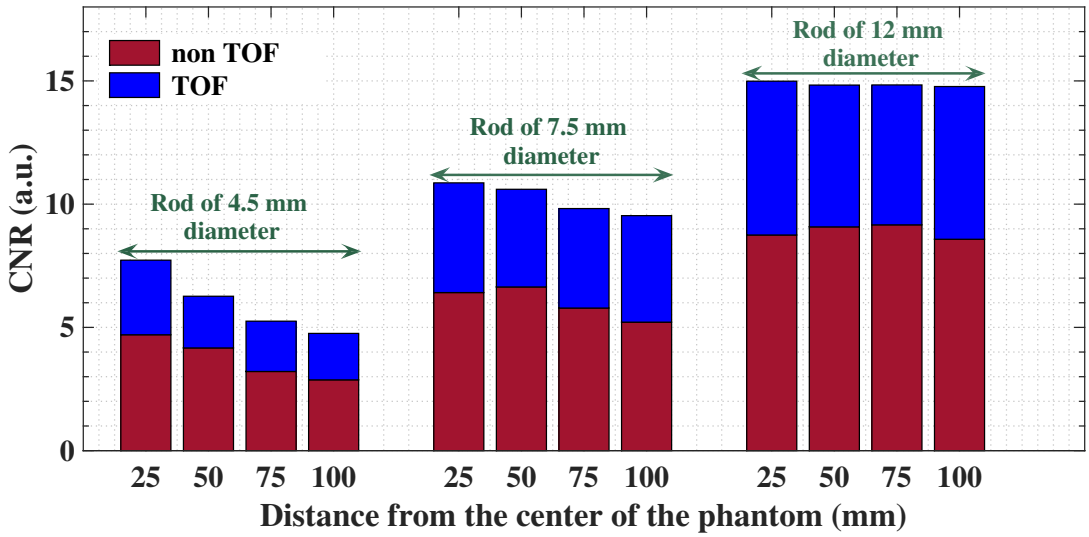

Figure 5.6 CNR performance of UHR scanner with TOF phantom for rods of 4.5, 7.5 and 12 mm diameter.

The phantom configuration clearly reveals the impact of TOF on CNR performance across the FOV. It can be seen that the TOF resolution of 215 ps leads to a gain, for all rods at any position, for the UHR scanner. It is also observed that the CNR performance for the 7.5 mm rod is rather homogenous across the FOV while the CNR is stable across the FOV for the rod of 12 mm as the measured CNR for this rod size is 15 with TOF resolution at any position. Although TOF adds gain in CNR performance for the UHR scanner, it is remarkable that the CNR for the 7.5 mm rod ($<$1 cm) is above the detection limit range (CNR $>$ 5) even without TOF resolution. The 1.5 and 15 mm rods follow the same trend as the other rods and thus are excluded from the graph.

– Comparative CNR Performance Study Using the Phantom with the UHR and Vision Scanners

Figure 5.7a shows the results of the CNR assessment for both the UHR and Siemens

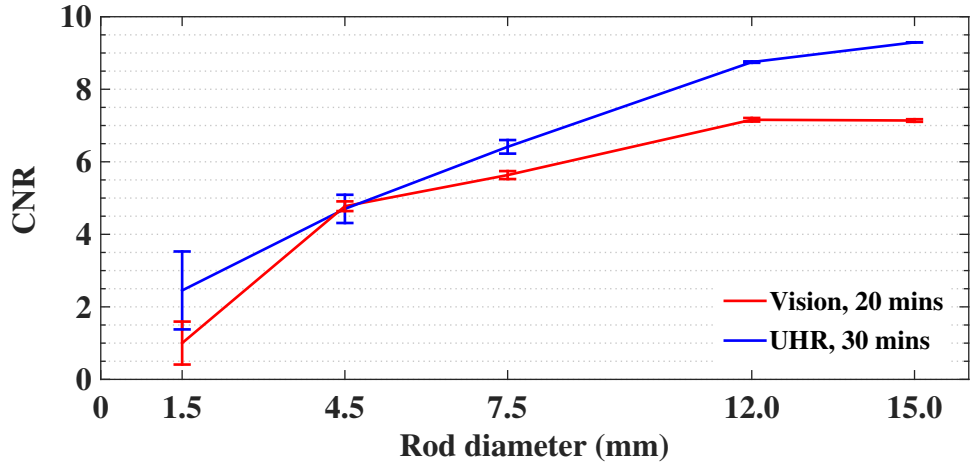

(a) Without TOF resolution at 30 iterations. The Vision scanner (6.4 x 10^6 events) and the UHR scanner with the [250 - 650 keV] energy window (6.4 x 10^6 events).

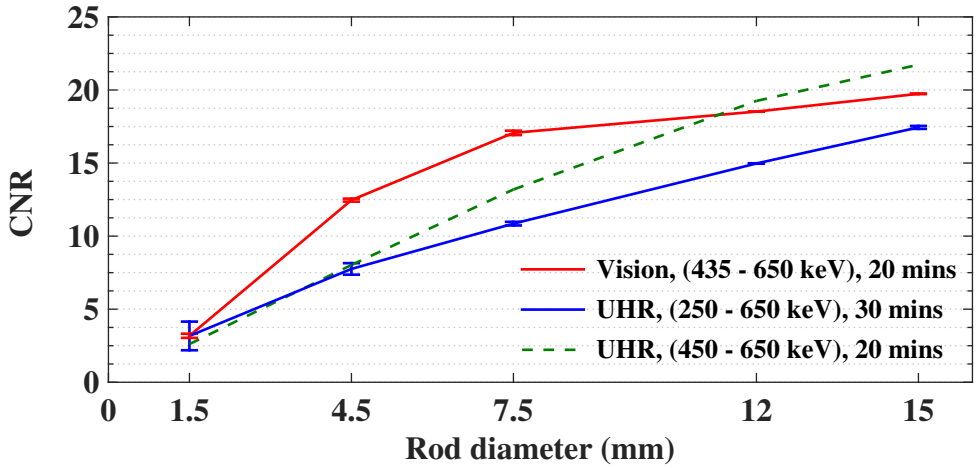

(b) With TOF resolution at 8 iterations. The Vision scanner (6.4 x 10^6 events), the UHR scanner with the [250 - 650 keV] energy window (6.4 x 10^6 events) and the UHR scanner with [450 - 650 keV] energy window (9.4 x 10^5 events)

Figure 5.7 CNR analysis for Siemens Biograph Vision and UHR scanners with TOF phantom. The error bars shows the parallax error.

Biograph Vision scanners without TOF resolution for the same counting statistics. The

CNR is shown for each rod first replica (located at 25 mm from the center for each rod) and the error bar at each rod diameter shows the parallax error measured by the corresponding equation in section 5.2.4. The CNR obtained with of the UHR scanner is shown to be superior to that of the Vision scanner without TOF information for all the rods. This is expected due to higher spatial resolution of the UHR scanner that dominates the image quality when TOF resolution is not available [163]. The matched CNR performance for the 4.5 mm rod for the UHR and Vision is due the position of this rod in the Vision scanner FOV as similar trend was observed for the rods with smaller diameter placed at the same position in the FOV. However, when TOF resolution is employed as Figure 5.7b depicts, the Vision CNR performance seems to exceed the UHR CNR performance. It was also shown that a narrower energy window ([450 - 650 keV]) for the UHR scanner that leads to much less counts, the UHR CNR performance exceeds the Vision CNR performance for larger rods. By comparing the results obtained without TOF (Figure 5.7a) to the results with TOF (Figure 5.7b), it is notable that for both the scanners, the parallax error for each rod diameter reduces when TOF resolution is employed. Hence, the phantom allows the CNR performance and parallax error to be measured as a function of position and rod diameter.

5.4 Discussion

In this research, a novel phantom is introduced that allows evaluating TOF effect on scanners CNR performance. The phantom configuration allows to study the CNR performance of the sources across the entire useful field-of-view in the presence of TOF information. The rod diameters were chosen associated with the location uncertainty of TOF resolution current state-of-the-art as well as the location uncertainty of ideal TOF resolution in future, thus containing rods from 15 mm down to 1.5 mm diameter. An experimental study was performed with Siemens Biograph Vision PET/CT scanner and its results was used to assess the validity of the simulation process. The phantom performance is then assessed by performing a simulation study with Siemens and UHR scanner models.

The simulation process is validated with an experimental study using the Jaszczak phantom and the results obtained from the experiment validate the simulation process. We are confident that the simulations performed in this work are close to reality as matched results was achieved between our simulations and experimental Biograph Vision scanner data. Thus, real experimental data when the phantom will be fabricated should lead to similar results as predicted by the simulations.

In addition, it was demonstrated that the design configuration of the phantom allows to study the CNR performance variations as a function of source transaxial position by showing that the currently achieved TOF resolution (215 ps) would provide a gain in imaging performance of the UHR scanner across the field of view. This was encouraging results that provides incentive for endowing the next generation of the UHR scanner with TOF capabilities.

Furthermore, the phantom was used as a comparative tool in a study conducted on Siemens Biograph Vision and UHR scanners. As expected the UHR outperforms Siemens Biograph Vision scanner without TOF information on the entire FOV which is absolutely due the superior spatial resolution of the scanner that is 1.2 FWHM versus that of 3.8 FWHM reported for Siemens Vision scanner [156, 163].

Whereas in the presence of TOF resolution, the CNR performance of the Siemens Biograph Vision scanner seems to be better than UHR scanner. This can be justified by acknowledging the ∼2.5 times larger transaxial FOV of the Vision scanner. As CNR enhancement by TOF resolution is a function of the TOF location uncertainty and the length of the transaxial FOV, this leads to more TOF bins in the reconstruction thus better CNR performance [189, 190]. However, it was demonstrated that if a narrower energy window ([450 - 650 keV]) is employed for UHR similar to that of Vision scanner ([435 - 650 keV]), a significant enhancement of CNR is achieved even with 6 times less events. Hence, a study for longer scan time and with narrow energy window will lead to even much more improvement in UHR CNR performance. This highlights the importance of choosing proper energy window, in particular when TOF information is available. Despite all these, it was demonstrated that, with TOF resolution, UHR scanner CNR performance is similar to the Siemens Biograph Vision scanner for the rod with the smallest diameter (rod of 1.5 mm) and this provides incentive for further investigation of CNR by including rods with diameters varying between 1 to 2.5 mm to be able to conduct a more thorough comparison on the CNR performance of the scanners.

Parallax error was assessed with the proposed phantom. By looking into the reported parallax error for each rod size, it was observed that the CNR performance is rather homogenous for the rod with the diameter of 7.5 and 15 mm all over the FOV for both the scanners. This also demonstrates including rods with larger diameters is futile in the design of the phantom as those rods are coarse enough and would be perfectly detectable even without TOF resolution with current available scanners.

Finally, a phantom was designed and evaluated that can be used as a tool to assess the TOF efficiency for the clinical scanners prior to the manufacturing and can provide much more flexibility in performance assessment of TOF scanners. In addition, the configuration of the phantom allows to gather redundant information in one simulation process that could save time, energy and resources in CNR performance evaluation of the scanners at design level.

5.5 Conclusion

In this study, a novel phantom is presented that allows for validating TOF-PET clinical scanners CNR performance. The geometry of the phantom provides flexibility in terms of studying the impact of source radial position as well as the effectiveness of incorporated TOF information. The validation of the phantom was done by conducting simulations and the robustness of the simulations were confirmed by performing an experimental study with the Siemens Biograph Vision scanner. Finally, the phantom can be used in design of TOF PET scanners to assess how available TOF information would eventually affect the scanner image performance. In future study, the experimental results with the manufactured phantom will be presented. Further application of the phantom in determining the minimum counting statistics required for the object detection in the presence of TOF resolution will be also reported.

5.6 Acknowlegements

We appreciate the assistance of Dr. Etienne Croteau and Mr. Esteban Espinosa-Bentancourt in conducting the experiments on the Siemens Biograph Vision PET/CT scanner. In addition, we would like to thank Dr. Jean-Baptiste Michaud for his help in offering resources on his Calcul Quebec and Compute Canada accounts. The authors would like to thank the Natural Sciences and Engineering Research Council of Canada (NSERC) and Mitacs for their financial support and also Calcul Quebec and Compute Canada for their technical support and assistance with this research.

CHAPTER 6

Discussion

In this work, the trade-offs affecting the CNR were investigated for the purpose of maximizing the performance of this parameter for the next generations of the LabPET II scanners, including small animal and human brain dedicated scanners.

The currently achieved CTR of 215 ps in commercial scanners is not enough to add a significant gain in small animal imaging, as the object diameter is either equal to or smaller than the location uncertainty of 30 mm associated with this CTR. Due to this, up until this study, TOF was exclusively limited to clinical scanners in the literature. However, according to the current state-of-the-art, CTR of 100 ps will soon be feasible in practice. In addition, studies have shown that a CTR of 50 ps can be achieved by increasing the dopant in the scintillators; the current world record in the laboratories is a CTR of 30 ps achieved with micro-channel plate (MCP) photodetectors. These improvements now lead to the possible extension of TOF capability to small animal imaging. Hence, the first part of this study was focused on the investigation of TOF benefits and trade-offs on image parameters for the mouse-version of the LabPET II scanner through a factorial design method by studying the impact of four factors i.e. crystal length, scan time, TOF resolution and lesion size (rod diameter).

The obtained results set the 100 ps TOF resolution as the point where TOF starts to be effective in small animal imaging. It was also demonstrated that CRC is not a sensitive parameter to evaluate the image quality as scan time variations do not affect the CRC performance significantly. In addition, it was observed that, without TOF resolution, CNR performance was reduced by decreasing the crystal length by 2 mm relative to the current length of 10.6 mm; while when TOF information was employed, CNR was not necessarily degraded. Although crystal length reduction leads to improved CTR performance, it causes a reduction of intrinsic detection efficiency (Equation 2.15), thus degrading the sensitivity. However, crystal length reduction improves the spatial resolution performance by reducing the parallax error (Equation 2.21). The common practice in PET is to choose long crystals in order to enhance counting statistics that translates into higher signal and reduced noise in the image. However, counting statistics improves imaging performance up to a certain extent, but clearly this reaches a plateau at some point where increasing counts beyond that does not necessarily lead to any improvement of the imaging performance.

On the contrary, a previous study in our group showed that even with half the counting statistics, improved spatial resolution performance can be achieved when comparing the imaging performance of the UHR brain dedicated scanner based on the LabPET II platform with the HRRT scanner by Siemens Inc. [163]. This is a demonstration that the number of detected photons is not the only prime factor in image quality performance; the ability of the scanner to precisely measure the location of interaction of the detected photons is equally important.

In this study, the CNR performance was studied as a function of scan time and TOF resolution. It was observed that TOF improvement can compensate for the loss of statistics resulting from a reduction of the scan time. Thus, considering that counting statistics is not a prime factor, and also owing to the superior spatial resolution of the LabPET II scanners, it was shown that the crystal length can be slightly reduced if accurate TOF information can be used to compensate for the loss of statistics. However it should be noted that this study was conducted for a given scanner with highly pixelated detectors. It would have to be repeated for other scanners with a different configuration if the crystal length reduction is sought [14, 18, 20].

Moreover, it is known that image reconstruction algorithms are prone to noise, and generally the noise increases with respect to the iteration number. Hence, there is an optimum iteration number that provides the best imaging performance; this depends on the size of the lesion, the counting statistics available for the reconstruction and TOF resolution. However, the results in this study were obtained for the same iteration number for all the combinations of rod sizes and TOF resolutions; this can have an impact on the CNR performance. Thus a more robust conclusion could be reached if the iteration number was also investigated; however, this would have added more complexity and computing time to the factorial design study, and hence was excluded from this research.

To obtain reliable images in PET, all three parameters of image quality i.e. spatial resolution, sensitivity and CNR should ideally be preserved. Amongst these, CNR received little attention in the literature as the priority has been so far given to the trade-offs between spatial resolution and sensitivity performance. The LabPET II platform has already been optimized for spatial resolution performance by achieving a spatial resolution approaching the physical limits imposed by the positron range and the acolinearity (0.73 mm at 1 mm from the center for mouse scanner). Thus, the second part of this work presented a further possible improvement of image quality of the LabPET II mouse-version scanner by conducting a series of simulations in order to quantify CNR performance based on three prime parameters: crystal length, lesion size and CTR. In this study, a regression analysis

was employed to parameterize CNR and derive a predictive model. This was followed by validating the model using the data from simulation and experiments. The results indicated that CNR has a positive correlation with rod size and TOF improvement and negative correlation with crystal length. The presented model provides for estimating the CNR values with MSE of 0.69 for a CTR in the range of 10 to 100 ps. The validation of the model with both experimental results and simulation confirms the robustness of the proposed approach. However, if a larger dataset was available, more advanced machine learning algorithms could be employed, allowing to predict the CNR values for a larger range of variations.

The model was derived for a small animal scanner geometry in order to reduce the computational cost, and the employed method was shown to be valid in this work by performing validation with both simulations and experiments. More robust validation with the experiments could be conducted if the scanner was TOF capable. Furthermore, the model can be readily extended in the future to other scanners, such as whole body clinical ones and if the computational cost can be tolerated, the model can also be expanded by including the variations of CNR with respect to more parameters such as iteration number, source radial position, and scan time. However, this requires more extensive analysis to be conducted, more complex numerical methods to be employed, and also the availability of the resources to handle the computational load.

Although the model is derived using ultra-fast TOF information (10 to 100 ps) that may not be currently feasible in practice, studies have shown that TOF technology is progressing by optimizing the crystal materials, dimension and coating, and the ongoing research addresses some new scintillator materials that may be a surrogate for Lutetium-based crystals in future [191]. Moreover, using Cherenkov radiators is shown to be another promising option to improve timing performance [17]. On the other hand, promising results have been published on the advancement of the SiPMs that operate at high speed in transmitting the signal coming from the scintillators that leads to improved CTR [192]. Hence, as the 10 ps worldwide challenge claims [91], there is neither a physical nor technological hurdle in achieving a CTR below 100 ps in a not too distant future. This research provides an incentive to derive a CNR predictive model for the UHR scanner from the LabPET II platform; this initiates the third part of this work.

The NEMA protocols have been the standard for evaluating the performance of PET scanners for quite some time. However, there has been a significant advancement in TOF technology in recent years, and NEMA standards have not kept up with the investigation of TOF advantages, notably with the performance across the entire FOV of the scanners.

Hence, in the third part of this work, a novel phantom was presented for the purpose of assessing TOF benefits across the FOV. The designed phantom is a cylinder that contains 20 rods that are spread spirally to cover the entire scanner's useful FOV. The rod diameters were chosen to cover current state-of-the-art TOF resolution down to expected TOF resolution in the future, as claimed in the 10 ps worldwide challenge [91]. To be able to confirm the performance of the phantom, simulations were first validated by comparing the results with an experimental study on the Siemens Biograph Vision PET/CT scanner. This is followed by performing phantom simulation studies in two clinical scanners including: the LabPET II-based UHR brain dedicated scanner and the Siemens Biograph Vision PET/CT scanner. For the purpose of experimental validation, the Jaszczak phantom was used; hence the validation process had to be carried out with hot background and cold rods configuration on the Siemens Biograph Vision scanner. Although this is not a common practice in PET, we used this configuration (cold rods) solely for the purpose of validating the simulation process; and this can be done more reliably once either the actual phantom or the UHR scanner becomes available.

It was observed that the design configuration of the phantom allows exploring the performance of the scanners all across the field of view, and to conducting a thorough comparative study. Finally, the phantom design configuration provides flexibility by allowing to study the impact of TOF on the source radial position in a single imaging session, resulting in saving time and resources, and also facilitating the analysis. This is an advantage that is not found in NEMA standards. It was observed that the proposed size for the phantom demands high computation time at both simulation and reconstruction levels; as a result, the phantom size should require some modifications *e.g.* to be the same size as the commonly used Jaszczak phantom. The phantom however requires further examination, and more reliable data could be obtained once the actual phantom is fabricated.

The TOF performance assessment of this work was conducted based on the LabPET II platform that is equipped with APDs as photodetectors, which are not TOF capable. This maybe a shortcoming of the current research in practice. However, the choice of photodetector for this platform was made according to the availability of more reliable and advanced technology for APDs at the time of designing the first prototype of these scanners (almost 12 years ago) as opposed to the emerging SiPMs at that time. The SiPMs technology has made significant progress in recent year; and it is now evident that SiPMs have to be used as a surrogate for APDs if the optimum timing performance is sought.

CHAPTER 7

ENGLISH CONCLUSION

7.1 Conclusion

In this research, a study was conducted to investigate the possible future endowment of LabPET II small animal scanners with time-of-flight (TOF) capabilities by investigating the trade-offs in their design. These scanners are unique owing to their one-to-one coupled scintillator to avalanche photodiodes (APDs) configuration. Such an approach requires complex electronics to read the signal coming from each scintillator but allows for the optimum spatial resolution performance of these scanners. Hence to further enhance the image quality for these scanners, this study is focused on contrast-to-noise (CNR) performance. Therefore, a thorough study was conducted on TOF and its impact on CNR image quality for small animal scanners; this novel approach leads to the derivation of an innovative model for CNR image performance.

The introduction chapter of this manuscript emphasized the importance of TOF technology and how it affects the image quality by enhancing small lesion detection. It was discussed that one possible approach to further improve TOF performance is crystal length reduction which is rewarding in two ways; first, it improves ultra-fast TOF (< 75 ps), leading to the enhancement of small lesion detectability or CNR; second, shorter crystal length reduces the parallax error, thus improving spatial resolution performance in the periphery of the scanner FOV. However, as shorter crystals lead to decreased sensitivity, trade-offs should be investigated. This chapter summarized the motivation for this study by discussing the fact that a model that predicts CNR performance is highly desirable in the design of PET scanners. The LabPET II mouse scanner was chosen as the model to carry out the investigation.

Chapter 2 reviewed the state-of-the-art and background in physics associated with TOF-PET. The physical parameters of PET image quality were discussed, followed by how the design parameters affect the performance of each image quality parameter. The acquisition and time chains were also detailed. This was followed by highlighting the unavoidable trade-offs in the scanner design. This chapter is concluded by describing the data modelling approach that was undertaken to implement a model for this study.

Chapter 3 presented for the first time the benefits of TOF technology for the LabPET II small animal scanner and determined that 100 ps TOF is a limit from which TOF leads to a gain in small animal imaging. In addition, the trade-offs between scan time, crystal length and coincidence time resolution (CTR) were investigated, and it was deduced that similar CNR performance can be achieved with shorter crystal length if improved TOF information is incorporated in the image reconstruction. Hence it was concluded that the crystal volume can be reduced by 19% without compromising the image quality with the help of TOF resolution of 50 ps. Besides, it was shown that TOF can compensate for sensitivity loss due to the reduction of crystal length or scan time. This research identified the most important parameters contributing to CNR performance and confirmed that TOF can be beneficial for small animal imaging using highly pixelated systems. Steady progress in TOF technology provided the incentive to further study the CNR image performance of the scanners with shorter crystal lengths and with ultra-fast CTR. It also launched a study to parameterize CNR performance that leads to deriving a CNR predictive quantitative model for the first time; this is the content of the following chapter.

In Chapter 4, a novel approach to parametrize CNR performance was introduced. In this study, a data set was prepared by conducting simulations based on a factorial design. The data set was prepared in order to study the trend in variations for three prime parameters affecting CNR performance i.e. crystal length, lesion size and CTR. The trend of variations for each parameter was then modelled by fitting a polynomial function. The validity of each designated polynomial equation was assessed. The correlation of each parameter with CNR leads to a figure of merit for CNR performance. This was followed by performing a regression analysis by assigning the 80% of the data set as a training set to derive a model for CNR performance. The remaining data (20%) was used as a test set to assess the validity of the CNR model by measuring the mean squared error (MSE). The model was further assessed by the experimental data obtained with the LabPET II mouse-version. Therefore the employed approach allowed parameterizing CNR based on design parameters. The model is an original tool to predict the CNR performance for next generation of the LabPET II scanners. Obtaining a model for the LabPET II mouse-version scanner triggered the enthusiasm for adapting the CNR model to the latest version of the LabPET II platform; a brain-dedicated PET scanner. Hence conducting an extensive CNR performance assessment in the presence of TOF resolution on a clinical scanner was a motivation to design a phantom.

Chapter 5 introduced a novel phantom that is designed for the purpose of evaluating CNR performance for TOF-PET clinical scanners. The proposed design is a cylinder

containing 20 rods with five diameters that are spread spirally to cover the entire scanner useful FOV. The configuration of the phantom allows for studying the impact of TOF on the radial positions of the sources. Furthermore, it allows determining the amount of counting statistics required to detect an object in the presence of TOF information. The phantom performance was assessed in a simulation study and the validity of the simulations was confirmed by performing an experimental study using the Siemens Biograph Vision PET/CT scanner. In addition, the phantom was used in a comparative study on CNR performance of the UHR brain scanner and Siemens Biograph Vision scanner.

Finally, the thesis provides the tools to predict the performance of LabPET II scanners implementing the TOF capability for the first time and it sets the CTR of 100 ps as the limit from which TOF can lead to a gain in small animal imaging. This is a promising results for preclinical imaging researchers as the TOF of 100 ps may soon be within reach in practice, and this study demonstrates that this would add a gain in the image performance of these scanners. This study also leads to parameterizing CNR based on design parameters by applying machine learning methods. Furthermore, a novel phantom was designed that allows for assessing CNR performance all across the field of view of TOF-PET clinical scanners.

Generally, this work aims to improve the TOF resolution by providing tools to study the timing performance of the scanner at the design level. Improving TOF translates into less radiation dose and shorter scan time as well as improved CNR performance. These benefits open new avenues at the clinical level by making PET scanners suitable for pediatric imaging as well as more frequent use of PET/CT that currently suffer from high radiation doses. Shorter scan time leads to less motion noise in the images and also allows the imaging centers to take in charge more patients during the day.

7.2 Objectives and Originality

The current work addressed four objectives that are listed below:

1. Investigating TOF benefits for small animal imaging.
2. Identifying the key parameters affecting CNR performance and their trade-offs for a highly pixelated scanner.
3. Developing a figure of merit for CNR performance evaluation and the design of future generations scanners including LabPET II scanners.
4. Designing a phantom to add flexibility in CNR performance evaluation for clinical TOF-PET scanners.

The first and second objectives were accomplished and presented in an article published in the journal of *IEEE Transaction on Radiation and Plasma Medical Sciences (TRPMS)* [50]. In this article, TOF benefit was investigated for the first time for small animal scanner and the 100 ps TOF resolution was determined as the starting range where TOF can provide some gain in small animal imaging. The factors contributing to the image CNR performance were identified by studying the trade-offs between crystal length, lesion size, TOF and scan time on image CNR performance. It was demonstrated that the crystal thickness can be reduced by 19 % without loss in image performance when TOF information of 50 ps is employed for the LabPET II mouse-version scanner.

The third objective of this work was achieved and presented in an article published in the journal *IEEE TRPMS 2021* [51]. In this research, a novel approach was employed to parametrize CNR which leads to deriving a predictive model to estimate CNR image performance at the design stage. The model can be used as a design tool for future generations of LabPET II scanners and the approach can be readily extended to any scanner.

Finally a novel phantom has been designed and evaluated that can be used in TOF performance assessment for future clinical PET scanners. The design configuration of the phantom allows for assessing the performance of the scanners all over the useful field of view, according to current state-of-the-art and future TOF technology. The results of this research have been submitted to the journal *Physics in Medicine and Biology*, thus fulfilling the fourth objective.

7.3 Perspectives and Future Work

This research was focused on studying CNR for a future TOF-capable LabPET II small animal scanner by simulations. Although the choice of the iteration number for image analysis in this research was made with caution, the CNR performance should be explored further at more iterations; this could lead to a more robust outcome. In addition, studying the variation of the CNR as a function of iteration number, source radial position, and scan time would be highly useful. It would also provide a larger dataset for CNR performance evaluation that, together with the increase of computational power, would make it possible to employ more advanced machine learning algorithms for CNR assessment.

As for the fourth objective of this study, which was designing a phantom, it remains to be fabricated. The design of the phantom could also be expanded by adding another compartment that contains spheres and also a uniformity region. The experimental results with such a phantom would be of high interest for the imaging community, as it would

allow for evaluating TOF performance rigorously and systematically over the entire field of view. However, some modifications on the phantom size and configuration may be required to make the measurements easier and the computational cost of the simulation process more practical. All these efforts will hopefully contribute enormously to the future design and characterization of TOF-PET scanners.

In practice, the current LabPET II platform is based on APDs as a photodetector; to enable the TOF capability in the future, the detector module would have to be equipped with SiPMs or SPADs to guarantee fast time performance. This necessitates adapting a new electronic block to read the signal from these faster devices. Ongoing research on new scintillator materials may possibly open new avenues, thus the new crystal material should also be studied to achieve the ultimate TOF performance in the next generation TOF-PET scanners.

CHAPTER 8

CONCLUSION FRANÇAISE

Dans le cadre de cette recherche, une étude a été menée pour équiper les scanners LabPET II avec des capacités de temps de vol (TdV) en étudiant les compromis impliqués dans la conception des scanners LabPET II lesquels sont uniques en raison de leurs scintillateurs couplés de façon individuelle à leurs photodiodes à avalanche (PDA). Une telle approche nécessite une électronique complexe pour lire le signal provenant de chaque scintillateur mais permet d'atteindre une performance de résolution spatiale optimale. Par conséquent, pour améliorer davantage la qualité d'image de ces scanners, cette étude se concentre sur les performances du rapport contrast à bruit (RCB). Donc, pour la première fois, nous avons mené une étude approfondie de TdV et son impact sur la qualité de l'image en termes de RCB pour les scanners destinés aux petits animaux, ce qui conduit à l'élaboration d'un modèle innovant pour les performances du RCB de l'image.

Le chapitre d'introduction de ce manuscrit a souligné l'importance de la technologie TdV et la manière dont elle affecte la qualité de l'image en améliorant la détection des petites lésions. Une approche possible pour améliorer davantage les performances du TdV, soit la réduction de la longueur des cristaux, est avantageuse pour deux raisons; tout d'abord, améliorer le TdV ultra rapide (< 75 ps) qui conduit à une meilleure détectabilité des petites lésions ou RCB; ensuite, l'usage de cristaux plus court réduit l'erreur de parallaxe, améliorant ainsi les performances de résolution spatiale à la périphérie du scanner. Cependant, comme des cristaux courts entraînent une diminution de la sensibilité, les effets de ces compromis doivent être étudiés. Ce chapitre a résumé la motivation de cette étude en discutant du fait qu'un modèle qui prévoit les performances du RCB est hautement souhaitable dans la conception de scanners TEP. Le scanner LabPET II modèle souris a été choisi comme modèle pour mener l'étude.

Le chapitre 2 a passé en revue l'état de l'art et le contexte de la physique associés à la TEP-TdV. Les paramètres physiques de la qualité de l'image TEP sont discutés, suivis des facteurs de conception affectant les performances de chacun de ces paramètres. Les chaînes d'acquisition et de temps ont également été détaillées, suivies par une discussion des compromis indispensables à la conception du scanner. Ce chapitre se termine par une approche de modélisation des données qui a été entreprise pour élaborer le modèle utilisé dans cette étude.

Le chapitre 3 a présenté pour la première fois les avantages de la technologie TdV pour les scanners de petits animaux LabPET II et a déterminé que 100 ps constitue la limite à partir de laquelle le TdV contribue positivement à l'imagerie des petits animaux. Les compromis entre le temps d'acquisition, la longueur du cristal et la RTC ont été étudiés et Nous avons déterminé que les mêmes performances de RCB peuvent être obtenues avec une longueur de cristal plus courte si des résolutions temporelle améliorées sont incorporées dans la reconstruction d'image. Par conséquent, on a conclu que le volume de cristal peut être réduit de 19% sans compromettre la qualité de l'image à l'aide d'un TdV de 50 ps. En outre, il a été montré que le TdV peut compenser la perte de sensibilité en réduisant la longueur du cristal ou le temps d'acquisition. Ces travaux de recherche ont ciblé les paramètres les plus importants contribuant à la performance du RCB et ont démontré que le TdV peut être bénéfique à l'imagerie des petits animaux pour des systèmes hautement pixelisés. Les progrès constants de la technologie TdV ont incité à étudier plus loin les performances d'images RCB des scanners avec de longueurs de cristaux plus courtes et avec une RTC ultra-rapide. Cette étude a aussi lancé des travaux pour paramétrer les performances du RCB qui ont mené à l'élaboration d'un modèle quantitatif prédictif du RCB pour la première fois, ce qui est le sujet du chapitre suivant.

Dans le chapitre 4, une nouvelle approche pour paramétrer les performances du RCB a été introduite. Dans cette étude, nous avons préparé un ensemble de données en effectuant des simulations basées sur une analyse factorielle. L'ensemble de données a été préparé pour étudier la tendance des variations de trois principaux paramètres affectant les performances du RCB, à savoir la longueur des cristaux, la taille des lésions et la résolution temporelle en coïncidence (RTC). La tendance des variations pour chaque paramètre a ensuite été modélisée en leur attribuant une fonction polynomiale. La validité de chaque équation polynomiale désignée a été évaluée. La corrélation de ces paramètres avec le RCB conduit un facteur de qualité en lien avec la performance du RCB. Ensuite, une analyse de régression a été utilisée en considérant 80% de l'ensemble de données comme un ensemble d'apprentissage pour dériver un modèle de performance RCB. Les données restantes (20%) a été utilisé comme ensemble de test pour évaluer la validité du modèle RCB en mesurant l'erreur quadratique moyenne (EQM). L'évaluation du modèle s'est poursuivie par le traitement des données expérimentales obtenues avec la version souris du scanner LabPET II. Par conséquent, l'approche employée a permis de paramétrer le RCB en fonction des paramètres de conception. Ce modèle est un outil original pour prédire les performances du RCB pour la prochaine génération de scanner LabPET II. L'obtention d'un modèle pour le scanner LabPET II version souris suscite l'intérêt pour l'adaptation d'un modèle de RCB pour la dernière version de la plateforme LabPET II, un scanner

dédié à l'imagerie du cerveau. Par conséquent, être en mesure d'effectuer l'évaluation des performances du RCB sur un scanner clinique était la motivation derrière la conception d'une mire.

Le chapitre 5 a présenté une nouvelle mire conçue dans le but d'évaluer les performances du TdV pour les scanners cliniques. La conception proposée est un cylindre contenant 20 tiges de cinq diamètres différents qui sont réparties en spirale pour couvrir l'ensemble du champ de vue utile des scanners. La configuration de la mire permet d'étudier l'impact du TdV sur les positions radiales des sources. De plus, elle permet de déterminer le nombre d'événements nécessaires pour détecter un objet en présence de données TdV. Les performances de la mire ont été évaluées dans une étude de simulation dont la validité a été confirmée en effectuant une étude expérimentale à l'aide d'un scanner Siemens Biograph Vision. De plus, la mire a été utilisée dans une étude comparative des performances RCB du scanner cérébral LabPET UHR et du scanner Siemens Biograph Vision.

Enfin, cette thèse fournit les outils pour prédire les performances des scanners LabPET II avec la capacité TdV et de définir la RTC de 100 ps comme la limite à partir de laquelle le TdV peut offrir un avantage en imagerie chez le petit animal. Il s'agit d'un résultat prometteur pour les chercheurs en imagerie préclinique, car un TdV de 100 ps pourrait bientôt être accessible expérimentalement et cette étude a montré que cela ajouterait un gain sur les performances d'imagerie de ces scanners. Cette étude conduit également à paramétrer le RCB en fonction des paramètres de conception des scanners en appliquant des méthodes d'apprentissage automatique. De plus, une nouvelle mire a été conçue, permettent d'évaluer les performances TdV dans l'ensemble du champ de vue des scanners cliniques.

En général, ce travail vise à améliorer la résolution TdV en fournissant des outils pour étudier le résolution temporelle du scanner au niveau de la conception. L'amélioration du TdV se traduit par une dose de rayonnement moindre et un temps d'acquisition plus court, ainsi qu'une amélioration de RCB. Ces avantages ouvrent de nouvelles possibilités au niveau clinique en rendant les scanners TEP mieux adaptés à l'imagerie pédiatrique ainsi qu'à une utilisation plus fréquente des TEP/TDM qui souffrent actuellement de fortes doses de rayonnement. Un temps d'acquisition plus court entraîne moins de bruit de mouvement dans les images et permet également aux centres d'imagerie d'accepter plus de patients dans une journée.

8.1 Objectifs et originalité

Les travaux en cours ont porté sur quatre objectifs, énumérés ci-dessous :

1. Étudier les avantages du TdV pour l'imagerie des petits animaux.
2. Identifier les paramètres clés affectant les performances RCB et leurs compromis pour un scanner hautement pixelisé.
3. Développer un facteur de qualité pour l'évaluation des performances du RCB destinée la conception des futures générations de scanners, y compris les scanners LabPET II.
4. Concevoir une mire pour ajouter davantage de flexibilité à l'évaluation des performances de RBC des scanners TEP TdV cliniques.

Le premier et le deuxième objectifs ont été atteints et présentés dans le cadre un article publié dans le journal *IEEE Transaction on Radiation and Plasma Medical Sciences (TRPMS)* [50]. Dans cet article, l'avantage de faire appel au TdV a été étudié pour la première fois sur un scanner pour petits animaux et une résolution TdV de 100 ps a été déterminée comme valeur limite pour laquelle le TdV peut représenter un avantage pour l'imagerie de petits animaux. Les facteurs contribuant à la performance du RCB de l'image ont été identifiés en étudiant les compromis entre la longueur des cristaux, la taille de la lésion, le TdV et le temps d'acquisition de l'image sur les performances du RCB de cette image. Il a été démontré que l'épaisseur du cristal peut être diminuée de 19 % sans détériorer les performances de l'image lorsque une résolution TdV de 50 ps a prise en compte pour le scanner LabPET II version souris.

Le troisième objectif de ce travail de recherche a été atteint et présenté dans un article publié dans le journal *IEEE Transaction on Radiation and Plasma Medical Sciences (TRPMS)* [51]. Dans cette recherche, une nouvelle approche a été utilisée pour paramétrer le RCB, ce qui conduit à l'élaboration d'un modèle prédictif permettant d'estimer les performances du RCB de l'image au stade de la conception des scanners. Le modèle peut être utilisé comme outil de conception pour les futures générations de scanners LabPET et cette approche peut être facilement adaptée à n'importe quel scanner.

Enfin, une nouvelle mire a été conçue et évaluée pour être employée dans l'évaluation des performances RBC des prochains scanners TEP TdV cliniques. La configuration de la mire permet d'évaluer les performances des scanners sur l'ensemble du champ de vue et conformément à l'état de l'art actuel et futur de la technologie TdV. Les résultats de cette recherche ont été soumis au journal *Physics in Medicine and Biology*, satisfaisant ainsi le quatrième objectif.

8.2 Perspectives et Futurs Travaux

Cette recherche s'est concentrée sur l'étude par simulation du RCB pour un scanner pour petits animaux LabPET II intégrant le TdV. Bien que le choix du nombre d'itérations

pour l'analyse d'image ait été fait avec précaution, les performances du RCB devraient être explorées plus avant avec un plus grand nombre d'itérations, ce qui pourrait conduire aux résultats plus robustes. De plus, l'étude de la variation du RCB en fonction du nombre d'itérations, de la position radiale de la source et du temps d'acquisition serait souhaitable. Cela fournirait également un ensemble de données plus important pour l'évaluation des performances du RCB qui, associé à l'augmentation de la puissance de calcul, permettrait d'utiliser des algorithmes d'apprentissage automatique plus avancés pour l'évaluation du RCB.

Quant au quatrième objectif de cette étude qui était de concevoir une mire, elle doit encore être fabriquée. La conception de la mire pourrait aussi être améliorée en y ajoutant un autre compartiment qui comprend des sphères et une région uniforme. Les résultats expérimentaux avec une telle mire seraient d'un grand intérêt pour la communauté en imagerie, car ils permettraient d'évaluer rigoureusement et systématiquement les performances du TdV sur l'ensemble du champ de vision. Cependant, certaines modifications sur la taille et la configuration de la mire peuvent être nécessaires pour rendre le coût de calcul du processus de simulation plus efficace et plus pratique. Nous espérons que tous ces efforts contribueront substantiellement à la conception future et à la caractérisation des scanners TEP TdV.

En pratique, la plateforme LabPET II actuelle est fondée sur des photodétecteurs à base de photodiodes avalanche. Pour activer la capacité TdV à l'avenir, la conception du module de détection doit être équipé de SiPM ou de SPAD pour garantir des performances rapides. Cela nécessite d'adapter un nouveau bloc électronique pour lire le signal de ces appareils plus rapides. Les recherches en cours sur de nouveaux matériaux de scintillation pourraient éventuellement ouvrir de nouvelles voie. Ces nouveaux matériaux devront également être étudiés pour atteindre les performances TdV ultimes pour la prochaine génération de scanners TEP-TdV.

LIST OF REFERENCES

[1] J. S. Karp, S. Surti, M. E. Daube-Witherspoon, and G. Muehllehner. Benefit of time-of-flight in PET: experimental and clinical results. *J Nucl Med*, 49(3):462–470, Mar 2008.

[2] Anders Brahme. *Comprehensive Biomedical Physics*. Elsevier, The Boulevard, Langford Lane, Kidlington, Oxford OX5 1GB, UK, 2014.

[3] Statistics Canada (2020). Leading causes of death, total population, by age group. `https://www150.statcan.gc.ca/t1/tbl1/en/cv.action?pid=1310039401`, Accessed June, 2021.

[4] Canadian Cancer Statistics (2019). Canadian cancer statistics advisory committee. `https://cancer.ca/en/research/cancer-statistics/canadian-cancer-statistics`, Accessed July, 2021.

[5] Heiko Schöder and Mithat Gönen. Screening for cancer with PET and PET/CT: Potential and limitations. *J. Nucl. Med.*, 48(1 suppl):4S–18S, 2007.

[6] H. P. Chan, W. S. Liu, W. S. Liou, C. Hu, Y. L. Chiu, and N. J. Peng. Comparison of FDG-PET/CT for Cancer Detection in Populations With Different Risks of Underlying Malignancy. *In Vivo*, 34(1):469–478, 2020.

[7] Richard Pither. PET and the role of in vivo molecular imaging in personalized medicine. *Expert Rev. Mol. Diagn.*, 3(6):703–13, 2003.

[8] Sanjiv Sam Gambhir. Molecular imaging of cancer with positron emission tomography. *Nat Rev Cancer*, 2(9):683–693, 2002.

[9] R. Yao, R. Lecomte, and E. S. Crawford. Small-Animal PET: What Is It, and Why Do We Need It? *J. Nucl. Med. Technol.*, 40(3):157–165, 2012.

[10] Dunn. W.L. Time-of-flight localization of positron emitting isotopes. *Thesis in physics - Vanderbilt University- Nashville Tenessee*, 1975.

[11] T. K. Lewellen. Recent developments in PET detector technology. *Phys. Med. Biol.*, 53(17):287–317, Sep 2008.

[12] M M Ter-Pogossian, D C Ficke, M Yamamoto, and J T Hood. Super PETT I: A Positron Emission Tomograph Utilizing Photon Time-of-Flight Information. *IEEE Trans. Med. Imaging*, 1(3):179–187, 1982.

[13] Wai Hoi Wong, Nizar A. Mullani, Gary Wardworth, Ross K. Hartz, and David Bristow. Characteristics of small barium fluoride (BaF2.) scintillator for high intrinsic resolution time-of-flight positron emission tomography. *IEEE Trans. Nucl. Sci.*, 31(1):381–386, 1984.

[14] Maurizio Conti et al. First experimental results of time-of-flight reconstruction on an LSO PET scanner. *Phys. Med. Biol.*, 50(19):4507–4526, 2005.

[15] S. Surti, J.S. Karp, G. Muehllehner, and P.S. Raby. Investigation of lanthanum scintillators for 3D PET. In *2002 IEEE Nucl. Sci. Symp. Med. Imaging Conf. Rec.*, volume 2, pages 1177–1181 vol.2, 2002.

[16] Joyce J van Sluis et al. Performance characteristics of the digital Biograph Vision PET/CT system. *J. Nucl. Med.*, 60(7):1031–1036, 2019.

[17] R Ota et al. Coincidence time resolution of 30 ps FWHM using a pair of Cherenkov-radiator-integrated MCP-PMTs. *Phys. Med. Biol.*, 64(7):07LT01, Mar 2019.

[18] W. W. Moses. Time of flight in PET Revisited. *IEEE Trans. Nucl. Sci.*, 50(5 II):1325–1330, 2003.

[19] Maurizio Conti. Effect of randoms on signal-to-noise-ratio in TOF PET. *IEEE Nucl. Sci. Symp. Conf. Rec.*, 3(3):1590–1595, 2005.

[20] Maurizio Conti. Focus on time-of-flight PET: The benefits of improved time resolution. *Eur J Nucl Med Mol Imaging*, 38:1147–57, 06 2011.

[21] Maurizio Conti. Improving time resolution in time-of-flight PET. *Nucl. Instrum. Methods. Phys. Res. B*, 648:S194 – S198, 2011.

[22] Joshua D. Schaefferkoetter, Jianhua Yan, David W. Townsend, and Maurizio Conti. Initial assessment of image quality for low-dose PET: Evaluation of lesion detectability. *Phys. Med. Biol.*, 60(14):5543–5556, 2015.

[23] William W. Moses. Fundamental limits of spatial resolution in PET. *Nucl. Instruments Methods Phys. Res. Sect. A Accel. Spectrometers, Detect. Assoc. Equip.*, 648(SUPPL. 1):S236–S240, 2011.

[24] Maxime Toussaint, Roger Lecomte, and Jean-Pierre Dussault. Improvement of spatial resolution with iterative PET reconstruction using ultrafast TOF. *IEEE Trans. Rad. Plasma Med. Sci.*, 5(5):729–737, 2021.

[25] S. Cherry, J. Sorenson, and M. Phelps. *Physics in Nuclear Medicine*. Elsevier Health Sciences, 2012.

[26] M E Daube-Witherspoon, S Surti, A Perkins, C C M Kyba, R Wiener, M E Werner, R Kulp, and J S Karp. The imaging performance of a LaBr3-based PET scanner. *Phys. Med. Biol.*, 55(1):45–64, 2010.

[27] Xiaoli Li, Adam M Alessio, Thompson H Burnett, and Thomas K Lewellen. Performance Evaluation of Small Animal PET Scanners With Different System Designs. *IEEE Trans Nucl Sci.*, 60(3):1495–1502, 2013.

[28] Seiichi Yamamoto, Hitoshi Horii, Mitsuru Hurutani, Keiichi Matsumoto, and Michio Senda. Investigation of single, random, and true counts from natural radioactivity in LSO-based clinical PET. *Ann. Nucl. Med.*, 19(2):109–114, 2005.

[29] Suleman Surti. Update on time-of-flight PET imaging. *J. Nucl. Med.*, 56(1):98–105, 2015.

[30] S Surti, M E Werner, and J S Karp. Study of PET scanner designs using clinical metrics to optimize the scanner axial FOV and crystal thickness. *Phys. Med. Biol.*, 58(12):3995–4012, 2013.

[31] Suleman Surti, Adam R. Shore, and Joel S. Karp. Design study of a whole-body PET scanner with improved spatial and timing resolution. *IEEE Trans. Nucl. Sci.*, 60(5):3220–3226, 2013.

[32] S. Gundacker, A. Knapitsch, E. Auffray, P. Jarron, T. Meyer, and P. Lecoq. Time resolution deterioration with increasing crystal length in a TOF-PET system. *Nucl. Instruments Methods Phys. Res. Sect. A Accel. Spectrometers, Detect. Assoc. Equip.*, 737(2014):92–100, 2014.

[33] E. Auffray, B. Frisch, F. Geraci, A. Ghezzi, S. Gundacker, H. Hillemanns, P. Jarron, T. Meyer, M. Paganoni, K. Pauwels, M. Pizzichemi, and P. Lecoq. A comprehensive and systematic study of coincidence time resolution and light yield using scintillators of different size and wrapping. *IEEE Trans. Nucl. Sci.*, 60(5):3163–3171, 2013.

[34] Fréderic Nolet et al. Quenching circuit and SPAD integrated in CMOS 65 nm with 7.8 ps FWHM single photon timing resolution. *Instruments*, 2(4):19, 2018.

[35] Jean-François Pratte et al. 3D Photon-To-Digital Converter for Radiation Instrumentation: Motivation and Future Works. *Sensors*, 21(2), 2021.

[36] Ronald Nutt. The history of positron emission tomography. *Mol. Imaging Biol.*, 4(1):11–26, 2002.

[37] H. O. Anger and A. Gottschalk. Localization of Brain Tumors with the Positron Scintillation Camera. *J Nucl Med*, 4:326–330, Jul 1963.

[38] W. H. Sweet. The uses of nuclear disintegration in the diagnosis and treatment of brain tumor. *N Engl J Med*, 245(23):875–878, Dec 1951.

[39] S Rankowitz, J S Robertson, W A Higinbotham, and M J Rosenblum. Positron scanner for locating brain tumors. *Inst. Radio Engrs.*, 3 1961.

[40] M. E. Phelps, S. C. Huang, E. J. Hoffman, C. Selin, L. Sokoloff, and D. E. Kuhl. Tomographic measurement of local cerebral glucose metabolic rate in humans with (F-18)2-fluoro-2-deoxy-D-glucose: validation of method. *Ann Neurol*, 6(5):371–388, Nov 1979.

[41] Suleman Surti, Austin Kuhn, Matthew E Werner, Amy E Perkins, Jeffrey Kolthammer, and Joel S Karp. Performance of Philips Gemini TF PET/CT scanner with special consideration for its time-of-flight imaging capabilities. *J. Nucl. Med.*, 48(3):471–480, 2007.

[42] R. D. Badawi, H. Shi, P. Hu, S. Chen, T. Xu, P. M. Price, Y. Ding, B. A. Spencer, L. Nardo, W. Liu, J. Bao, T. Jones, H. Li, and S. R. Cherry. First Human Imaging Studies with the EXPLORER Total-Body PET Scanner. *J Nucl Med*, 60(3):299–303, 03 2019.

[43] T. Beyer, D. W. Townsend, T. Brun, P. E. Kinahan, M. Charron, R. Roddy, J. Jerin, J. Young, L. Byars, and R. Nutt. A combined PET/CT scanner for clinical oncology. *J Nucl Med*, 41(8):1369–1379, Aug 2000.

[44] Yiping Shao, Simon R Cherry, Keyvan Farahani, Ken Meadors, Stefan Siegel, Robert W Silverman, and Paul K Marsden. Simultaneous PET and MR imaging. *phys. Med. Biol.*, 42(10):1965–1970, oct 1997.

[45] P. M. Bloomfield, S. Rajeswaran, T. J. Spinks, S. P. Hume, R. Myers, S. Ashworth, K. M. Clifford, W. F. Jones, L. G. Byars, and J. Young. The design and physical characteristics of a small animal positron emission tomograph. *Phys. Med. Biol.*, 40(6):1105–1126, Jun 1995.

[46] S.R. Cherry, Yiping Shao, S. Siegel, R.W. Silverman, E. Mumcuoglu, K. Meadors, and M.E. Phelps. Optical fiber readout of scintillator arrays using a multi-channel pmt: a high resolution pet detector for animal imaging. *IEEE Trans. Nucl. Sci.*, 43(3):1932–1937, 1996.

[47] R. Lecomte, J. Cadorette, S. Rodrigue, D. Lapointe, D. Rouleau, M. Bentourkia, R. Yao, and P. Msaki. Initial results from the sherbrooke avalanche photodiode positron tomograph. *IEEE Trans. Nucl. Sci.*, 43(3):1952–1957, 1996.

[48] Mélanie Bergeron, Jules Cadorette, Jean-Francois Beaudoin, Jacques A. Rousseau, Marc Dumoulin, Martin Lepage, Ghislain Robert, Vitali Selivanov, Marc-André Tétrault, Nicolas Viscogliosi, Tyler Dumouchel, Stephanie Thorn, Jean DaSilva, Robert A. deKemp, Jeffrey P. Norenberg, Réjean Fontaine, and Roger Lecomte. Performance evaluation of the LabPET^{TM} APD-based digital PET scanner. In *2007 IEEE Nucl. Sci. Symp. Med. Imaging Conf. Rec.(NSS/MIC)*, volume 6, pages 4185–4191, 2007.

[49] Émilie Gaudin, Christian Thibaudeau, Louis Arpin, Jean-Daniel Leroux, Jean-Franois Beaudoin, Jules Cadorette, Larissa Njejimana, Arnaud Samson, Jonathan Bouchard, Konin Koua, Réjean Fontaine, and Roger Lecomte. Initial results of a truly pixelated APD-based PET scanner for high-resolution preclinical imaging. *J. Nucl. Med.*, 58(supplement 1):91, 2017.

[50] Nikta Zarif Yussefian, Maxime Toussaint, Émilie Gaudin, Roger Lecomte, and Réjean Fontaine. TOF Benefits and Trade-offs on Image Contrast-to-Noise Ratio Performance for a Small Animal PET Scanner. *IEEE Trans. Rad. Plasma Med. Sci.*, 5(5):687–693, 2021.

[51] Nikta Zarif Yussefian, Émilie Gaudin, Roger Lecomte, and Réjean Fontaine. Predicting Small Lesion Detectability for a Small Animal TOF PET Scanner. *IEEE Trans. Rad. Plasma Med. Sci. (Early Access)*, 2021.

[52] Nikta Zarif Yussefian, Émilie Gaudin, Roger Lecomte, and Réjean Fontaine. Novel phantom for practical performance evaluation of TOF-PET scanners. *Phys. Med. Biol.*, 2021(Submitted).

[53] B. M. Gallagher, A. Ansari, H. Atkins, V. Casella, D. R. Christman, J. S. Fowler, T. Ido, R. R. MacGregor, P. Som, C. N. Wan, A. P. Wolf, D. E. Kuhl, and M. Reivich. Radiopharmaceuticals XXVII. 18F-labeled 2-deoxy-2-fluoro-d-glucose as a radiopharmaceutical for measuring regional myocardial glucose metabolism in vivo: tissue distribution and imaging studies in animals. *J Nucl Med*, 18(10):990–996, Oct 1977.

[54] T. L. Collier, R. Lecomte, T. J. McCarthy, S. Meikle, T. J. Ruth, F. Scopinaro, A. Signore, H. VanBrocklin, C. van De Wiele, and R. N. Waterhouse. Assessment of cancer-associated biomarkers by positron emission tomography: advances and challenges. *Dis Markers*, 18(5-6):211–247, 2002.

[55] A. Abi-Dargham, N. Simpson, L. Kegeles, R. Parsey, D. R. Hwang, S. Anjilvel, Y. Zea-Ponce, I. Lombardo, R. Van Heertum, J. J. Mann, C. Foged, C. Halldin, and M. Laruelle. PET studies of binding competition between endogenous dopamine and the D1 radiotracer [11C]NNC 756. *Synapse*, 32(2):93–109, May 1999.

[56] G. V. Taplin, E. K. Dore, and D. E. Johson. The Quantitative Radiorenogram for Total Differential Renal Blood Flow Measurements. *UCLA Rep*, 86:1–18, Jun 1963.

[57] J. G. Hamilton. The Rates of Absorption of Radio-Sodium in Normal Human Subjects. *Proc Natl Acad Sci U S A*, 23(9):521–527, Sep 1937.

[58] N. A. Dyson, P. Hugh-Jones, G. R. Newbery, J. D. Sinclair, and J. B. West. Studies of regional lung function using radioactive oxygen. *Br Med J*, 1(5168):231–238, Jan 1960.

[59] D. Comar, J. Cartron, M. Maziere, and C. Marazano. Labelling and metabolism of methionine-methyl-11 C. *Eur J Nucl Med*, 1(1):11–14, 1976.

[60] L. B. Solnes, R. A. Werner, K. M. Jones, M. S. Sadaghiani, C. R. Bailey, C. Lapa, M. G. Pomper, and S. P. Rowe. Theranostics: Leveraging Molecular Imaging and Therapy to Impact Patient Management and Secure the Future of Nuclear Medicine. *J Nucl Med*, 61(3):311–318, 03 2020.

[61] W.S. Choong, Q Peng, C Q Vu, B T Turko, and W W Moses. High-performance electronics for time-of-flight PET systems. *J. Instrum.*, 8(1):T01006, 2013.

[62] P. Lecoq, E. Auffray, S. Brunner, H. Hillemanns, P. Jarron, A. Knapitsch, T. Meyer, and F. Powolny. Factors influencing time resolution of scintillators and ways to improve them. *IEEE Trans. Nucl. Sci.*, 57(5 PART 1):2411–2416, 2010.

[63] M. M. Ter-Pogossian, M. E. Phelps, E. J. Hoffman, and N. A. Mullani. A positron-emission transaxial tomograph for nuclear imaging (PETT). *Radiology*, 114(1):89–98, Jan 1975.

[64] M. R. Farukhi. Bi4Ge3O12 (BGO) - a scintillator replacement for NaI(Tl). *MRS Proceedings*, 16:115, 1982.

[65] N. Zhang, Z. Ding, Y. Wu, and M. Salomon. Study of a large BGO crystal in a charged particle beam. *IEEE Trans. Nucl. Sci.*, 37(2):216–219, 1990.

[66] C.L. Melcher and J.S. Schweitzer. A promising new scintillator: cerium-doped lutetium oxyorthosilicate. *Nucl. Instruments Methods Phys. Res. Sect. A Accel. Spectrometers, Detect. Assoc. Equip.*, 314(1):212–214, 1992.

[67] Emilie Roncali and Simon R. Cherry. Application of silicon photomultipliers to positron emission tomography. *Ann. Biomed. Eng.*, 39(4):1358–1377, 2011.

[68] R. Lecomte, D. Schmitt, A. W. Lightstone, and R. J. McIntyre. Performance characteristics of BGO-silicon avalanche photodiode detectors for PET. *IEEE Trans. Nucl. Sci.*, 32(1):482–486, 1985.

[69] Glenn F. Knoll. *Radiation Detection and Measurement*. John Wiley and Sons, New York, 3rd edition, 2000.

[70] John L Humm, Anatoly Rosenfeld, and Alberto Del Guerra. From PET detectors to PET scanners. *Eur. J. Nucl. Med. Mol. Imaging*, 30(11):1574–1597, 2003.

[71] Stefan Seifert, Ruud Vinke, Herman T. Van Dam, Herbert Löhner, Peter Dendooven, Freek J. Beekman, and Dennis R. Schaart. Ultra precise timing with SiPM-based TOF PET scintillation detectors. *IEEE Nucl. Sci. Symp. Conf. Rec.*, pages 2329–2333, 2009.

[72] M.-A. Tétrault, N. Viscogliosi, J. Riendeau, F. Belanger, J. B. Michaud, H. Semmaoui, P. Berard, F. Lemieux, L. Arpin, J. Cadorette, C. M. Pepin, G. Robert, M. D. Lepage, R. Lecomte, and R. Fontaine. System integration of the LabPET small animal PET scanner. In *2006 IEEE Nucl. Sci. Symp. Conf. Rec.*, volume 3, pages 1880–1884, 2006.

[73] Habib Zaidi, Marie-Louise Montandon, and Abass Alavi. Advances in attenuation correction techniques in PET. *PET Clinics*, 2(2):191–217, 2007. PET Instrumentation and Quantification.

[74] Guillem Pratx and Craig Levin. Online detector response calculations for high-resolution PET image reconstruction. *Phys. Med. Biol.*, 56(13):4023–40, 2011.

[75] M. Bentourkia, P. Msaki, J. Cadorette, and R. Lecomte. Assessment of scatter components in high-resolution pet: Correction by nonstationary convolution subtraction. *Journal of Nuclear Medicine*, 36(1):121–132, January 1995.

[76] Habib Zaidi and Kenneth F Koral. Scatter modelling and compensation in emission tomography. *Eur. J. Nucl. Med. Mol. Imaging*, 31(5):761–782, 2004.

[77] Habib Zaidi and Marie Louise Montandon. Scatter Compensation Techniques in PET. *PET Clin.*, 2(2):219–234, 2007.

[78] C.S. Levin, M. Dahlbom, and E.J. Hoffman. A Monte Carlo correction for the effect of Compton scattering in 3-D PET brain imaging. *IEEE Trans. Nucl. Sci.*, 42(4):1181–1185, 1995.

[79] K. Magota, T. Shiga, Y. Asano, D. Shinyama, J. Ye, A. E. Perkins, P. J. Maniawski, T. Toyonaga, K. Kobayashi, K. Hirata, C. Katoh, N. Hattori, and N. Tamaki. J Nucl MedScatter Correction with Combined Single-Scatter Simulation and Monte Carlo Simulation Scaling Improved the Visual Artifacts and Quantification in 3-Dimensional Brain PET/CT Imaging with 15O-Gas Inhalation. *J Nucl Med*, 58(12):2020–2025, 12 2017.

[80] R. Accorsi, L. E. Adam, M. E. Werner, and J. S. Karp. Optimization of a fully 3D single scatter simulation algorithm for 3D PET. *Phys. Med. Biol.*, 49(12):2577–2598, Jun 2004.

[81] Réjean Fontaine, François Bélanger, Nicolas Viscogliosi, Hicham Semmaoui, Marc André Tétrault, Jean Baptiste Michaud, Catherine Pepin, Jules Cadorette, and Roger Lecomte. The hardware and signal processing architecture of LabPETTM, a small animal APD-based digital PET scanner. *IEEE Trans. Nucl. Sci.*, 56(1):3–9, 2009.

[82] Jorge Llacer and John D. Meng. Matrix-based image reconstruction methods for tomography. *IEEE Trans. Nucl. Sci.*, 32(1):855–864, 1985.

[83] V.V. Selivanov and R. Lecomte. Fast pet image reconstruction based on svd decomposition of the system matrix. *IEEE Trans. Nucl. Sci.*, 48(3):761–767, 2001.

[84] T. F. Budinger. Time-of-flight positron emission tomography: Status relative to conventional PET. *J. Nucl. Med.*, 24(1):73–79, 1983.

[85] S Surti and J S Karp. Design considerations for a limited angle, dedicated breast, TOF PET scanner. *Phys. Med. Biol.*, 53(11):2911–2921, 2008.

[86] Piotr J. Slomka, Tinsu Pan, and Guido Germano. Recent Advances and Future Progress in PET Instrumentation. *Semin. Nucl. Med.*, 46(1):5–19, 2016.

[87] S. Surti and J. S. Karp. Advances in time-of-flight PET. *Phys Med*, 32(1):12–22, Jan 2016.

[88] Dan J Kadrmas, Michael E Casey, Maurizio Conti, Bjoern W Jakoby, Cristina Lois, and David W Townsend. Impact of time-of-flight on PET tumor detection. *J. Nucl. Med.*, 50(8):1315–23, 2009.

[89] Dennis R. Schaart, Sibylle Ziegler, and Habib Zaidi. Achieving 10 ps coincidence time resolution in TOF-PET is an impossible dream. *Med. Phys.*, 47(7):2721–2724, 2020.

[90] Paul Lecoq et al. Roadmap toward the 10 ps time-of-flight PET challenge. *Phys. Med. Biol.*, 2020.

[91] S Gundacker, E Auffray, B Frisch, P Jarron, A Knapitsch, T Meyer, M Pizzichemi, and P Lecoq. Time of flight positron emission tomography towards 100ps resolution with L(Y)SO: an experimental and theoretical analysis. *J. Instrum.*, 8(07):P07014, 2013.

[92] Stephen E Derenzo, Woon-Seng Choong, and William W Moses. Fundamental limits of scintillation detector timing precision. *Phys. Med. Biol.*, 59(13):3261–86, 2014.

[93] Xin Yang, Evan Downie, Thomas Farrell, and Hao Peng. Study of light transport inside scintillation crystals for PET detectors. *Phys. Med. Biol.*, 58(7):2143–61, 2013.

[94] Maxime Toussaint, Francis Loignon-Houle, Jean-Pierre Dussault, and Roger Lecomte. Analytical model of DOI-induced time bias in ultra-fast scintillation detectors for TOF-PET. *Phys. Med. Biol.*, 64(6):065009, mar 2019.

[95] Stefan Seifert, Herman T van Dam, and Dennis R Schaart. The lower bound on the timing resolution of scintillation detectors. *Phys. Med. Biol.*, 57(7):1797–1814, 2012.

[96] Stefan Gundacker, Etiennette Auffray, Kristof Pauwels, and Paul Lecoq. Measurement of intrinsic rise times for various L(Y)SO and LuAG scintillators with a general study of prompt photons to achieve 10 ps in TOF-PET. *Phys. Med. Biol.*, 61(7):2802–2837, 2016.

[97] P. Lecoq. New approaches to improve timing resolution in scintillators. *IEEE Trans. Nucl. Sci.*, 59(5 PART 2):2313–2318, 2012.

[98] W.W. Moses, W.-S. Choong, and S.E. Derenzo. Modeling Time Dispersion Due to Optical Path Length Differences in Scintillation Detectors. *Acta Phys. Pol. B, Proc. Suppl.*, 7(4):725, 2014.

[99] S. E. Brunner, L. Gruber, J. Marton, K. Suzuki, and A. Hirtl. New approaches for improvement of TOF-PET. *Nucl. Instruments Methods Phys. Res. Sect. A Accel. Spectrometers, Detect. Assoc. Equip.*, 732:560–563, 2013.

[100] W. S. Choong. The timing resolution of scintillation-detector systems: Monte Carlo analysis. *Phys. Med. Biol.*, 54(21):6495–6513, Nov 2009.

[101] W W Moses and Q Peng. Artifacts in digital coincidence timing. *Phys. Med. Biol.*, 59(21):N181–5, 2014.

[102] F. Powolny, E. Auffray, S.E. E. Brunner, E. Garutti, M. Goettlich, H. Hillemanns, P. Jarron, P. Lecoq, T. Meyer, H.C. C. Schultz-Coulon, W. Shen, M.C.S. C S Williams, E. Auffray, S.E. E. Brunner, M. Despeisse, E. Garutti, M. Goettlich, H. Hillemanns, P. Lecoq, T. Meyer, F. Powolny, W. Shen, H.C. C. Schultz-Coulon, M.C.S. C S Williams, E. Auffray, S.E. E. Brunner, E. Garutti, M. Goettlich, H. Hillemanns, P. Jarron, P. Lecoq, T. Meyer, H.C. C. Schultz-Coulon, W. Shen, M.C.S. C S Williams, E. Auffray, S.E. E. Brunner, M. Despeisse, E. Garutti, M. Goettlich, H. Hillemanns, P. Lecoq, T. Meyer, F. Powolny, W. Shen, H.C. C. Schultz-Coulon, and M.C.S. C S Williams. Time based readout of a silicon photomultiplier (SiPM) for time of flight positron emission tomography (TOF-PET). *2009 IEEE Nucl. Sci. Symp. Conf. Rec.*, 58(3 PART 1):1212–1219, 2009.

[103] S. Gundacker, E. Auffray, B. Frisch, H. Hillemanns, P. Jarron, T. Meyer, K. Pauwels, and P. Lecoq. A systematic study to optimize SiPM photo-detectors for highest time resolution in PET. *IEEE Trans. Nucl. Sci.*, 59(5 PART 1):1798–1804, oct 2012.

[104] Dan J. Kadrmas, M. Bugrahan Oktay, Michael E. Casey, and James J. Hamill. Effect of scan time on oncologic lesion detection in whole-body PET. *IEEE Trans. Nucl. Sci.*, 59(5 PART 1):1940–1947, 2012.

[105] G. El Fakhri, S. Surti, C. M. Trott, J. Scheuermann, and J. S. Karp. Improvement in lesion detection with whole-body oncologic time-of-flight PET. *J. Nucl. Med.*, 52(3):347–353, 2011.

[106] C. Lois, B. W. Jakoby, M. J. Long, K. F. Hubner, D. W. Barker, M. E. Casey, M. Conti, V. Y. Panin, D. J. Kadrmas, and D. W. Townsend. An Assessment of the impact of incorporating time-of-flight information into clinical PET/CT imaging. *J. Nucl. Med.*, 51(2):237–245, 2010.

[107] Abolfazl Mehranian and Habib Zaidi. Impact of time-of-flight PET on quantification errors in MR imaging-based attenuation correction. *J. Nucl. Med.*, 56(4):635–41, 2015.

[108] Craig S. Levin, Sri Harsha Maramraju, Mohammad Mehdi Khalighi, Timothy W. Deller, Gaspar Delso, and Floris Jansen. Design features and mutual compatibility studies of the time-of-flight PET capable GE SIGNA PET/MR system. *IEEE Trans. Med. Imaging*, 35(8):1907–1914, 2016.

[109] J. Nuyts, A. Rezaei, and M. Defrise. The validation problem of joint emission/transmission reconstruction from TOF-PET projections. *IEEE Trans Rad Plasma Med Sciences*, 2(4):273–278, 2018.

[110] Eunsin Lee, Matthew E. Werner, Joel S. Karp, and Suleman Surti. Design optimization of a dedicated breast PET scanner using TOF imaging in a partial ring geometry. In *IEEE Nucl. Sci. Symp. Conf. Rec.*, pages 4276–4280, 2012.

[111] P. Gravel, Y. Li, and S. Matej. Effects of TOF resolution models on edge artifacts in PET reconstruction from limited-angle data. *IEEE Trans Rad Plasma Med Sciences*, pages 1–1, 2020.

[112] P. Lecoq. Pushing the limits in time-of-flight PET imaging. *J. Nucl. Med.*, 1(6):473–485, 2017.

[113] Joshua W Cates, Stefan Gundacker, Etiennette Auffray, Paul Lecoq, and Craig S Levin. Improved single photon time resolution for analog SiPMs with front end readout that reduces influence of electronic noise. *Phys. Med. Biol.*, 63(18):185022, sep 2018.

[114] Stefan Gundacker, Rosana Martinez Turtos, Nicolaus Kratochwil, Rosalinde Hendrika Pots, Marco Paganoni, Paul Lecoq, and Etiennette Auffray. Experimental time resolution limits of modern SiPMs and TOF-PET detectors exploring different scintillators and cherenkov emission. *Phys. Med. Biol.*, 65(2):025001, January 2020.

[115] Eric S. Harmon, Michael O. Thompson, C. Ross Schmidtlein, James N. Turner, and Andrzej Król. Towards 50 ps TOF-PET for brain imaging. In *Med. Imaging*, 2019.

[116] Stefan Gundacker, Rosana Martinez Turtos, Etiennette Auffray, Marco Paganoni, and Paul Lecoq. High-frequency SiPM readout advances measured coincidence time resolution limits in TOF-PET. *Phys. Med. Biol.*, 64(5):055012, Feb 2019.

[117] Hao Peng and Craig S Levin. Recent development in PET instrumentation. *Curr. Pharm. Biotechnol.*, 11(6):555–71, 2010.

[118] F Habte, A M K Foudray, P D Olcott, and C S Levin. Effects of system geometry and other physical factors on photon sensitivity of high-resolution positron emission tomography. *Phys. Med. Biol.*, 52(13):3753–3772, 2007.

[119] Y. Lv, X. Lv, W. Liu, M. S. Judenhofer, A. Zwingenberger, E. Wisner, E. Berg, S. McKenney, E. Leung, B. A. Spencer, S. R. Cherry, and R. D. Badawi. Mini EXPLORER II: a prototype high-sensitivity PET/CT scanner for companion animal whole body and human brain scanning. *Phys. Med. Biol.*, 64(7):075004, 03 2019.

[120] Jonathan K Poon, Magnus L Dahlbom, William W Moses, Karthik Balakrishnan, Wenli Wang, Simon R Cherry, and Ramsey D Badawi. Optimal whole-body PET scanner configurations for different volumes of LSO scintillator: a simulation study. *Phys. Med. Biol.*, 57(13):4077–94, 2012.

[121] S.C. Strother, M.E. Casey, and E.J. Hoffman. Measuring pet scanner sensitivity: relating countrates to image signal-to-noise ratios using noise equivalents counts. *IEEE Trans. Nucl. Sci.*, 37(2):783–788, 1990.

[122] Stefan Gundacker. *Time resolution in scintillator based detectors for positron emission tomography.* PhD thesis, Vienna, Tech. University, 2014.

[123] G. Muehllehner, J. S. Karp, and S. Surti. Design consideration for PET scanners. *Q. J. Nucl. Med.*, 46(1):16–23, 2002.

[124] Shiva Abbaszadeh, Garry Chinn, and Craig S. Levin. Effect of energy threshold in positioning true coincidences that undergo detector scatter for a sub-mm resolution CZT-based PET system. In *2015 EEE Nucl. Sci. Symp. Med. Imaging Conf. (NSS/MIC)*, pages 1–3, 2015.

[125] Yi Gu, Guillem Pratx, Frances W Y Lau, and Craig S. Levin. Effects of multiple photon interactions in a high resolution PET system that uses 3-D positioning detectors. *IEEE Nucl. Sci. Symp. Conf. Rec.*, 5494(2010):3814–3819, 2008.

[126] Timothy G. Turkington, John W. Wilson, and James G. Colsher. Adjusting the low energy threshold for large bodies in PET. In *IEEE Nucl. Sci. Symp. Conf. Rec.*, volume 5, pages 2872–2876, 2004.

[127] Maurizio Conti, Inki Hong, and Christian Michel. Simultaneous reconstruction of scatter and unscattered PET coincidences using TOF and energy information. *IEEE Nucl. Sci. Symp. Conf. Rec.*, 307:2332–2337, 2012.

[128] Julien Clerk-Lamalice, Melanie Bergeron, Christian Thibaudeau, and Roger Lecomte. Effect of inter-crystal scatter events on coincidence detection in LabPET scanners. In *2014 IEEE Nucl. Sci. Symp. Med. Imaging Conf. NSS/MIC 2014*, pages 2–4, 2016.

[129] Roger Lecomte, D Schmitt, and G Lamoureux. Geometry study of a high resolution PET detection system using small detectors. *IEEE Trans. Nucl. Sci.*, 31(1):556–561, 1984.

[130] Srilalan Krishnamoorthy, B LeGeyt, and ME Werner. Design and Performance of a High Spatial Resolution, Time-of-Flight PET Detector. *IEEE Trans. Nucl. Sci.*, 61(3):1092–1098, 2014.

[131] Michael V. Green, Harold G. Ostrow, Jurgen Seidel, and Martin G. Pomper. Experimental evaluation of depth-of-interaction correction in a small-animal positron emission tomography scanner. *Mol. Imaging*, 9(6):311–318, 2010.

[132] Stephen E. Derenzo, Woon Seng Choong, and William W. Moses. Monte Carlo calculations of PET coincidence timing: single and double-ended readout. *Phys. Med. Biol.*, 60(18):7309–7338, 2015.

[133] M. C. Maas, D. R. Schaart, D. J. van der Laan, P. Bruyndonckx, C. Lemaître, F. J. Beekman, and C. W. van Eijk. Monolithic scintillator PET detectors with intrinsic depth-of-interaction correction. *Phys. Med. Biol.*, 54(7):1893–1908, Apr 2009.

[134] Jung Yeol Yeom, Ruud Vinke, and Craig S. Levin. Side readout of long scintillation crystal elements with digital SiPM for TOF-DOI PET. *Med. Phys.*, 41(12):122501, 2014.

[135] H. Camilia Yousefzadeh, Roger Lecomte, and Réjean Fontaine. LabPET pulse simulator for crystal identification validation of multi-layer phoswich detectors. In *2009 IEEE Nucl. Sci. Symp. Med. Imaging Conf.(NSS/MIC)*, pages 578–582, 2009.

[136] Craig S Levin and Edward J Hoffman. Calculation of positron range and its effect on the fundamental limit of positron emission tomography system spatial resolution. *Phys. Med. Biol.*, 44(3):781–799, 1999.

[137] A. Rose. Quantum and noise limitations of the visual process. *J Opt Soc Am*, 43(9):715–716, Sep 1953.

[138] C. M. Michail, G. E. Karpetas, G. P. Fountos, I. G. Valais, D. Nikolopoulos, I. S. Kandarakis, and G. S. Panayiotakis. Assessment of the Contrast to Noise Ratio in PET Scanners with Monte Carlo Methods. *J. Phys. Conf. Ser.*, 637(1), 2015.

[139] H. H. Lin, K. S. Chuang, S. Y. Chen, and M. L. Jan. Recovering the triple coincidence of non-pure positron emitters in preclinical PET. *Phys. Med. Biol.*, 61(5):1904–1931, Mar 2016.

[140] Maurizio Conti, Lars Eriksson, and Victor Westerwoudt. Estimating image quality for future generations of TOF PET scanners. *IEEE Trans. Nucl. Sci.*, 60(1):87–94, 2013.

[141] Jianhua Yan, Josh Schaefferkoette, Maurizio Conti, and David Townsend. A method to assess image quality for Low-dose PET: Analysis of SNR, CNR, bias and image noise. *Cancer Imaging*, 16(1):1–12, 2016.

[142] Loc Fin, Pascal Bailly, Jol Daouk, and Marc Etienne Meyer. A practical way to improve contrast-to-noise ratio and quantitation for statistical-based iterative reconstruction in whole-body PET imaging. *Med. Phys.*, 36(7):3072–3079, 2009.

[143] Craig S. Levin. New imaging technologies to enhance the molecular sensitivity of positron emission tomography. *Proceedings of the IEEE*, 96(3):439–467, 2008.

[144] J. Joung, R.S. Miyaoka, and T.K. Lewellen. cMice:a high resolution animal PET using continuous LSO with a statistics based positioning scheme. In *2001 IEEE Nucl. Sci. Symp. Med. Imaging Conf. Rec. (Cat. No.01CH37310)*, volume 2, pages 1137–1141 vol.2, 2001.

[145] Jennifer R Stickel and Simon R Cherry. High-resolution PET detector design: modelling components of intrinsic spatial resolution. *Phys. Med. Biol.*, 50(2):179–195, 2005.

[146] Yiping Shao, Simon R. Cherry, Stefan Siegel, and Robert W. Silverman. A Study of inter-crystal scatter in small scintillator arrays designed for high resolution PET imaging. *IEEE Trans. Nucl. Sci.*, 43(3 PART 2):1938–1944, 1996.

[147] Francis Loignon-Houle, Mélanie Bergeron, Catherine M. Pepin, Serge A. Charlebois, and Roger Lecomte. Simulation of signal losses in highly pixelated scintillator arrays read out by discrete photodetectors. In *2015 IEEE Nucl. Sci. Symp. Med. Imaging Conf. NSS/MIC 2015*, pages 6–8, 2016.

[148] Sanae Rechka, Réjean Fontaine, Roger Lecomte, and Magdalena Rafecas. LabPET inter-crystal scatter study using GATE. In *IEEE Nucl. Sci. Symp. Conf. Rec.*, pages 3988–3994, 2009.

[149] David N. Ter Weele, Dennis R. Schaart, and Pieter Dorenbos. Scintillation detector timing resolution; A study by ray tracing software. *IEEE Trans. Nucl. Sci.*, 62(5):1972–1980, 2015.

[150] H Wieczorek, A Thon, T Dey, V Khanin, and P Rodnyi. Analytical model of coincidence resolving time in TOF-PET. *Phys. Med. Biol.*, 61(12):4699–4710, 2016.

[151] Simon R. Cherry, Yiping Shao, Martin P. Tornai, Stefan Siegel, Anthony R. Ricci, and Michael E. Phelps. Collection of Scintillation Light from Small BGO Crystals. *IEEE Trans. Nucl. Sci.*, 42(4):1058–1063, 1995.

[152] Craig S. Levin. Design of a high-resolution and high-sensitivity scintillation crystal array for PET with nearly complete light collection. *IEEE Trans. Nucl. Sci.*, 49 I(5):2236–2243, 2002.

[153] F. Loignon-Houle, M. Bergeron, C. M. Pepin, S. A. Charlebois, and R. Lecomte. Simulation of scintillation light output in LYSO scintillators through a full factorial design. *Phys Med Biol*, 62(2):669–683, 01 2017.

[154] NEMA. Performance measurements of small animal positron emission tomographs. *NEMA Standards Publication NU4-2008*, 2008. Rosslyn, VA.

[155] J. S. Reddin et al. Performance evaluation of the SiPM-based Siemens Biograph Vision PET/CT system. In *2018 IEEE Nucl. Sci. Symp. Med. Imaging Conf (NSS/MIC)*, pages 1–5, 2018.

[156] W. W. Moses and M. Ullisch. Factors influencing timing resolution in a commercial LSO PET camera. *IEEE Trans. Nucl. Sci.*, 53(1):78–85, 2006.

[157] S. Surti and J. S. Karp. Impact of detector design on imaging performance of a long axial field-of-view, whole-body PET scanner. *Phys. Med. Biol.*, 60(13):5343–5358, 2015.

[158] M Pizzichemi, A Polesel, G Stringhini, S Gundacker, P Lecoq, S Tavernier, M Paganoni, and E Auffray. On light sharing TOF-PET modules with depth of interaction and 157 ps FWHM coincidence time resolution. *Phys. Med. Biol.*, 64(15):155008, aug 2019.

[159] Sodai Takyu, Abdella M Ahmed, Eiji Yoshida, Hideaki Tashima, Masaaki Kumagai, Taichi Yamashita, and Taiga Yamaya. Design study of a brain-dedicated time-of-flight PET system with a hemispherical detector arrangement. *Phys. Med. Biol.*, 65(3):035012, feb 2020.

[160] Francis Loignon-Houle, Maxime Toussaint, M. S. Lee, Jashau Cates, and Roger Lecomte. Experimental validation of a coincidence time resolution metric including depth-of-interaction bias for TOF-PET. *Phys. Med. Biol.*, 65(24):245004, 12 2020.

[161] É. Gaudin, C. Thibaudeau, L. Arpin, J. D. Leroux, M. Toussaint, J. F. Beaudoin, J. Cadorette, M. Paillé, C. M. Pepin, K. Koua, J. Bouchard, N. Viscogliosi, C. Paulin, R. Fontaine, and R. Lecomte. Performance evaluation of the mouse version of the LabPET II PET scanner. *Phys. Med. Biol.*, 66(6):065019, 03 2021.

[162] Émilie Gaudin, Maxime Toussaint, Christian Thibaudeau, Maxime Paillé, Réjean Fontaine, and Roger Lecomte. Performance simulation of an ultra-high resolution brain PET scanner using 1.2-mm pixel detectors. *IEEE Trans Rad Plasma Med Sciences*, 3(3):334—342, May 2019.

[163] Jan S et al. GATE: a simulation toolkit for PET and SPECT. *Phys. Med. Biol.*, 49(19):4543, 2004.

[164] Thibaut Merlin et al. CASToR: A generic data organization and processing code framework for multi-modal and multi-dimensional tomographic reconstruction. *Phys. Med. Biol.*, 63(18), 2018.

[165] Robert L. Siddon. Fast calculation of the exact radiological path for a three dimensional CT array. *Med. Phys.*, 12(2):252–255, mar 1985.

[166] Filip Jacobs, Erik Sundermann, Bjorn De Sutter, Mark Christiaens, and Ignace Lemahieu. A fast algorithm to calculate the exact radiological path through a pixel or voxel space. *J. Comput. Inf. Technol.*, 6(1):89–94, 1998.

[167] Marina Filipović, Claude Comtat, and Simon Stute. Time-of-flight (TOF) implementation for PET reconstruction in practice. *Phys. Med. Biol.*, 64(23):23NT01, nov 2019.

[168] T. Tomitani. Image reconstruction and noise evaluation in photon time-of-flight assisted positron emission tomography. *IEEE Trans Nucl Sci.*, 28(6):4581–4589, 1981.

[169] Suleman Surti, Joel S. Karp, Lucretiu M. Popescu, Margaret E. Daube-Witherspoon, and Matthew Werner. Investigation of time-of-flight benefit for fully 3-D PET. *IEEE Trans. Med. Imaging*, 25(5):529–538, 2006.

[170] Maurizio Conti and Bernard Bendriem. The new opportunities for high time resolution clinical TOF PET. *Clinical and Translational Imaging*, 7(2):139–147, 2019.

[171] Joshua W Cates and Craig S Levin. Evaluation of a clinical TOF-PET detector design that achieves $\leqslant$100 ps coincidence time resolution. *Phys. Med. Biol.*, 63(11):115011, jun 2018.

[172] S. E. Brunner, L. Gruber, J. Marton, K. Suzuki, and A. Hirtl. Studies on the cherenkov effect for improved time resolution of TOF-PET. *IEEE Trans Nucl Sci*, 61(1):443–447, 2014.

[173] Joshua W Cates and Craig S Levin. Electronics method to advance the coincidence time resolution with bismuth germanate. *Phys. Med. Biol.*, 64(17):175016, Sep 2019.

[174] E. Berg and S. Cherry. Innovations in instrumentation for positron emission tomography. *Seminars in Nuclear Medicine*, 48(4):311–331, Jul 2018.

[175] Larissa Njejimana, Louis Arpin, Christian Thibaudeau, Nadia Jürgensen, Haithem Bouziri, Marc-André Tétrault, Nicolas Viscogliosi, Caroline Paulin, Roger Lecomte, and Réjean Fontaine. Firmware architecture of the data acquisition system for the LabPET II mouse scanner. In *2016 IEEE Nuclear Science Symposium, Medical Imaging Conference and Room-Temperature Semiconductor Detector Workshop (NSS/MIC/RTSD)*, pages 1–3, 2016.

[176] Émilie Gaudin, Louis Arpin, Jonathan Bouchard, Maxime Paillé, Haithem Bouziri, Mélanie Bergeron, Catherine M. Pepin, Jules Cadorette, Réjean Fontaine, and Roger Lecomte. Performance characterization of a dual-threshold time-over-threshold APD-based detector front-end module for PET imaging. In *2015 IEEE Nucl. Sci. Symp. Med. Imaging Conf. (NSS/MIC)*, pages 1–3, 2015.

[177] S Jan et al. GATE v6: a major enhancement of the GATE simulation platform enabling modelling of CT and radiotherapy. *Phys. Med. Biol.*, 56(4):881–901, Jan 2011.

[178] Albert Rose. *Vision: human and electronic*. New York: Plenum Press, 1973.

[179] Victor Westerwoudt, Maurizio Conti, and Lars Eriksson. Advantages of improved time resolution for TOF PET at very low statistics. *IEEE Trans. Nucl. Sci.*, 61(1):126–133, 2014.

[180] Tom K. Lewellen. Time-of-flight PET. *Seminars in Nuclear Medicine*, 28(3):268–275, 1998.

[181] M. E. Daube-Witherspoon, S. Surti, A. E. Perkins, and J. S. Karp. Determination of accuracy and precision of lesion uptake measurements in human subjects with time-of-flight PET. *J Nucl Med*, 55(4):602–607, Apr 2014.

[182] Gerard Ariño-Estrada, Emilie Roncali, Aaron R Selfridge, Junwei Du, Jaroslaw Glodo, Kanai S. Shah, and Simon R. Cherry. Study of Cherenkov light emission in the semiconductors TlBr and TlCl for TOF-PET. *IEEE Trans. Rad. Plasma Med. Sci. (Early Access)*, Sept. 2020.

[183] S. Gundacker, E. Auffray, P. Jarron, T. Meyer, and P. Lecoq. On the comparison of analog and digital SiPM readout in terms of expected timing performance. *Nucl. Instrum. Methods Phys. Res. A: Accel. Spectrom. Detect. Assoc. Equip.*, 787:6–11, 2015. New Developments in Photodetection NDIP14.

[184] NEMA. Performance measurements of positron emission tomographs. *NEMA Standards Publication NU2-2001*, 2001. Rosslyn, VA.

[185] Gin-Chung Wang et al. PET timing performance measurement method using NEMA NEC phantom. *IEEE Trans. Nucl. Sci.*, 63(3):1335–1342, 2016.

[186] A. Hirtl, H. Bergmann, B. Knäusl, T. Beyer, M. Figl, and J. Hummel. Technical Note: Fully-automated analysis of Jaszczak phantom measurements as part of routine SPECT quality control. *Med Phys*, 44(5):1638–1645, May 2017.

[187] L. S. Graham, F. H. Fahey, M. T. Madsen, A. van Aswegen, and M. V. Yester. Quantitation of SPECT performance: Report of Task Group 4, Nuclear Medicine Committee. *Med Phys*, 22(4):401–409, Apr 1995.

[188] L. Eriksson and M. Conti. Randoms and TOF gain revisited. *Phys. Med. Biol.*, 60(4):1613–1623, Feb 2015.

[189] Deepak Bharkhada, Lars Eriksson, Maurizio Conti, and Harold Rothfuss. SNR TOF gain in high time resolution PET systems. In *2017 IEEE Nucl. Sci. Symp. Med. Imaging Conf. (NSS/MIC)*, pages 1–2, 2017.

[190] R. M. Turtos, S. Gundacker, E. Auffray, and P. Lecoq. Towards a metamaterial approach for fast timing in PET: experimental proof-of-concept. *Phys. Med. Biol.*, 64(18):185018, Sept 2019.

[191] S. Enoch, A. Gola, P. Lecoq, and A. Rivetti. Design considerations for a new generation of SiPMs with unprecedented timing resolution. *J. Instrum*, 16(02):P02019–P02019, Feb 2021.